2020-01-01

Laser Diagnostics Of Compressible And High-Intensity Premixed Methane-Air Combustion Inside A Backward Facing Step Combustor Using High- Repetition Rate CH-PLIF And PIV

Md. Amzad Hossain
University of Texas at El Paso

Recommended Citation

LASER DIAGNOSTICS OF COMPRESSIBLE AND HIGH-INTENSITY
PREMIXED METHANE-AIR COMBUSTION INSIDE
A BACKWARD FACING STEP COMBUSTOR
USING HIGH- REPETITION RATE
CH-PLIF AND PIV

Md. Amzad Hossain

Doctoral Program in Mechanical Engineering

APPROVED:

_____
Ahsan R. Choudhuri, Ph.D., Chair

_____
Norman D. Love, Ph.D.

_____
Md Mahamudur Rahman, Ph.D.

_____
Luis Rene Contreras Sapien, Ph.D.

_____
Stephen L. Crites, Ph.D.
Dean of the Graduate School

Dedication

This dissertation is dedicated to my parents, wife, and friends whose unlimited love, support, and encouragement have inspired me to pursue and complete this research.

LASER DIAGNOSTICS OF COMPRESSIBLE AND HIGH-INTENSITY PREMIXED METHANE-AIR COMBUSTION INSIDE A BACKWARD FACING STEP COMBUSTOR USING HIGH- REPETITION RATE CH-PLIF AND PIV

by

Md. Amzad Hossain, B.Sc., M.Sc.

DISSERTATION

Presented to the Faculty of the Graduate School of

The University of Texas at El Paso

in Partial Fulfillment

of the Requirements

for the Degree of

DOCTOR OF PHILOSOPHY

Department of Mechanical Engineering

THE UNIVERSITY OF TEXAS AT EL PASO

May 2020

Acknowledgments

Abstract

A novel high repetition rate (10 kHz) planar laser-induced fluorescence (PLIF) diagnostic technique was used for the flame front study. Premixed methane-air combustion was studied at different flow turbulence conditions (Re = 15000, 30000 and 64000; 12CFM, 25CFM and 50 CFM; 10m/s, 20 m/s and 40 m/s) and fuel loading (Φ =0.6 to 1.2). The study used an optically accessible backward-facing step high-speed combustor. Methane-air mixture was supplied to the combustor at atmospheric pressure and standard room temperature (T =25ºC). CX-CH PLIF was used to detect the actual flame front structures. The flame dynamics were then correlated to the flow dynamics at various turbulent length scales (L_T) and velocity fluctuations (u'). The turbulent length scales were varied using turbulence-generating grids with blockage ratios (BR) from 46% to 63% and two-hole diameters (HD) of 1.5 mm and 3 mm. The velocity fluctuations (u') were altered using different flow momentum at the combustor inlet. The different flow momentum yields a different Reynolds number at the edge of the backward-facing step. The flow properties such as velocity vector fields, velocity fluctuations (u'), turbulent intensity (I), and vorticity (ω) were measured at the edge of the backward-facing step using a 10 kHz time-resolved particle image velocimetry (PIV). The flame and flow characteristics were used to locate the flame regime on Borghi-Peter's diagram. The study of flame-flow correlation was done at different Damkohler number (Da), Karlovitz number (Ka), and mixture flow rates. The effects of Reynold's Number (Re) and grids on the flame and flow dynamics were studied. CH-PLIF was tuned by changing the dye of the existing laser system. A wavelength of 314.415 nm was found to be the most effective wavelength for the detection of the CX-CH band. This wavelength results in better visualizing the flame front. The detection of the CH signal and extraction of flame fronts was very challenging. This is due to the experimental complexity with overlapping OH bands, laser wall scattering, and in-flame soot formation. Two different MATLAB based image processing codes were developed to

detect the flame profiles and flame edges. It was observed that the flame turbulence and flame width (lateral expansion) increased as the flame moves downstream. It was also observed that there was a presence of unburned gases inside the burned gases and vice-versa. Additionally, an irregularly shaped flame wrinkling was noticed. However, wrinkle size decreased throughout the flame evolution. The flame wrinkling was higher with small-hole diameters grids (grid 1 and grid 3), whereas the flamelet breakdown, burnout, flame expansion, flame stretching, and turbulent flame speed were higher under larger diameter grids (grid 2 and grid 4). The combustor system is being upgraded for supersonic combustion conditions (Ma =2) using customed air heaters and De Laval Nozzle. The analytical calculations, design optimization, experimental methodology, and post data analysis schemes for supersonic combustion tests are also reported in this dissertation.

Table of Contents

List of Tables

List of Figures

Chapter 1: Introduction

The design and development of next-generation high-speed engine combustors such as scramjets require an in-depth understanding of high-intensity turbulent combustion [1], [2]. The turbulent flame study has experienced the use of non-intrusive flame measurement techniques such as high-speed laser diagnostics in the last two decades. Among the non-intrusive measurement techniques, planar laser-induced fluorescence (PLIF) has been widely used to characterize the turbulent flame behavior for both open and closed combustion systems. PLIF is used to target the species present in the flame, such as hydroxyl (OH), CH_2O, and methylidyne (CH). The OH radicals are present in abundance in flames, and the concentration gradients of OH radicals are high. Also, the OH radical near the flame has a high lifetime and thus suitable for tracking flame fronts in a highly turbulent environment. Due to these advantages, the OH radicals have been used in high-repetition-rate PLIF diagnostics[3], [4]. While these advantages seem prevailing, there are few questions about the use of OH as the flame front tracer. For instance, OH is slowly removed away by three-body collisions; therefore, OH could be convected to flow downstream, making it very difficult to trace the primary fuel reaction zone. Also, OH is a tracer of the radical-recombination zone, not necessarily a marker of flame front tracing [5].

Generally, Methylidyne (CH) radicals provide superior flame front tracking, as they are formed and removed away by rapid two-body collision reactions during the initial fuel decomposition. Consequently, the CH radicals are present during the main course of combustion, resulting in better detection of flame fronts. Besides, there is a good correlation between the CH signal and heat release rate [6]–[8]. Carter's group [9] has reported three bands of CH radicals. According to their statement, among the CH bands, C-X ($C^2\Sigma^+$ -$X^2\pi$ (0,0) band) is relatively better compared to other two bands: A-X ($A^2\Sigma^+$ -$X^2\pi$ (0,0)) and B-X (BΣ—XΠ).

The C-X CH band could be easily generated using the frequency-doubling dye laser system, for instance, YAG pump-dye laser commonly used for OH detection [7], [10], [11]. Therefore, the excitation wavelength of C-X CH bands could be achieved by a low laser power system. Also, the C-X CH band has better absorption, and emission coefficients compare to A-X and B-X bands of CH. Moreover, the excitation and emission spectrum of the C-X CH radical are broad, generally held at $\geq$314nm [9]. Therefore, there is no chance of having resonance in the PLIF system, unless the excitation wavelength is very close to the emission wavelength. Care needs to be taken in the selection of CH excitation wavelength as it might overlap with OH excitation bands.

Most of the researchers, including Carter's group uses OH PLIF and CH PLIF in an open flame system such as Bunsen burner, flat plate burner, and flat swirl burner [3], [8], [12]. Very few investigations were done with closed flame systems. Also, experimental analysis of flame-flow interaction at higher-order turbulence remains very limited [6], [13], [14]. The status of the present scientific literature on OH and CH flame diagnostics is presented in Figure 1. The statistical results presented in Figure 1 are based on 100 random papers that were published in the last two decades. It shows that most researches are done for the open flame system and OH PLIF. The research works on the closed flame system, and CH PLIF is very limited. Also, the application of C-X CH PLIF to the closed flame system is limited. An experimental methodology and laser flame diagnostics were investigated using the C-X CH PLIF technique to address these issues.

The Center for Aerospace and Exploration Technology Research (cSETR) at the University of Texas at El Paso with the funding support from NASA and Army Research Office (ARO) has developed an experimental high-speed premixed combustion test facility. The initial design, development, and testing of the combustion system were done by former cSETR graduate students Arturo Acosta-Zamora (Ph.D.), Arifur Rahman (MS), and Martin Alejandro

De La Torre (Ph.D.), The previous team, also performed some preliminary tests using the OH PLIF. The present research builds on the previous work by completing the flame front detection using CH imaging as well as additional flow-field data processing.
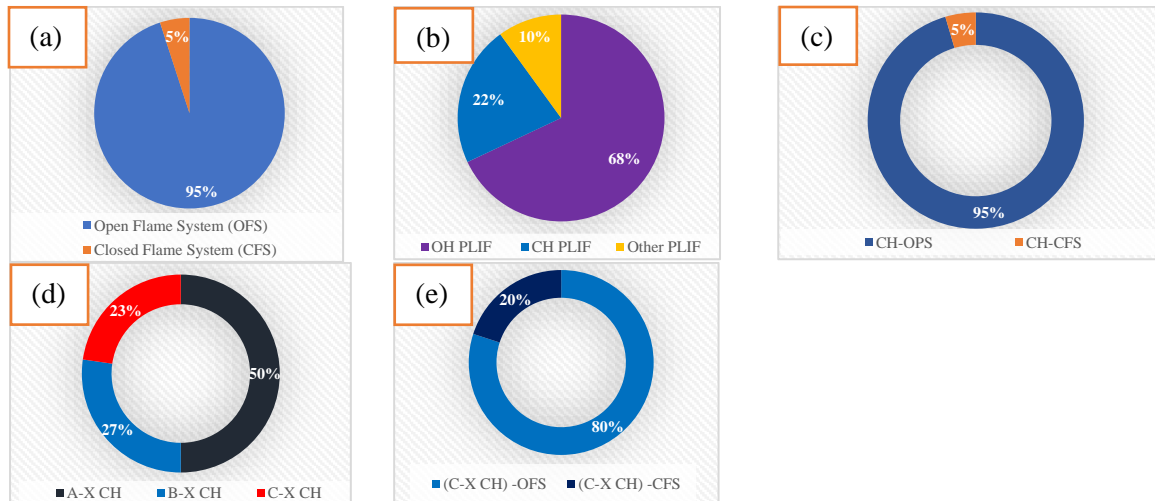
Figure 1. Random statistical analysis of PLIF based combustion literature, (a) Flame systems; (b) PLIF systems; (c) CH based flame system, (d) CH bands based PLIF, and (e) C-X CH based flame systems

1.1 Objectives

The primary objective of this research is to understand the premixed flame dynamics under compressible and extreme turbulence environments. The overarching goal of the cSETR high speed and high-intensity turbulent combustion research is to address the following research questions:

[1] What are the characteristics of premixed flame structures at a compressible and high-intensity turbulent combustion?

[2] What is the limit of regime boundaries at this condition?

[3] What are the scales that affect the characteristics of the reaction zone?

Chapter 2: Background Theory and Literature Review

The following chapter is designed to give an idea of relevant background theories, statements, terminologies and previous works pertinent to this Ph.D. research work. The flow behavior over a backward-facing step, turbulent flow and turbulent combustion theories, laser diagnostic techniques will be discussed sequentially in this chapter.

2.1 Flow Stabilization Using a Backward Facing Step

The flow dynamics over a backward-facing step has been studied extensively because of its geometric simplicity. It has been also used to validate the experimental results with CFD results. The purpose of using the backward-facing step is to stabilize the flame inside the combustor. When the flow goes over the step, there is a sudden change in the fluid flow path. Therefore, there is a formation of low-speed velocity recirculation zones right after the step. Also, there is a formation of a boundary layer at the end of the step. This forms a shear layer right after the onset of the step. At the shear layer, the formation and breakdown of vortices continue. The low-speed recirculation zones and whirling vortex helps to anchor the flame. This flame anchoring mechanism is well stabilized and tested at different flow conditions [11], [15].

Armaly et al [16] and Biswas et al [17] have investigated the flow characteristics over a backward-facing step using both experimental and numerical approaches. The schematic of their backward-facing step is shown in Figure 2. The results were used to generate the turbulent parameters for high-velocity flows. Similar research was conducted by M.A. Hossain [3] where a CFD analysis is performed to investigate different recirculation zones after the backward-facing step. Their observation was matched with existing literature [11],[17] and is shown in Figure 3.

4
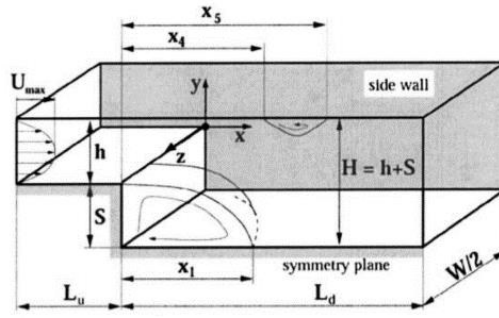
Figure 2. A schematic of a backward-facing step [17]
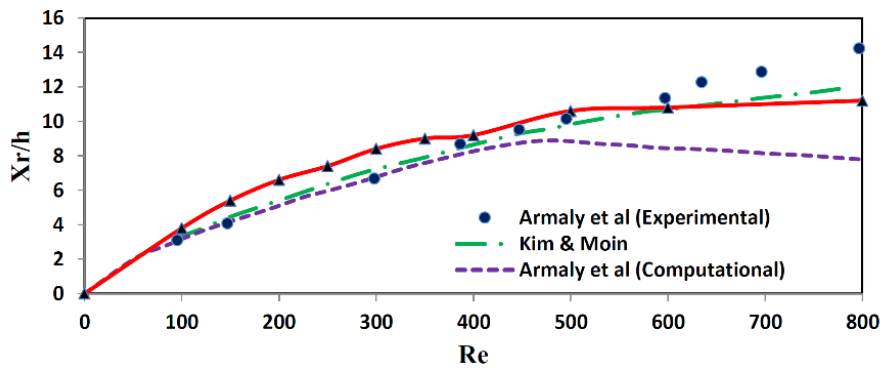
Figure 3. The validation of experimental and CFD results over a backward-facing step [3]

Pitz and Daily [18] have used a laser velocimetry and Schlieren photography techniques to investigate the turbulent characteristics over a backward-facing step for a reacting and non-reacting flow. Cohen et al [19] have investigated the effect of equivalence ratios on the near blowout thermal instabilities. They have also investigated the effect of pulsating flow on the velocity flow field using laser velocimetry. The different recirculation zones identified by their research is presented in Figure 4. Similar research was done by Sabelnikov et al [20] on thermoacoustic instabilities. They have used a 4kHz PIV and 4kHz OH-PLIF for flow and field characterization respectively.
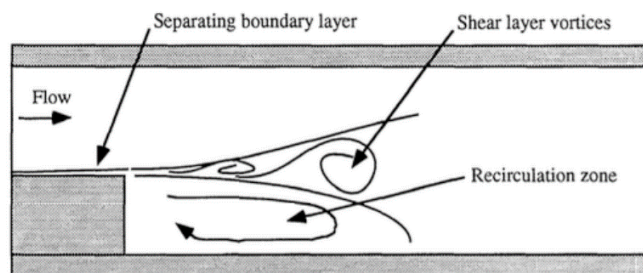
Figure 4. The location of different separation zones for flow over a backward-facing step [19]

5

2.2 Turbulent Flows

Turbulent flow is characterized by the unsteadiness, irregularity, randomness, and chaos in the flow. In the turbulent regime, the boundary layer may repeat, and identical flow may not be reproduced. However, the flow characteristics such as velocity fluctuation, or mean flow velocity have been well studied. These properties provide well descriptions of any turbulent flow.

The properties of turbulent flow depend on the nature of fluids, fluid velocity, surface geometry, surface temperature, and surface roughness, etc. Osborne Reynolds has identified that the transition in flow regimes depends on inertial and viscous forces. The ratio of inertial force to the viscous force is called the Reynolds number (Re). For internal flow, it is expressed as the following equation:

$$Re = \frac{Inertial\ FLow}{Viscous\ Flow} = \frac{V\ D}{\vartheta} = \frac{\rho V\ D}{\mu} \tag{1}$$

In Eq. (1), V is the flow velocity, ρ is the flow density, D is the characteristics dimension of the flow passage, ϑ is the kinematic viscosity of the flow and μ is the dynamic (absolute) viscosity of the flow. For most practical cases, the flow through a pipe is laminar when Re $\lesssim$ 2300, transitional when 2300 $\lesssim$ Re $\lesssim$ 4000 and turbulent when Re $\gtrsim$ 4000.

2.2.1 Statistical Description of Turbulent Flow

The most flows encountered in engineering practice are turbulent flows. Therefore, it is important to know the turbulent flow characteristics. The turbulent flow is mostly controlled by eddies which are the rapid fluctuating swirling regions of the flow. The turbulent eddies transport mass, momentum, and energy to the nearest regions at a rate faster than the molecular diffusion. Therefore, the turbulent flow has a higher value of friction. Also, it has higher heat

and mass transfer coefficients. If a hot wire anemometer is placed inside a flow, the recorded instantaneous velocity could be expressed as follows:

$$u(t) = u\acute{}(t) + \bar{u} \tag{2}$$

$$v(t) = v\acute{}(t) + \bar{v} \tag{3}$$

In Eq. (2) and (3), the $\bar{u}$ and $\bar{v}$ represent the mean velocity components to the x and y directions, and $u\acute{}(t)$ and $v\acute{}(t)$ represent the velocity fluctuating components in x and y directions. A typical velocity fluctuation profile is shown in Figure 5.
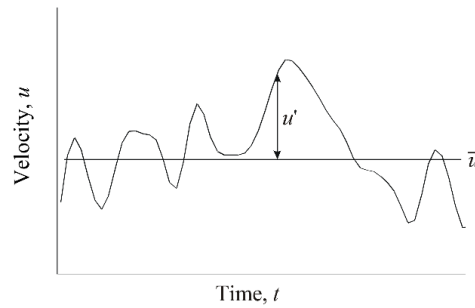
Figure 5. The turbulent velocity fluctuation profile [21]

The velocity fluctuation at any point in a flow field is often determined using the root-mean-square velocity, which is represented by u_{rms}. This is also called the standard deviation of flow velocity and is expressed with the following formula:

$$u_{rms} = \left[\frac{1}{N} \Sigma_i^N (u\acute{}(t))^2\right]^{\frac{1}{2}} \tag{4}$$

The rms velocity shows the level of turbulent energy present in the flow.

2.2.2 Turbulent Kinetic Energy (TKE)

The turbulent kinetic energy (TKE or k) is the measure of energy variation per unit control volume of the flow field. The rms velocity in x, y and z could be used to determine the turbulent kinetic energy. The TKE is described with the following equation:

$$k = \frac{1}{2}\left(u^2{}_{rms} + v^2{}_{rms} + w^2{}_{rms}\right) \tag{5}$$

Eq. (5) could be further simplified using the isotropic turbulence assumption where the fluctuating velocity components are equal, or the z-direction fluctuation is equal to the y-direction [21]. With the simplifying assumption,

$$k = \frac{3}{2}(\acute{u}^2) = \frac{1}{2}\left(u^2{}_{rms} + 2v^2{}_{rms}\right) \tag{6}$$

2.2.3 Turbulent Intensity (I)

The turbulent intensity (I) is an important parameter that shows the different levels of turbulent zones inside the flow. Turbulent Intensity (I) is the ratio of the velocity fluctuation component (u') to the mean velocity component ($\bar{U}$). The turbulent fluctuating term $\acute{u}$ which represent the velocity variation in the flow could be expressed as follows,

$$\acute{u} = \sqrt{\frac{u^2{}_{rms} + 2v^2{}_{rms}}{3}} \tag{7}$$

Therefore, the turbulent Intensity (I)

$$I = \frac{u'}{\bar{U}} \tag{8}$$

For most practical cases, the average value of turbulent intensity varies from 5% to 20%.

2.2.4 Turbulent Eddy Vorticity

For the fundamental understanding of the turbulent combustion mechanism, it is important to understand the turbulent eddy vorticity. For this, the vorticity ($\bar{\omega}$) must be calculated. The vorticity could be determined by taking the curl of the mean velocity component ($\bar{U}$) which are shown below:

$$\bar{\omega} = rot\,(\bar{U}) = curl\,(\bar{U}) = \nabla \times \bar{U} = \left(\frac{\partial w}{\partial y} - \frac{\partial v}{\partial z}\right)\bar{\imath} + \left(\frac{\partial u}{\partial z} - \frac{\partial w}{\partial x}\right)\bar{\jmath} + \left(\frac{\partial v}{\partial x} - \frac{\partial u}{\partial y}\right)\bar{k} \tag{9}$$

Where each term under the first parenthesis represents the rotation along the x, y, and z-axis. For 2D flow, it reduces to the rotation along the z-axis only:

$$\omega_z = \left(\frac{\partial v}{\partial x} - \frac{\partial u}{\partial y}\right) \qquad (10)$$

2.2.5 Energy Cascading and Turbulent Length Scales

To analyze the flow field and detect the flame regimes, the understanding of different energy modes and length scales is important. The turbulent length scale defines the size of eddies present in the flow field. The eddies with the highest amount of energy are called the largest eddies and represented by L_T. The largest eddies have the highest kinetic energy. Those eddies start losing their energy to the nearest small eddies because of the energy breakdown. It continues as long as the mechanical energy converts to the thermal dissipation energy. The small eddies are responsible for the viscous dissipation of kinetic energy. The smallest eddies are called the Kolmogorov scale (ɳ). The principle is referred to as the energy cascade principle and could be described by Kolmogorov's hypothesis [22].
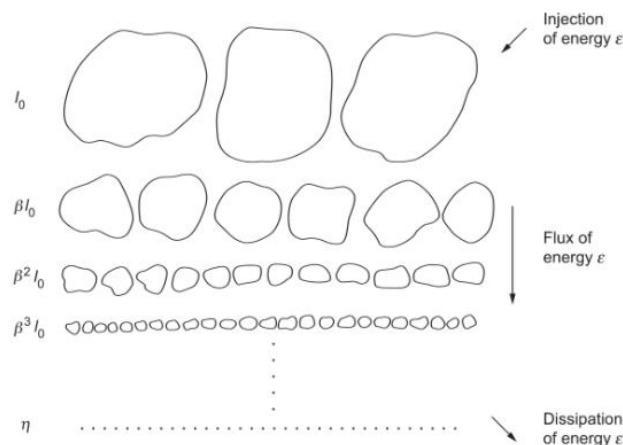
Figure 6. Energy cascading Principle (Image is taken from http://astro.physics.ncsu.edu/~madelosr/background.html)

The smallest scales of the flow are calculated based on the viscosity of the flow at that instance of time. The energy dissipation (ε), timescale (t_η), velocity-scale (u_η) and the smallest length scale (η) could be calculated using the following equations:

$$\varepsilon = \frac{u_0{}^3}{L} \tag{11}$$

$$t_\eta = \left(\frac{\vartheta}{\varepsilon}\right)^{\frac{1}{2}} \tag{12}$$

$$u_\eta = (\vartheta\varepsilon)^{\frac{1}{4}} \tag{13}$$

$$\eta = \left(\frac{\vartheta^3}{\varepsilon}\right)^{\frac{1}{4}} \tag{14}$$

2.2.6 Grid Induced Turbulence

The turbulence enhances the heat and mass transfer to the flow. For this, perforated plates also called grids have been used extensively for the normal flow or crossflow. The grid creates homogenous isotropic turbulence inside the flow. The assumptions of isotropic turbulence are (i) flow properties are independent of the position and orientation, (ii) there is no rotation and buoyancy and (iii) the average of the mean flow is zero [23]. The fluid flow evolution inside the grid domain could be segmented into three consecutive stages. The first stage is transitioned to fully developed turbulent flow, the second stage is the fully developed turbulent flow and the last stage is the small-scale turbulence decay.
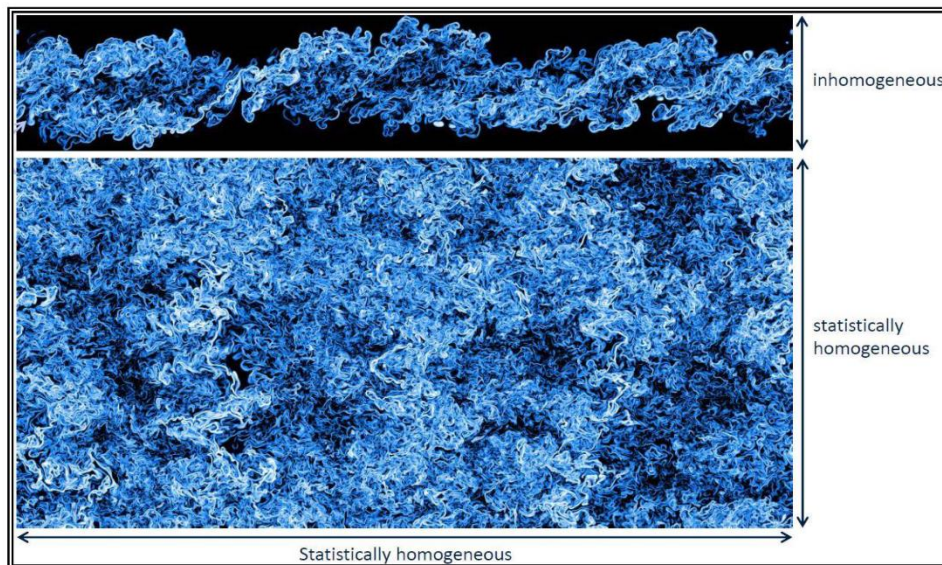
Figure 7. Evolution of grid Induced turbulence [23]

2.3 Combustion and Flames

When reactants (fuel and oxidizer/air) are ignited, they induce an exothermic reaction and release some heat to the surrounding. The heat release through the ignition of an oxidizer and fuel is called combustion. Generally, the fuel is considered as the energy source which releases heat through instantaneous chemical reactions. The propagating nature of the chemical reaction is called flame. The flame continues as long as the chemical reaction reactions continue. The pressure and temperature of the combustor increases as the reaction continue [24].

The flame is divided into two broad categories: premixed flame and non-premixed flame (diffusion flame). If the reactants mix completely or partially before being ignited, the resulting flame is called a premixed flame. On the other hand, if the reactants do not mix before the ignition, the flame is called a non-premixed flame. In this case, the reactants are separated and interact at their interface [24].

11

2.3.1 Statistical Description of the Combustion

The ratio of oxidizer and fuel has a tremendous effect on combustion dynamics. The ratio of oxidizer and fuel needed to have complete combustion is referred to as stoichiometry. If the oxidizer ratio increases over the stoichiometry, the mixture is called a lean mixture. On the other hand, if the fuel ratio goes over the stoichiometry, it is called a rich mixture. In this study, methane and air are used as reactants. The following equation expresses the complete chemical formulation of hydrocarbon and air mixture:

$$C_xH_y + \left(x + \frac{y}{4}\right)(O_2 + 3.76N_2) \rightarrow xCO_2 + \left(\frac{y}{2}\right)H_2O + 3.76(x + \frac{y}{2})N_2 \quad (15)$$
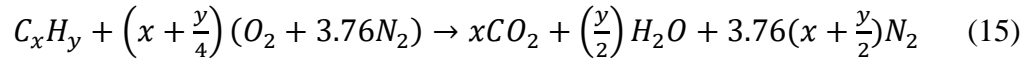
The general assumption of the air is that it has 79% oxygen and 21% nitrogen. Therefore, the combustion formula for methane and air is going to be,

$$CH_4 + (O_2 + 3.76N_2) \rightarrow 2CO_2 + 2H_2O + 7.52N_2 \quad (16)$$
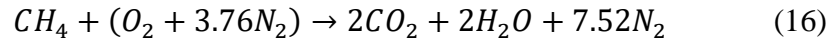
The stoichiometric air-fuel ratio is defined as the ratio of the mass of air to the mass of fuel, as expressed below:

$$\left(\frac{A}{F}\right)_{stoic} = \frac{m_{air}}{m_{fuel}} \quad (17)$$

Therefore, the stoichiometric ratio for air-methane is 17:1. This ratio could be further used to determine the nature of the reactant mixture, whether the mixture is lean or rich. This could be done with the implementation of the equivalence ratio (φ),

$$\varphi = \frac{\left(\frac{A}{F}\right)_{stoic}}{\left(\frac{A}{F}\right)_{actual}} \quad (18)$$

If the $\varphi = 1$, the mixture is stoichiometric, $\varphi < 1$, the mixture is lean and $\varphi > 1$, the mixture is rich. The research presented in this study has considered the lean, stoichiometric and

12

rich mixture conditions at different Re's. However, φ =1 is used to detect the flame regime and scale factors that control the reaction zone.

2.3.2 Laminar Premixed Combustion

The understanding of laminar flame or laminar premixed flame is important for most of the practical cases of combustion. For instance, most of the turbulent combustion and computational models derived from the assumption of laminar flame characteristics. A typical laminar premixed methane-air flame structure is presented in Figure 8 [25]. The flame has two zones: the chemically inert preheat zone and the reaction zone. The preheat zone has very little change in temperature because the heat release rate is too small, whereas the reaction zone experienced a high heat release. Consequently, the temperature and concentration gradients are too high in the reaction zone. The reaction zone has two intermediate layers. The first layer in the reaction zone is called the inner layer or fuel consumption layer of order δ_L. The fuel is consumed in this layer and radicals are depleted by the fast chain-breaking reaction. This layer is also responsible to keep the reaction process alive. The second layer in the reaction zone is called the oxidation layer of the order ε. The global flame structure could be interrupted if the reaction zone flame gets distracted by the flow turbulence. If the smallest scale eddy or Kolmogorov scale is less than the reaction zone thickness, the eddies might get penetrated to the inner layer flame. Thus, it makes the reaction zone even thinner.

2.3.2.1 Laminar Flame Structure

Under the adiabatic condition, the propagation of a quiescent flame through a homogenous mixture of unburned gases is called the laminar flame speed. Based on the literature, it is found that the laminar flame thickness (δ_L) is typically less than 1 mm. This is the zone of interest of this present research.

13
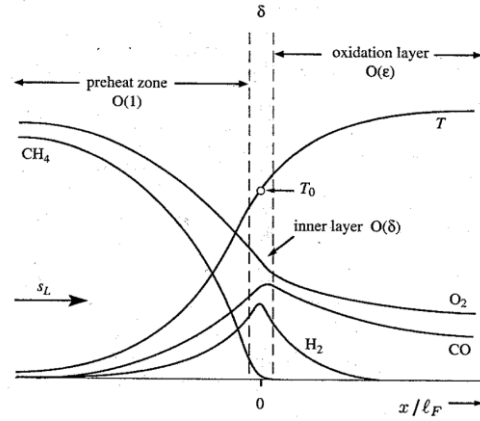
Figure 8. The Premixed Methane-Air Flame Structure [25]

The laminar flame thickness (δ_L) could be calculated by taking the tangent of the flame temperature profile. Another way of calculating the δ_L is to consider the flame thermal diffusivity ($D_{mixture}$) and the laminar flame speed (S_L) [26].

$$\delta_L = \frac{D_{mixture}}{S_L} \tag{19}$$

The $D_{mixture}$ and S_L both depend on the pressure, temperature and fuel-air concentration. For this research, the S_L value of 36 cm/s is used.

2.3.3 Behavior of Combustion Species

As the combustion continues, there is a formation of many intermediate species. When hydrocarbons such as methane (CH_4) is ignited, it forms the following radicals in sequence: OH, CH_2O, HCO, and CH. Concentration profiles of these species depend on the flame position, path of flame propagation, flame temperature, etc. A typical concentration profile of CH_4-air combustion is shown in Figure 9.

14
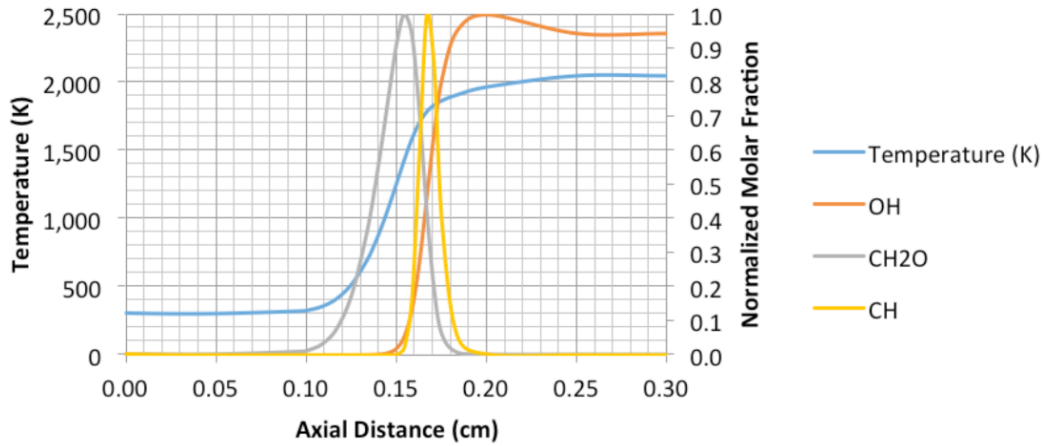
Figure 9. The concentration profiles of combustion radicals with temperature and mole fraction [12]

HCO and CH exhibit high heat release rates in the inner flame zone, however, their concentration is low, and they have a very short life. The OH and CH₂O radicals have a higher concentration and they sustain in the flame for a long time. They also present near the flame fronts and combustion products. However, they might be convected to flow downstream, which makes it very difficult to trace the primary fuel reaction zone. The alternative way to tracing the flame front is to use the CH radicals [27]–[29]. However, the excitation of CH radicals is not easy. It requires a high repetition laser power system. In this research, the C-X band is chosen over the A-X and B-X bands of CH. The advantages of using the C-X CH band are already discussed in chapter one and will be also discussed in the following section of this thesis work.

2.3.4 Statistical Description of Turbulent Premixed Combustion

In most of the practical cases, combustion takes place in extreme turbulence. The characteristics of turbulent premixed combustion could be investigated using different combustion models. Often time extensive experimentation is needed to establish and validate those combustion models. There are many parameters which have been used to define the turbulent premixed combustion, for instance, turbulent flame speed (S_T), Karlovitz Number (Ka), Damkohler Number (Da) and turbulent Reynolds Number (Re_T), etc.

The laminar flame speed simply depends on the thermal energy of the reactants, however, the turbulent flame speed (S_T) depends on both flow and reactant characteristics. Although there are many equations for the S_T, the following is used for its simplicity.

$$S_T = \frac{\dot{m}}{A\rho_u} \tag{20}$$

Where $\dot{m}$ is the mass flow rate of the gas mixture, A is the area of flame, and ρ_u is the density of the unburned gas mixture. The flame-flow interaction is an important part of combustion study. There are many non-dimensional parameters, for instance, Damkohler Number (Da), Karlovitz Number (Ka) and Turbulent Reynolds Number (Re$_T$), etc that have been used to define the turbulent flame-flow interaction.

The Karlovitz number (Ka) relates the chemical timescale to the Kolmogorov timescale. In another word, Ka relates the laminar flame properties to the turbulent length-scale and velocity fluctuation. The Karlovitz number (Ka) shows the degree of flame stretching. Higher the number of Ka, higher the stretching in the flame. Also, the flamelet breakdown, burnout, flame expansion, and flame broadening are increases with the increase in Ka. The Ka is defined as follows:

$$Ka = \frac{\text{Chemical Time Scale}}{\text{Kolmogorov Time Scale}} = \left(\frac{L_T}{\delta_L}\right)^{-\frac{1}{2}} \left(\frac{u'}{S_L}\right)^{\frac{3}{2}} \tag{21}$$

Damkohler Number (Da) relates the reaction rate to the diffusion rate. It indicates what controls flame propagation. Therefore, if chemical timescale dominates over turbulent timescale, Da is going to be greater than unity. If turbulent timescale dominates over chemical timescale then Da is less than unity. Less the value of Da, higher the flame wrinkling would be.

$$Da = \frac{\text{Reaction Rate}}{\text{Diffusion Rate}} = \frac{\text{Chemical Time Scale}}{\text{Turbulent Time Scale}} = \frac{L_T S_L}{u'\delta_L} \tag{22}$$

Turbulent Reynolds number (Re_T) is a function of velocity fluctuation (u'), integral length-scale of eddies (L_T), and laminar flame properties such as S_L and δ_L. The Re_T is expressed as follows:

$$Re_T = \frac{u'L_T}{S_L\delta_L} \tag{23}$$

2.3.5 Statistical Description of Flame Regimes

Turbulence parameters and flame parameters are used to detect the flame regimes. The diagram used to classify the flame is called the Borghi diagram. This diagram is later modified by Peter [25]. Borghi-Peter's diagram is shown in Figure 10. The assumption used for this diagram is that the turbulent flame structure is the same as the stretched flame structure [23]-[24]. The main categories of flames are corrugated flames, thin reaction zones, and well-stirred reactor regimes. The Ka = 1 and Re=Re_T=1 define the boundaries of different flame regimes of premixed turbulent combustion. The line $\acute{u}/S_L$=1 separates the wrinkled flame from the corrugated flame. The line Ka_δ =1 separates the thickened flame (thin reaction zone) from the broken reaction zone. The regime below the line Re_T =1(i.e. Re_T <1) is called the laminar flame regime whereas regimes above the line Re_T =1 (i.e. Re_T>1) is called the turbulent flame regimes. The flame regime boundaries and flame regime characteristics are shown in Figure 11.

In the wrinkled flamelet regime, the turbulence levels are not significant enough to alter the characteristics of the flame fronts. The separation of the thickened flame regime from the corrugated flame regime could be explained with the Kilmov-Williams hypothesis where $\eta = \delta_L$. Although there is some doubt about this assumption, many researchers have found this as handy. It is because this assumption allows them to compare their experimental results with simulation.

In general, for a specific test condition, the turbulent flame thickness is higher than the laminar flame thickness. It is because the flow dynamics and thermal diffusion are dominating at turbulent combustion. Many researchers have investigated the flame regimes' characteristics at different flow conditions and combustor geometries. Yuen and Gulder [30] have investigated the flame characteristics of methane-air and propane-air using PIV and Rayleigh scattering. They found that the flame thickness increases with the increase in turbulent RMS velocity. Tamadonfar and Gulder [31] have found that the flame front thickness increases with the increase in equivalence ratios, however, it decreases with the increase in Ka. Another researcher has found the opposite results, for instance, the flame thickness decreases at lower Ka and turbulence values [32]. Therefore, it is obvious that the flame regime characteristics especially the thin reaction zone is not well studied. More intensive investigation is needed for a better understanding of the thin reaction zone.
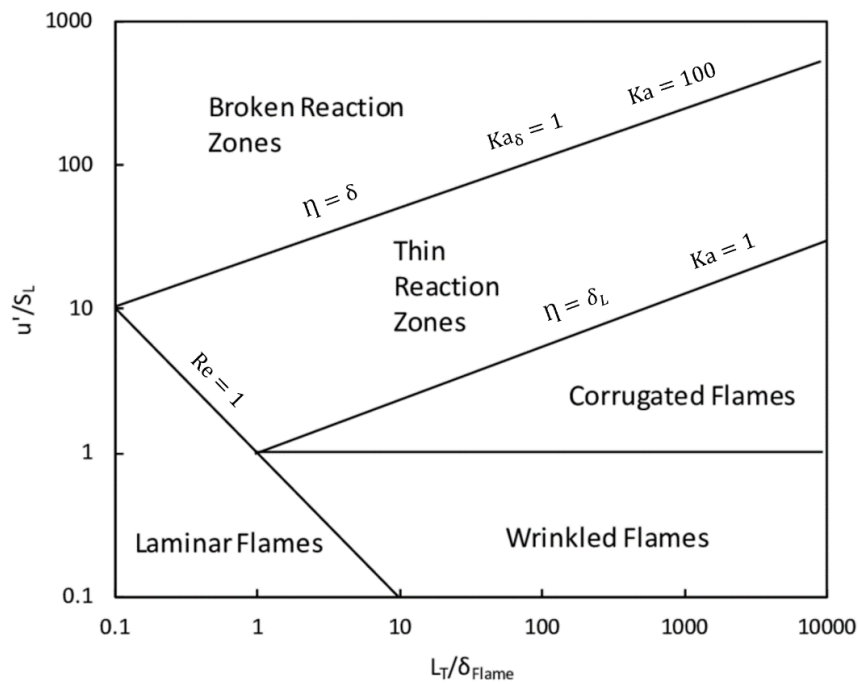
Figure 10. Borghi-Peter's Diagram [25]

18

Flame Regime	Re_T	Da	Ka	u'/S_L	δ_L/η	Graphical Illustration of Flame Fronts
Wrinkled Flame	>1	>1	<1	<1	<1	
Corrugated Flame	>1	>1	<1	>1	<1	
Thickened Flame (Thin-Reaction Zones)	>>1	≥1	>1	>>1	>1	
Distributed Flame (Well-Stirred Reactor)	>1	<1	>1	>1	>1	

Figure 11. Flame Regime Characteristics [3]

2.4 Laser Diagnostics for High-speed Combustion

The laser diagnostic techniques are non-intrusive techniques that give instantaneous information about flow and flame characteristics. In laser diagnostic techniques either non-reacting seeding particles or a high-intense laser light sheet is used to illuminate the flow and flame fields. These techniques help to acquire data with high resolution and high accuracy. The higher sampling rate and simplicity of these techniques enable researchers to diagnose the flame in extreme turbulence. The diagnosis of the reacting gas-mixture combustion using the traditional data acquisition technique is not easy. It is because the reacting gas combustion involves both timescale and chemical scale. The laser diagnostics techniques can resolve this issue [4], [34]. Also, instantaneous changes in velocity and temperature field could be acquired using laser diagnostics. This information is very instrumental in the study of turbulent flame propagation [4]. The most widely used laser diagnostic techniques are Raman spectroscopy, Rayleigh scattering, Particle image velocimetry (PIV), Laser doppler velocimetry (LDV), Planar laser-induced fluorescence (PLIF), etc. All these techniques are promising, however, for this study, only the PIV and PLIF have been used. The system description, data acquisition and post-processing using the PIV and PLIF systems will be discussed in the following section of this thesis.

2.4.1 Particle Image Velocimetry (PIV)

Particle image velocimetry (PIV) is a doubled pulse laser system. It gives the instantaneous velocity distribution of the flow field. It traces the displacement of the flowing particles in a short duration of time. After that, PIV uses the time and displacement of particles and generates the velocity fields. Since PIV gives the velocity profiles for the entire cross-section, therefore, it is a whole-field technique. It provides the flow-filed mapping of the fluid. Unlike the ordinary flow visualization technique, PIV provides both the qualitative and quantitative description of the flow field. Thus, PIV results are used to validate the computational results. Also, flexibility in application, versatility, microsecond exposure time, whole-field imaging and higher accuracy have made the PIV system extremely important for flow-filed study. The PIV has been used for the study of unsteady flow, supersonic and hypersonic flows, explosions, flame propagation, turbulence, etc [35].
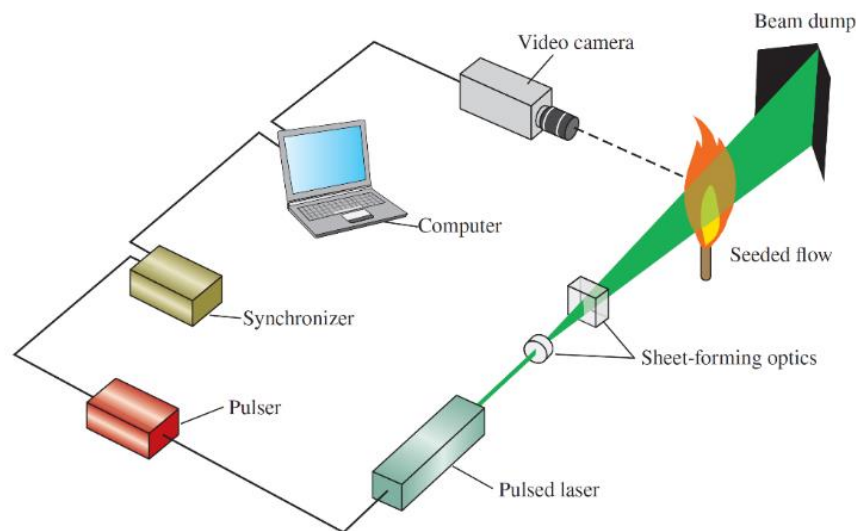
Figure 12. A typical PIV system used to study flame stability [35]

A typical PIV has three important components: flow tracer particles, laser light sources, and high-speed imaging. The first step is to choose suitable seeding particles. A double pulse laser is used to send two laser light signals to the target area. A charged coupled device or high-

20

speed photographic camera is used to detect the light scattering pattern from those laser pulses. The magnitude of particle velocity is determined from $\Delta s / \Delta t$.

The selection of seeding particles is crucial as the accuracy of PIV is also affected by them. Seeding particles must be able to trace the flow path lines. Therefore, the density of the seeding particle (ρ_s) should be equal to the fluid density (ρ_f). Thus, seeding particles should be neutrally buoyant. Also, their size should be small compared to the size of the fluid particles. For high-speed flows, very small size particles should be used. Silicon carbide particles (~ 1.5 μm) and alumina (1 μm) are suitable for high-speed liquid and gas flow. For high-temperature gas flow, titanium dioxide particles (~ 0.2 μm) are normally used. For low-temperature medium, polystyrene latex particles (~ 1.0 μm) are suitable. Olive oil or silicon oil bubbles or droplets could be used as the seeding particle for gas flow [36].

2.4.2 Planar Laser-Induced Fluorescence (PLIF)

Planar laser-induced fluorescence (PLIF) is a technique widely used to measure the temperature or molecular concentration maps for liquid and gaseous flow, reacting and non-reacting flows. In this process, a high-power laser light source is used. The laser light source passes through a set of light-sheet optics before it hits the target plane. The laser light source illuminates the target plane (shown in Figure 13). The laser wavelength is chosen based on the energy transition of the molecular species of interest. Once the laser light is targeted to the plane of interest, the light is absorbed by the combustion molecules/species. Therefore, the collision between the molecules increases and they transformed into a higher energy state. After that, the energy is redistributed to the nearest molecules. In the redistribution process, excess energy is released as photons. These photons are commonly referred to as Fluorescence. Fluorescence has a higher wavelength relative to that of the excitation. When fluorescence is emitted from the molecules, there is a chance of having interference from the scattered laser

light. Normally a spectral filter is used in front of high-speed cameras to minimize this effect. A schematic of the mode of energy transfer from the excited molecules is shown in Figure 14. The detection of this fluorescence is further used to (i) understand the spectral behavior of the combustion radicals, (ii) visualize the flame front, (iii) understand the ignition phenomena, (iv) understand the fuel injection, atomization, and distribution, etc.
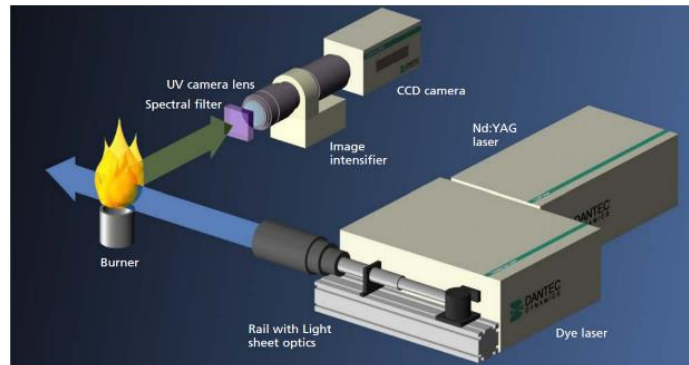
Figure 13. A typical LIF system for combustion analysis [37]
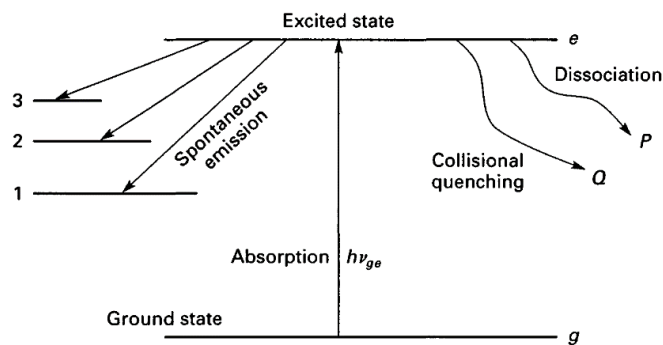
Figure 14. Modes of energy transfer from an excited state [38]

The species such as OH, CH, CN, NH, NO, CH_2O, etc are widely used for LIF measurements. Their excitation wavelengths are presented in Table 1.

Table 1. The absolute wavelength of combustion species [3]

Species	Wavelength (nm)
OH	306
CH	431
NH	336
CN	388
CH_2O	320-360
NO	226

PLIF systems have many limitations. It depends on the nature of the species. If two or more species must be excited, multiple laser and camera units must be used. If the laser trigger rates reach the kHz level, the pulse energy drops. Lower repetition rates provide high pulse energy; however, it reduces the time resolution of the measurements. The fluorescence is a strong function of species concentration. Therefore, it is difficult to excite some of those species. The detection gets more difficult with the addition of noises, reflections, soot, etc [27]–[29]. The high spectral filter is used to eliminate unwanted laser reflections. However, background radiation might get through the filters if radiation signal resonance with the PLIF. The laser pulse and PLIF emission are fast processes, therefore, they must be correctly synchronized. Besides, the detection system such as camera and intensifier units generate noises which might affect the overall synchronization process [11]. Because of these difficulties, special care needs to be considered in the selection of the PLIF system.

2.4.2.1 OH PLIF

The flame front is the area of the highest thermal energy. The PLIF is used to detect the flame fronts. There are many tracers (OH, CH, CH_2O, CN, NH, etc) that have been widely used in combustion research [28]. In most of the hydrocarbon-air combustion, OH form as an intermediate species. It forms when two H_2 radicals hit the O_2 molecules. The OH is formed by a fast two-body collision reaction. The OH radicals are then consumed by the slower three-body recombination reactions. Therefore, the life of OH radicals is long. Also, they could be convected away to a new place because of the flow turbulence.

The OH radicals normally present in the lean regions within the flame where the chemical reactions are completed. In premixed combustion, the OH is slowly consumed by the burned gases. They even stay at equilibrium concentrations state. Therefore, OH PLIF could be used to separate the unburned gas zones from the burned gas zones [11]. In non-premixed

combustion, the OH shows a wider flame front compare to the other radicals such as CH, CN, etc.

The OH PLIF uses a pump-dye laser combination. The laser light is generated by the pump laser. It then goes through the dye laser and frequency doubling unit before it fully tuned for OH radicals. The OH PLIF was first used for 2D visualization of naturally occurring flame [39]. It has been extensively used in the last few decades because of the numerous advantages. However, it has some limitations too. Most of the OH-PLIF research has been done for the open flame system such as for Bunsen burners, Flat flame burner, spiral burner, etc. Therefore, the effect of background noises, reflection has not been considered [11], [28]. There are very few researches exist where OH-PLIF is used for closed/enclosed flame system, however, they mostly limited to low repetition rate [3],[40]. A. Acosta-Zamora [11] and Martin Alejandro De La Torre [41] have done some preliminary research on the closed flame system using the OH-PLIF. Apart from all these, the application of OH PLIF at higher Ma is not feasible [3], [42]. The advantages and limitations of the OH-PLIF have already been discussed in chapter one. Further information on the OH-PLIF system could be found elsewhere [11],[28].

2.4.2.2 CH-PLIF

CH species could be used to detect the actual flame fronts. For instance, Vagelopoulos and Frank [14] experimentally concluded that the CH concentration coincides reasonably well with the heat release zone. It infers the adequacy of CH species as a flame front marker. The tracing of CH species is not as they have low radical concentration, narrow-band spectral and short life. However, they present during the main course of combustion and near the flame fronts, thus CH is also considered for flame front tracing. CH-PLIF has been used for different combustion systems. Different detection schemes have been used for CH detection, for example, A-X~430nm, B-X~390nm, and C-X~314nm, etc [9], [43]. Miller et al [44] have

used the CH PLIF diagnostics to understand the reaction zone behavior of turbulent premixed flame and diffusion flame. Jiang et al [45] have investigated the relationship between flame extinction and flame wrinkling using the CH-PLIF. Yoshida et al [46] have used the CH PLIF and investigated the turbulent premixed methane-air combustion behavior at elevated pressure.

Since 1950, much research has been done on CH PLIF, none of them were able to detect the absolute CH signal without the noises and overlapping resonance. For example, Chou et al [47] used a laser perturbation of methane flame to understand the high-temperature reaction of CH. Similarly, Tsujishita et al [48] used a PLIF system to visualize the CH molecules present in the turbulent flame. Although those researchers were almost close to the detection of CH fluorescence, however, they failed because of their system limitations. Most recently Carter's group made success in detecting the CH using a new band called C-X (~314 nm) [9], [43], [49]. The wavelength of multiple species present during the combustion is listed in Table 2.

Table 2. The excitation wavelength of multiple radical species [50]

Excitation Wavelength	Radical Species	Transition			Energy^a cm^{-1}
334.09	NH	A-X	(0,0)	$R_3(4)$	29932.71
	CN	B-X	unknown	$\Delta v=2$	—
315.10	OH	A-X	(0,0)	$P_1(13)$	31726.79
	NCO	B-X	000-000	unknown	—
314.85	OH	A-X	(1,1)	$Q_2(5)$	31752.72
	NH	A-X	(2,1)	$P(17)$	—
	NCO	B-X	000-000	R_1 head	—
314.66	OH	A-X	(1,1)	Q_2 head	—
	NH	A-X	(1,0)	$P(22)$	—
314.38	OH	A-X	(0,0)	$P_1(12)$	31799.49
	CH	C-X	(0,0)	$Q_2(10)$	31799.4
				$Q_1(11)$	31799.6
312.22	OH	A-X	(0,0)	$Q_2'(15)^b$	32019.34
			(1,1)	$R_1(6)$	
	NH	A-X	(2,1)	$P_1(12)$	32019.38
	CH	C-X	(0,0)	$R_1(7)$	32019.32
	CN	B-X	unknown	$\Delta v=3$	—

Chapter 3: Experimental Setup and Methodology

In this chapter, the experimental setup, experimental procedures, methodologies, experimental challenges and solutions, test matrices and post-data analysis will be discussed.

3.1 Experimental Setup

In this section, the experimental setup, procedures, methods relevant to this thesis work are provided. For this research, methane-air is used as the reactant. H_2-air is used as the pilot mixture. The full description of the experimental setup could be found in [2], [51]. The turbulent premixed flame behavior is investigated at different flow rates (12CFM, 25CFM, and 50CFM) and fuel concentrations (Φ=0.6 to 1.2). The combustor and subsystems, pilot flame system, combustor and exhaust cooling systems, high-speed laser diagnostics (PLIF and PIV), control system, experimental challenges and solutions, and post data analysis techniques will be discussed in the following sections of this chapter.

3.1.1 Combustion Chamber

The combustor is made of 304 SS material and it can hold a maximum of 90 psi (6 bar) and 500K. Two 1" quartz windows are placed on the two external sides of the combustor for high-speed camera sensing. One 1" quartz window is placed on the top of the combustor so that a high-laser sheet can illuminate the target plane. All the quartz windows were designed with a 3.5 factor of safety. The methane and air were introduced to the mixing chamber. The air is injected through the axial injection port, whereas the methane is injected through a tangential injection port. This premixed mixture passes through the square cross-section flow path and then gets into the combustion chamber. When the mixture flows over the backward-facing step, it experiences a sudden expansion in the flow path. Because of this expansion (1:2), there is a formation of many low-speed recirculation zones inside the chamber. There is a formation of a shear layer at the edge of the step. The detailed flow stabilization technique is

already been discussed in chapter 2. The combustor is a modular setup. Therefore, the height of the backward-facing step was designed based on the dimension of the combustor body. However, the height of the step may be changed in the future to see how that affects the flow stabilization and reattachment length.

The ignition source is placed in the recirculation zone. The hydrogen-air mixture is used as the pilot flame subsystem. The Pilot flame is used to ignite the combustible mixture (methane-air) inside the combustor. During the combustion, the temperature of the combustor body increases very rapidly. Dynalene solution is used as the coolant for the combustor body. The exhaust gases are then passing through the exhaust chamber. In the exhaust chamber, the evaporative water-cooling system is utilized. After that, the cooled exhaust is sent to the atmosphere through the exhaust fan. The overview of the combustor assembly is shown in Figure 15. The cross-sectional presentation of the combustor is shown in Figure 16.
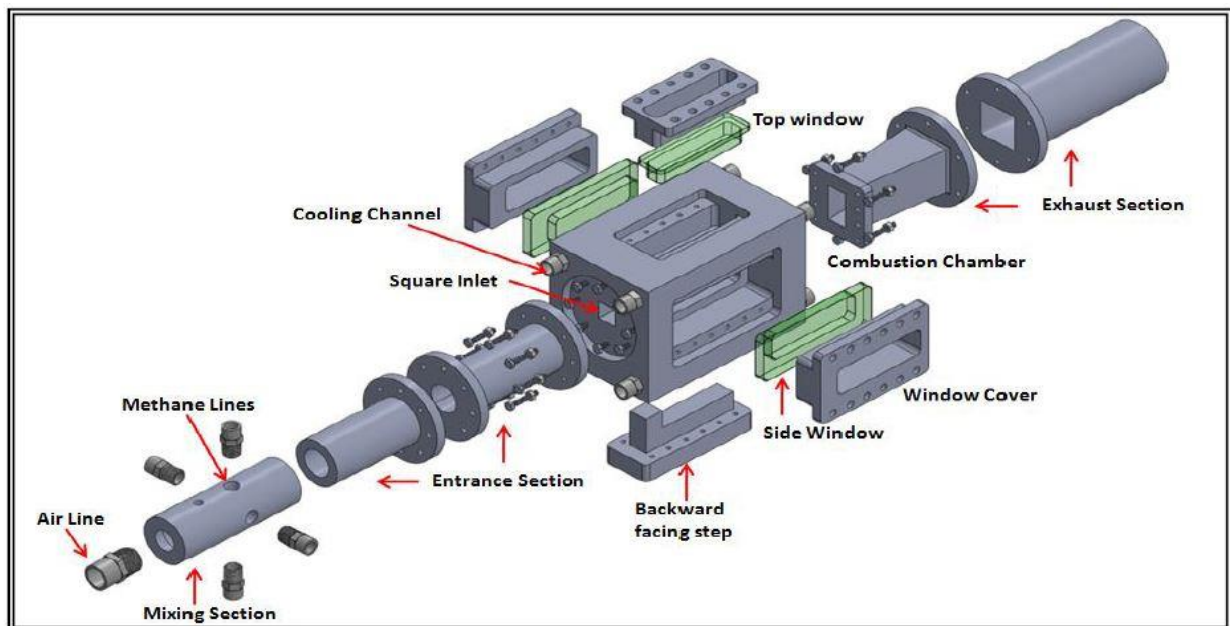
Figure 15. Exploded view of the combustor assembly [11], (Mixture is going from left to right direction)
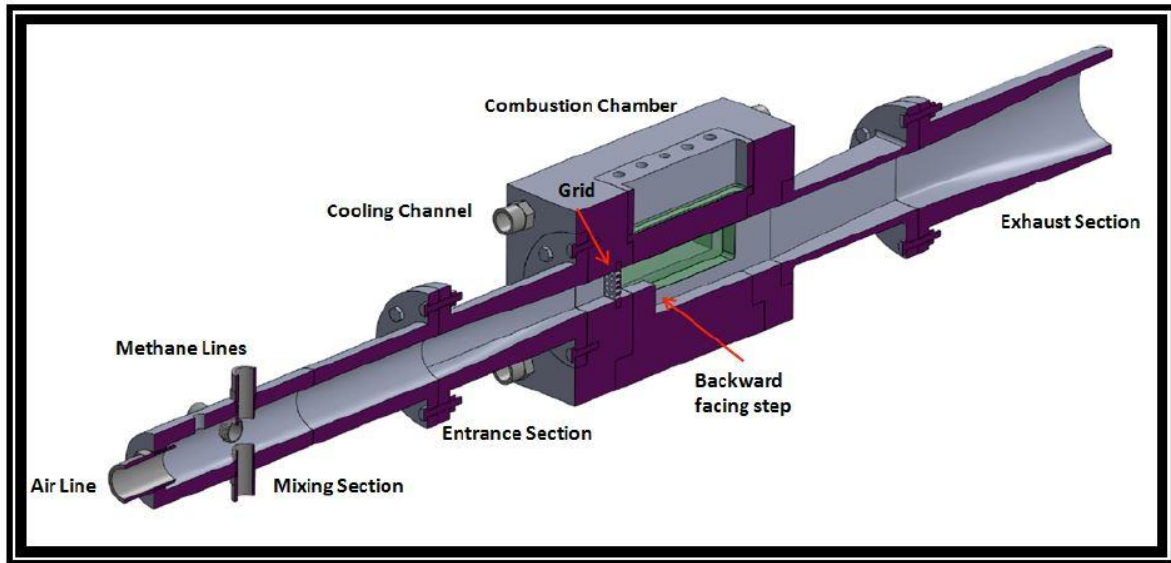
Figure 16. The cross-sectional view of the combustor [11], (Mixture is going from left to right direction)

The grid is located at the inlet of the combustor. The purpose of using the grid is to create homogenous isotropic turbulence inside the combustor body. The grids also act as a flashback arrestor which protects the incoming unburned gases from the sudden shock. Al-6061 is used to fabricate the grids. It is chosen as they are not in contact with the flame or combustible mixture. The grids are shown in Figure 17. Two different hole diameters (1.5 mm and 3mm) and blockage ratio of 46% to 48% is used for this research. The grid's geometries are limited to the machinability of the materials and placement ability inside the combustor. The summary of the grid geometries is listed in Table 3.
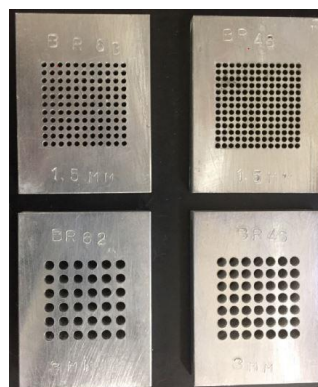
Figure 17. The grids used to generate the isotropic turbulence inside the combustor [11]

Table 3. Grids geometries used in this research

Grid #	Blockage Ratio (BR)	Hole Diameter (D)	Effective Area (mm²)
1	48%	1.5mm	335.5
2	46%	3mm	348.4
3	63%	1.5mm	238.7
4	62%	3mm	245.2

3.1.2 Main Delivery Lines

Methane and air are used as the main component of the delivery system. An industrial compressor with a capacity of 190 CFM at 140 PSIG is used to provide high-compressed air to the system. An industrial dryer and high accuracy filter are used to make the air dry and clean. For better control of the system, each line is fitted with control valves, thermocouples, pressure transducers, flow meter, etc. Methane is supplied to the system using 4 k bottles. Air is controlled using a control valve and a high flow regulator. Methane and air are mixed at the mixing chamber so that only the premixed mixture can enter the combustor. The detailed schematic of the experimental feed lines and control systems could be found in [11].

3.1.3 Subsystem Delivery Lines

An ultra-high pure H_2 is supplied to the main system from industrial K-bottle. The H_2 is chosen for this research because of its high flame speed. The high-flame speed helps to avoid pilot flame blowout by the main flow. The pilot flame is in the recirculation zone so that better ignition could be made at higher-order turbulence. The location of the pilot flame inside the combustor is shown in Figure 18. H_2 and air are mixed in the mixing chamber. After that, it enters the ignition chamber. The common car spark (LS2 MSD ignition coil, 60 KV) is used as the ignition source to the ignition chamber. As the Re increases, the main flow rate and pilot flame flowrate increase too.
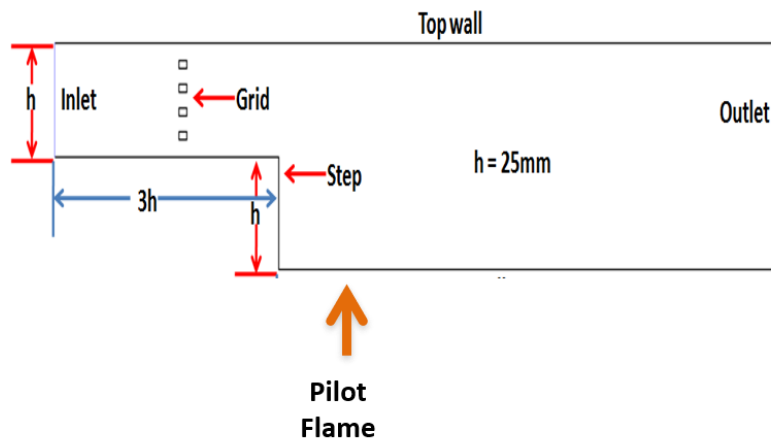
Figure 18. The location of pilot flame and grid

3.1.4 Experimental Flow Control Systems

All valves and control line hardware and instrumentation are connected to the main switch panel. The main switch panel houses mechanical valves that control the individual valves (shown in Figure 19). The instrumentation is powered through the AC and DC power. The main control panel has two modes of control: Manual and software controlled. In the manual control system, mechanical switches are used to control each switch. Also, manual control has two emergency switches. The first emergency switch is used to cut off the gas delivery line whenever needed. Another switch is used to cut off the water supply from the exhaust. The data acquisition system is equipped with PCI cards that read the voltage input from the instruments. The PCI cards with mechanical relay are used to control the valves. The LabVIEW system used in this research has two controlling units, one is numeric indicators and another one is Boolean control. These units are used to monitor and control each component of the delivery system. The LabVIEW control user interface is shown in Figure 20. The detail of the DAQ controlled block diagram, LabVIEW interface, PCI controlled cards, mechanical switch control valves could be found in [11].

Figure 19. The mechanical switch control panel used in this research [11]
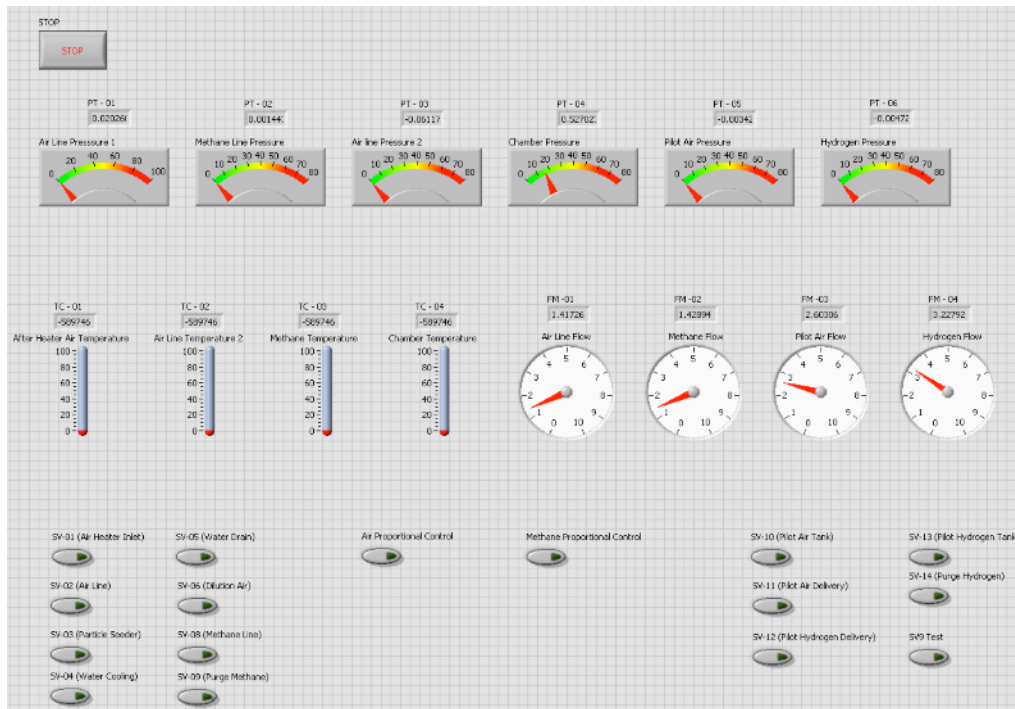
Figure 20. LabVIEW control system [11]

3.1.5 Time-Resolved Particle Image Velocimetry (TR-PIV)

For flow characterization, Litron LDY15-1000 dual power Neodymium-doped Yttrium

Lithium Fluoride (Nd-YLF) with a pulse energy of 15 mJ is used. For the camera to be able to

capture the signal, the light source needs to perpendicular to the camera direction. For this, the

laser light head is placed at an elevated height and laser light is redirected at an angle of 45°

into the laser sheet optics. A laser sheet with a plane area of 1mm×52mm×25mm is produced once the laser beam passed optics. Compressed air driven fine alumina particle (1 µm) is introduced to the chamber far upstream so that the crossflow generation is not affected. A 10 kHz high frame rate high-speed camera (speed sense 9070 CCD) with a resolution of 598×288 pixels (12 bits) and an interrogation area of 73×35mm is used to sense and capture the scattering pattern from the particles. A BNC-575-8 timer-box is used to synchronize the camera with the laser pulse. The Dantech dynamic studio is used for overall synchronization and post-processing. The schematic of the PIV components is shown in Figure 21.

A quarter turns manual valve is used to transfer air into the main airline. After that, a 120 V AVCO E03/05 8P14 solenoid valve and a manual valve is used to set the airflow into the system. An analog flow meter (Hedland variable area flowmeter) with a flow rate range of 25-250scfm and a pressure range of 40-120 psi ± 2% is used to measure the airflow rate. A doubled pulse laser is used to introduce two laser pulses separated by a known time difference. The camera records the two instances when the particles travel the fixed distance. The images are then subdivided into two sections called interrogation areas. During the post-processing, the software does a cross-correlation to all interrogation areas and generates the velocity fields. Statistical analysis and further post-processing help to generate other flow characteristics such as turbulence intensity, vorticity, etc. The PIV data analysis process is shown in Figure 22.
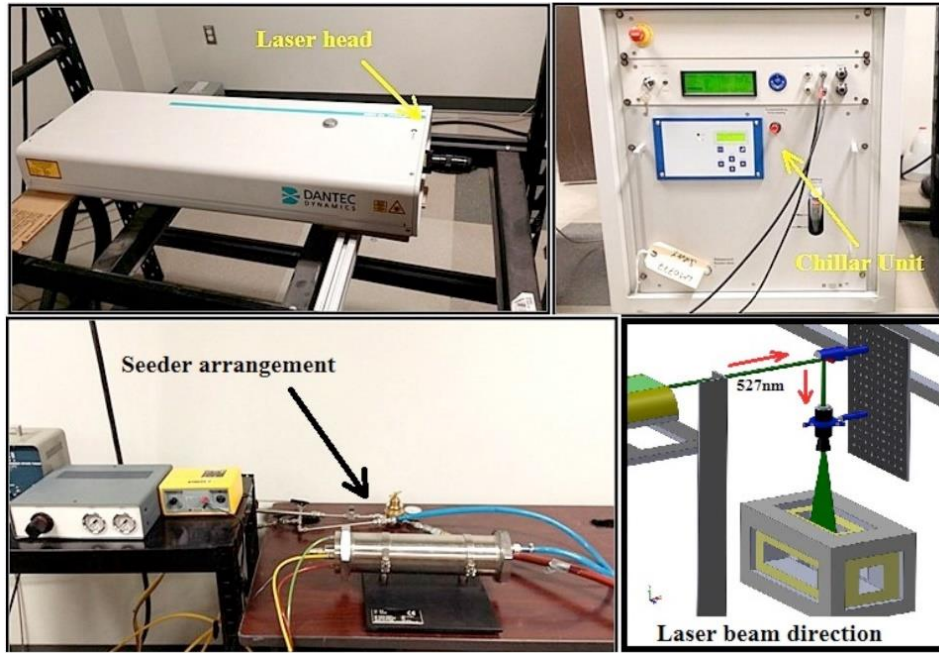
Figure 21. PIV laser head, chiller unit, seeder arrangement, and laser beam direction
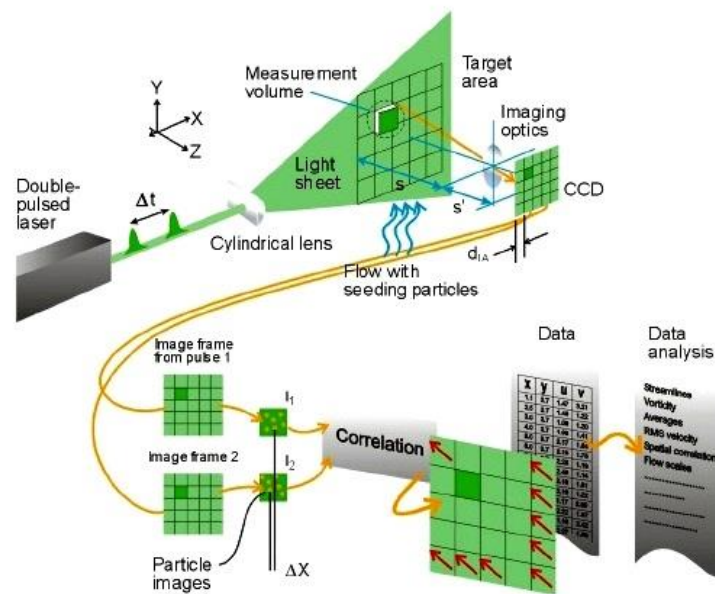
Figure 22. The PIV data analysis process (Taken from Dantec dynamic website)

3.1.6 Planar Laser-Induced Fluorescence (PLIF)

A 10 kHz high-repetition-rate planar laser-induced fluorescence (PLIF) system is used for flame characterization. The PLIF system comprises three main sections: a pump laser (Q switched DPSS pump laser, Nd-YAG Edge wave IS series laser), a dye laser (Radiant Dyes

HighRep dye laser) and a high-speed charge-coupled device (CCD) camera integrate with an intensifier unit. The pump laser generates 20W laser power at 10 kHz resulting in a laser pulse energy of 2 mJ/pulse. The pump laser pumps a 532nm laser beam through the frequency doubling unit and oscillator unit of the dye laser. The dye laser uses a DCM-ethanol dye (0.55 g/L) and a BBO crystal assembly to adjust the system wavelength to the CH excitation range.
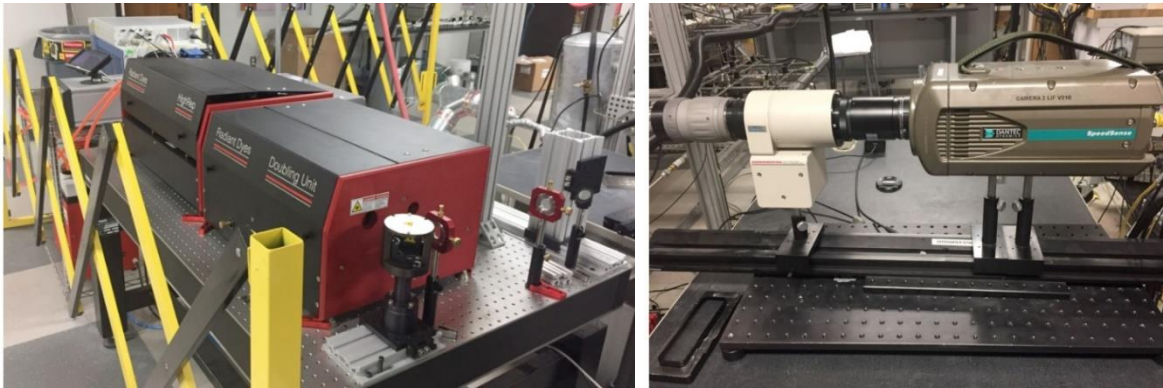
Figure 23. The schematic of PLIF assembly (left) and Intensifier unit (right)
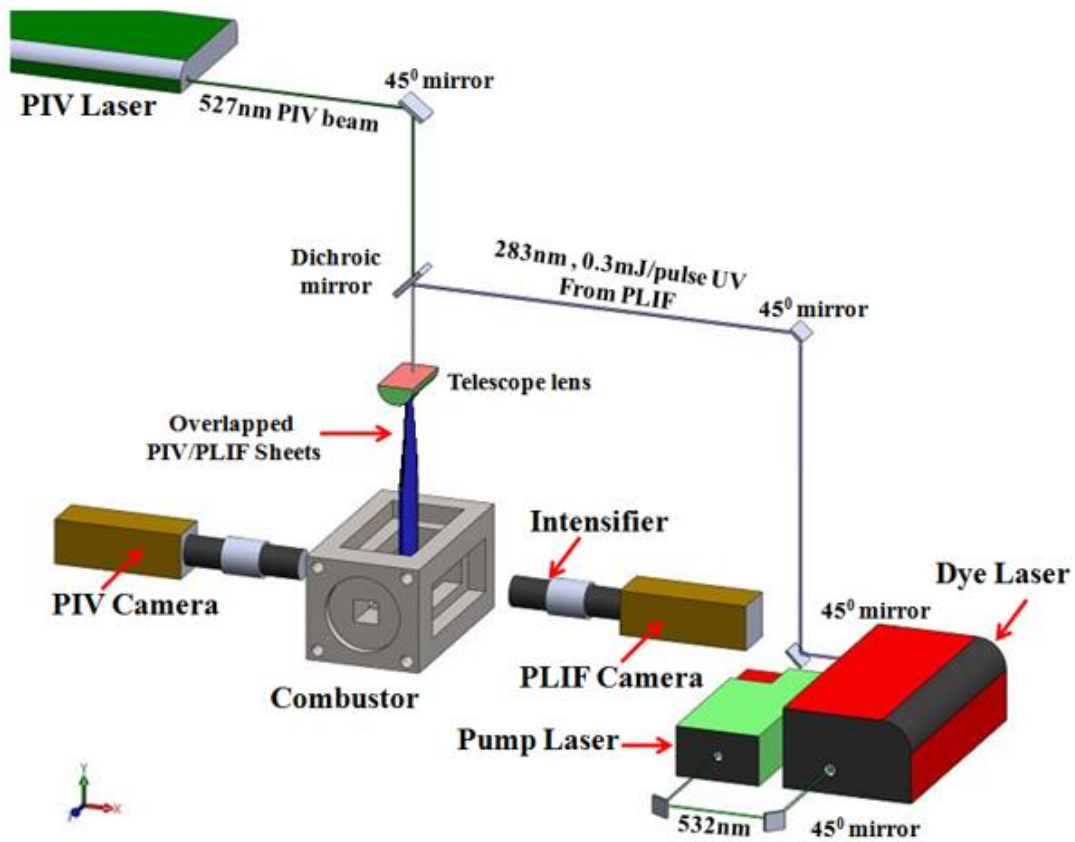
Figure 24. The integration of PLIF and PIV systems

A wavelength of 314.415 nm was found to be the best for CH C-X band excitation. High frame rate CCD camera (Speed sense 9070 series) integrates with a Hamamatsu intensifier unit is used to detect the flame fluorescence. The camera can provide a maximum resolution of 105.48 um/pixel at 10 kHz. The intensifier unit equipped with two more parts: a Cerco 100mm f/2.8 lens to facilitate the detection, and a UG-5 colored glass filter to filtering out the noises coming from visible light. The complete schematic of the PLIF system is shown in Figure 23. All the components of the PLIF system are synchronized to the control and data acquisition system using a BNC timer box. Dantec Dynamic software is used to monitor, control the signals and acquire real-time data. The both PIV and PLIF systems are integrated so that that measurement of flow and flame characteristics are not interrupted. The integration of both laser systems with the combustor is shown in Figure 24.

The PLIF system connection diagram shown in Figure 25 shows how the pump laser, dye laser, chiller, camera sensing unit, intensifier unit, timer box, oscillator, etc are integrated. A Dantec Dynamics system is used to control both PIV and PLIF signals. This software is also used to acquire and processing of PIV and PLIF images. The system is capable of simultaneous operation of PIV and PLIF laser. However, in this research, the laser systems are operated separately. The complete overview of the high-speed combustor, the laser diagnostic systems, PLIF system electric connection lines, Dantec Dynamics software connection lines used for this work could be found elsewhere [11].
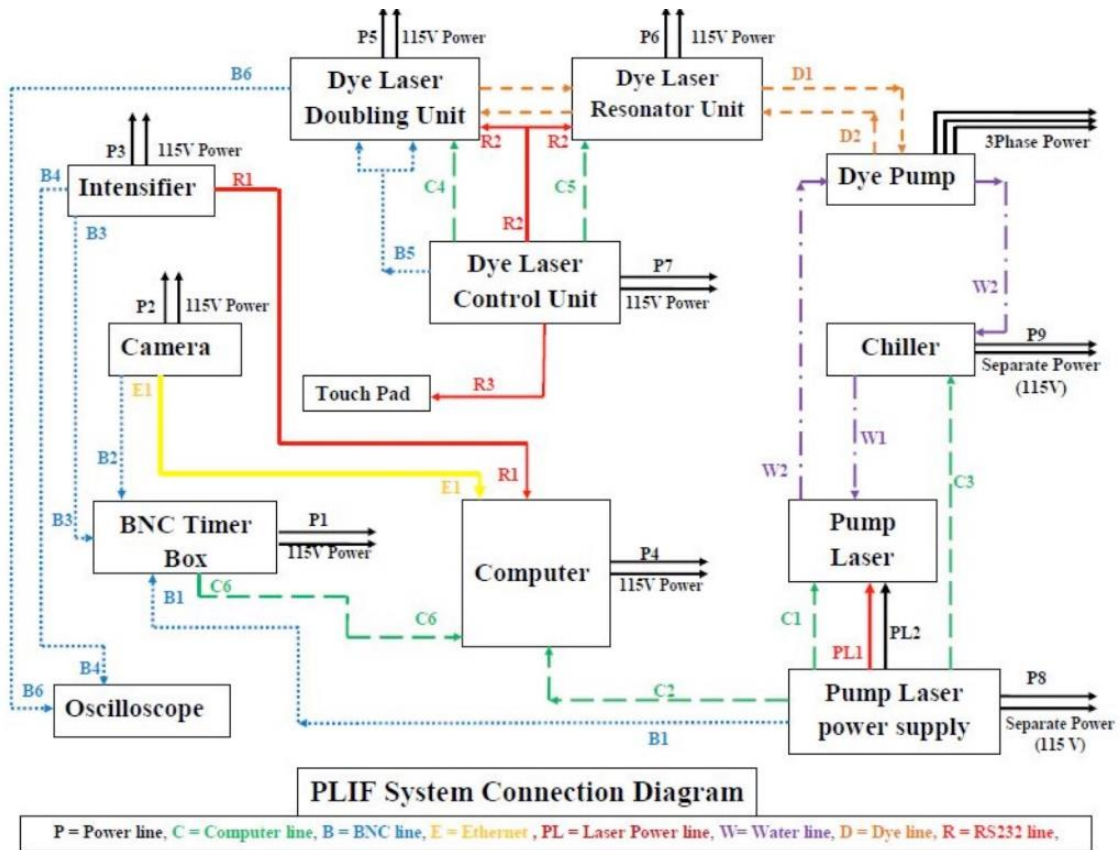
Figure 25. PLIF system connection diagram

3.2 Test Operating Conditions

The research has been done at different bulk flow rates with Re =15000, 30000 and
64000. Grids with different blockage ratios (BR%) are used to introduce the turbulence inside
the combustor. Table 4 shows the bulk mixture velocity and flow rates at different Re's.

Table 4. Overview of the flow and associated mixture flow rates

Reynolds Number, Re	Combustion Mixture	Flow Nature	Mach Number, M	Bulk Mixture Flow Rate LPM	CFM	Bulk Mixture Velocity (m/s)
15000	Premixed methane-air	Turbulent	0.027	353.7	12	10
30000			0.055	707.3	25	20
64000			0.12	1508.9	50	40

36

The operating conditions are set based on the Reynolds numbers (Re), equivalence ratios (ϕ), and associated flow rates of air and methane. The Reynolds number (Re) is calculated using the following equation:

$$Re = V_{mixture}\,L/\nu_{mixture} \tag{24}$$

Where, $V_{mixture}$ is bulk mixture velocity, $\nu_{mixture}$ the is the logarithmic bulk mixture viscosity and L is a characteristics dimension of the combustor inlet. The bulk mixture velocity, $\nu_{mixture}$ is calculated using the following equation,

$$log\ \nu_{mixture} = (x_{air} * log\ \nu_{air}) + (x_{CH4} * log\ \nu_{CH4}) \tag{25}$$

Where, ν is the kinematic viscosity and x is the mole fraction in the mixture. For each of the pre-set Re, bulk mixture flow rates are calculated. Afterward, the actual air-methane ratios are calculated using the pre-set equivalence ratios and the stoichiometric air-methane ratio. Subsequently, the moles of the mixture and mixture components are calculated. Finally, the flow rates of methane and air are generated. Table 5 shows the test matrix used for this specific research.

Table 5. The test operating conditions

Re	ϕ	F/A)$_{actual}$	A/F)$_{actual}$	Q$_{bulk}$ (LPM)	Q$_{methane}$ (LPM)	Q$_{air}$ (CFM)
15000	0.6	0.06	15.9	353.7	21.0	11.7
	0.7	0.07	13.6		24.2	11.6
	0.8	0.08	11.9		27.4	11.5
	0.9	0.09	10.6		30.5	11.4
	1.0	0.11	9.5		33.6	11.3
	1.1	0.12	8.7		36.6	11.2
	1.2	0.13	7.9		39.6	11.1
30000	0.6	0.06	15.9	707.31	41.9	23.5
	0.7	0.07	13.6		48.4	23.3
	0.8	0.08	11.9		54.8	23.0
	0.9	0.09	10.6		61.1	22.8
	1.0	0.11	9.5		67.2	22.6
	1.1	0.12	8.7		73.3	22.4
	1.2	0.13	7.9		79.2	22.2
	0.6	0.06	15.9		89.5	50.1

64000	0.7	0.07	13.6	1508.93	103.4	49.6
	0.8	0.08	11.9		117.0	49.2
	0.9	0.09	10.6		130.3	48.7
	1.0	0.11	9.5		143.4	48.2
	1.1	0.12	8.7		156.3	47.8
	1.2	0.13	7.9		168.9	47.3

Before each test run, both PIV and PLIF systems have synchronized with the camera, intensifier unit, etc. The synchronization was made so that the flow and flame characteristics could be captured without sacrificing their evolution. The synchronization parameters are optimized based on several trials and post-processing of the data. The operating parameters for PIV and PLIF systems are listed in Table 6 and Table 7.

Table 6. The operating criteria for synchronization of the PIV system components

Controlling Parameters	Magnitudes with Units
PIV Laser	Nd-YLF Type, 10 kHz
Capacity and Pulse Energy	527 nm and 15 mJ/pulse
Area of Laser Sheet	75 mm wide and 0.1 mm thick
Resolution	640 x 480 resolution at 10 kHz
Interrogation Area	73 mm x 36 mm
Seeding Particles	Alumina (1μm)
Driving Force	Compressed Air at 70 psi
Camera and Intensifier Unit	CCD Camera (Speed Sense 9072) + Nikon 60 mm lens and a 532 nm light filter

Table 7.The operating criteria for synchronization of the PLIF system components

Controlling Parameters	Magnitudes with Units
Pump Laser Capacity and Pulse Energy	532 nm and 2 mJ/pulse
Dye Laser Maximum Output and Pulse Energy	355 nm and 0.2 mJ/pulse
Camera Exposure Time	70μs
Intensifier Parameters: Gain, Gate Delay Time, Gate Pulse Width	700-750, 10ns and 15 μs-100 μs
Excitation Wavelength for CH-CX Band	310-320 nm 314.415nm was used in this study

3.3 Experimental Challenges and Solutions

3.3.1 Experimental Challenges in PLIF System

Various difficulties are encountered during the experimentation and post-processing stages. The first challenge is to focus a concentrated laser sheet onto the interrogation area inside the combustor. The second challenge is to get the right wavelength for CH C-X band excitation. Wavelength scanning has been performed and an optimum wavelength of 314.415nm is set for CH C-X excitation. The next challenge is to detect and extract the CH signal from the flame as it overlaps with OH. The OH signal is reduced by optimizing several cameras and intensifier unit parameters (listed in Table 3). However, the optimization of both camera and intensifier parameters are subjected to change with flow turbulence. The flame profiles are detected and recorded using the Dantec dynamics studio software. The recorded raw images are then post-processed for further investigation.

3.3.2 Solution Executed in PLIF Image Processing

Since the combustion took place inside a windowed combustor, the raw images have witnessed an unwanted laser reflection from the walls, soots and background noises. Besides, the post-processing of the raw images shows a scaling error. It happens because of the shifting of the flame across the interrogation area. To address these difficulties, MATLAB image processing codes are developed. To filter the unwanted laser reflections and background noises, the MATLAB code is adjusted to the flame image pixel matrix. This adjustment also helps to protect the area of interest from the external influence. Also, the MATLAB code adjusted the flame shifting by changing the interrogation areas. To make the flame profiles more visible, a separate code for color-scaling is implemented. At the primary image processing, the base images (without flame) are subtracted from the raw images (with flame). Consequently, the primary processed RGB images are converted to the grayscale and webinar scale. The

colormap is then implemented on both grayscale and webinar scale images. It is found that the flame profile generated by grayscale colormap shows higher resolution and almost no background noises compared to the webinar colormap. For this reason, the grayscale induced HSV colormap is reported in this paper. Besides, the flame profiles are magnified in each run. A magnification factor of 2 to 4 is chosen for the conditions tested in this research. The magnification makes the flame profiles more visible and it does not disturb the flame structures.

The flame edges give a more in-depth understanding of the flame evolution. To generate the flame edges, a separate MATLAB code is established. The code first flipped the HSV colormap contours. The flipped RGB images are then converted to Gray images. Consequently, the images are binarized. Afterward, different edge detection commands are implemented. However, for simplicity, in this paper, flame edges detected by the Canny command is presented. MATLAB imcomplement command and Canny command gives a final flame edge profile. Figure 26 shows the complete view of how the colormap and flame edge generated in the post-image processing.
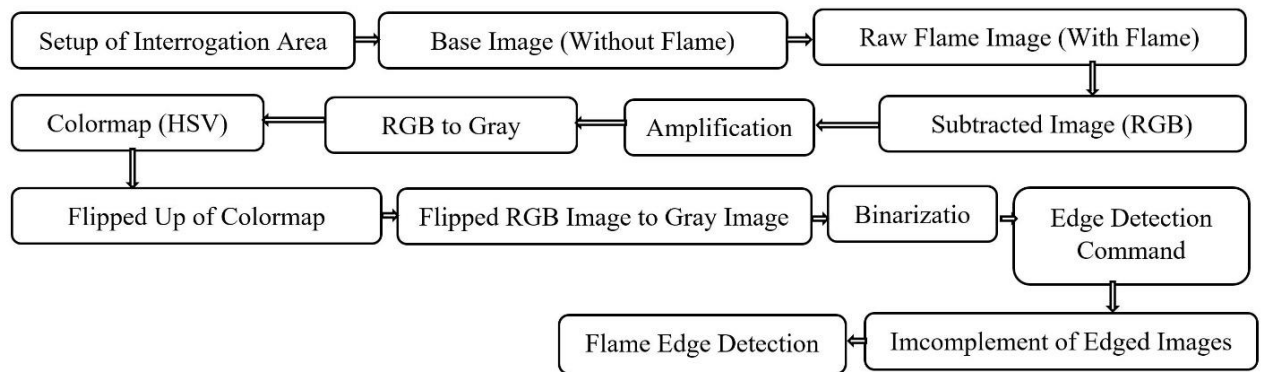
Figure 26. Flow chart of MATLAB based image processing codes

3.3.3 Experimental Challenges in PIV Setup

The main challenge in the PIV system is to redirect the laser beam to the laser optics sheet. For this, the laser head is elevated vertically, and laser light is redirected by 45° towards the laser optics. Once the laser light gets into the combustor, it creates a laser plane area of

40

1mm×52mm×25mm. Another challenge is to send the tracer particles continuously to the combustion chamber. The alumina particles (1 micron) are introduced into the combustor using the high pressure compressed air. Camera calibration also shows some challenges. The camera is calibrated considering the Origo marker (0,0) as the datum. Also, two pre-set markers A and B are used to generate the scale factor for calibration.

3.3.4 Solution Executed in PIV Post Analysis

There are many difficulties in the post-processing of raw PIV data. Non-uniformities is one of them. For this, Dynamic studio generates an image balance map. The image balance map is then applied to the raw images to generate light balanced maps. The light balanced images have higher contrast, therefore, the location of the particles is easily distinguished. Besides, there is a presence of higher background noises in the processed images. Dynamic studio helps to mask out the area of higher background noises. Also, to address wall bias, a wall windowing function is implemented to the processed images. The wall windowing function provides a symmetrical uniform distribution of the seeding particle within the interrogation area.

Furthermore, the velocity vector fields have the issue of adapting the interrogation area to the local seeding densities and flow gradients. To address this issue, an adaptive PIV function is implemented. The adaptive PIV is also used for frequency filtering and universal outliner detections.

3.4 System Upgradation for Supersonic Combustion

Three different Re's (15000,30000,64000) and seven different equivalence ratios (Φ) are tested and post-processed. Therefore, there is a total of 21 tests, seven tests at each Re. However, the present system is designed for sonic combustion. One of the goals of this project is to make the system ready for supersonic combustion. For this, tremendous efforts have been

made. The supersonic combustion system is under development. Design, analytical and simulation analysis has been performed to understand the thermodynamics of the flow. These results are used to optimize the design of the air heater and the De Laval nozzle. These results are also used to determine the optimal criteria needed to achieve Ma >2 at the combustor inlet. The proposed schematic of the supersonic combustion test setup is shown in Figure 27.
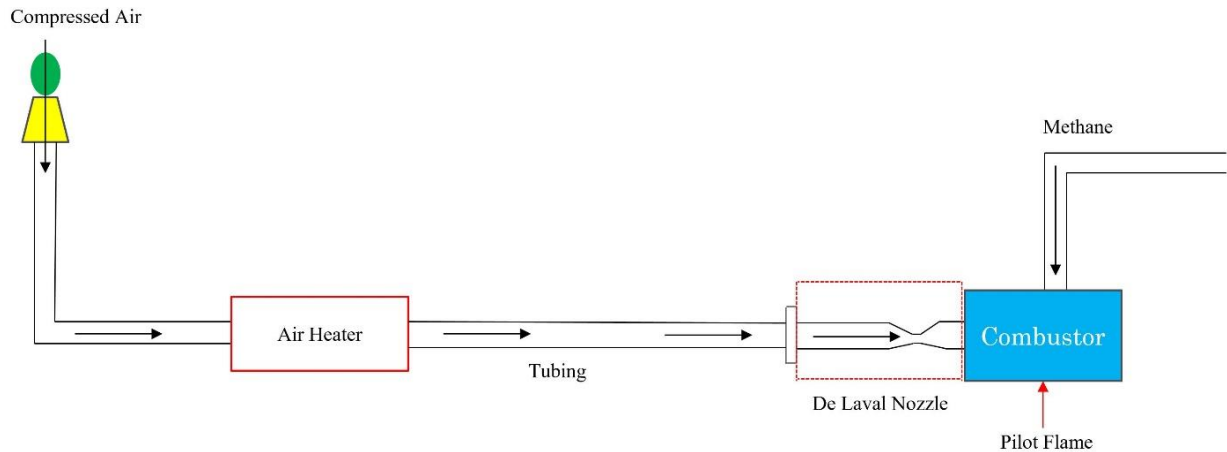
Figure 27. The schematic of the proposed supersonic combustion test facility

3.4.1 Selection of Air Heater

The premixed methane-air mixture is used subsonic combustion study. However, for supersonic combustion tests, the methane and air will introduce separately to the combustor body. For the airline, an air heater is designed so that an elevated temperature could be achieved. The purpose of the heater is to increases the thermal energy of the air. When heated air goes through the converging and diverging nozzle (supersonic diffuser and supersonic nozzle or De Laval Nozzle), the thermal energy converted to kinetic energy. Therefore, the nozzle exit-velocity increases. This helps to achieve Ma for supersonic combustion.

The air properties at Re =64000 (50CFM) are known from the test matrix. These properties are used as the inlet conditions to the air heater. An analytical calculation has been done to calculate the air properties at the heater outlet. The heater outlet air properties are

calculated in such a way that when air passes through the proposed De Laval Nozzle, it creates high exit velocity where Ma > 2. The steps considered to calculate the air properties at the heater outlet and long tubing are discussed below.

The following equations are used to determine the stagnation properties at the heater outlet:

$$T_{01} = T_1 + \frac{V_1^2}{2C_P} \tag{26}$$

$$T_{02} = T_2 + \frac{V_2^2}{2C_P} \tag{27}$$

$$Q = \dot{m}C_P \left(T_{02} - T_{01}\right) \tag{28}$$

Where T_{01} and T_{02} are the stagnation air temperatures at the heater inlet and outlet. Also, Q is the total heat input by the heater. Therefore, if one of these temperatures is known, others should be determined.

The calculated stagnation properties of air are used as the inlet conditions to the long tubing. The heat resistance method is used to calculate the total resistance inside the tubing. Equation 29 to 31 are used for the heat resistance method. At the inner and outer sides of the tubing, the heat is transferred through convection. There is also a conduction heat transfer through the tube solid wall.

$$Q_{Loss} = \frac{\Delta T}{R_T} \tag{29}$$

$$R_T = R_{Inner} + R_{Wall} + R_{Out} \tag{30}$$

$$= \frac{1}{h_1 A_1} + \frac{\ln(\frac{D_0}{D_i})}{2\pi K L} + \frac{1}{h_0 A_0} \tag{31}$$

To account the convection heat transfer coefficients (h_1 and h_0), Gnielinski Equation is used. The Gnielinski Equation gives the Nu values (expressed by Eqn. 32). The fundamental air properties tables and Nu values are used to get the h_1 and h_0.

$$Nu = \frac{\left(\frac{f}{8}\right)(Re-1000)P_r}{1+12.7\left(\frac{f}{8}\right)^{0.5}\left(Pr^{\frac{2}{3}}-1\right)} \tag{32}$$

The heat loss through the tubing is then calculated using the Eqn. 29. The temperature at the exit of the tube is determined using Eqn. 33.

$$Q = \dot{m}C_P\,\Delta T \tag{33}$$

The air properties at the heater outlet and tube outlet are listed in Table 8.

Table 8. Air properties at the outlet of heater and tubing

Heater Outlet	Tube Outlet
Ma = 0.12	Q_{Loss} = 800 W
T^* = 3460°K	T_2 = 667°K
P^* = 235 kPa	
V^* = 1077 m/s	
Ma_2 = 0.192	
T_0^* = 4140°K	
T_{02} = 676 °K	
Q =50 KW	
P_2 = 535 kPa	
V_2 = 92 m/s	
T_2 = 400°C = 673°K	

The air heater requirements match with locally available air heat torch 400 series. This heat torch 400 is purchased from TUTCO-FARNAM. The schematic of the air heater is shown in Figure 28.

Figure 28. Heat torch 400 used for supersonic combustion (Image is taken from

https://farnam-custom.com/)

Table 9. Airflow properties using heat torch 400 (properties are gathered from https://farnam-custom.com/)

Categories	Magnitudes and units
Power Input	16 KW
Maximum air inlet temperature	250°F = 121°C
Maximum air outlet temperature	900°F = 482°C
Minimum airflow rate	20 SCFM
Maximum airflow rate	220 SCFM
Air Pressure	120 PSIG

3.4.2 De Laval Nozzle

The airflow properties at the heater outlet are used as the inlet conditions to the De Laval Nozzle. A De Laval Nozzle is a combination of the supersonic diffuser and supersonic nozzle that is used to achieve higher Ma for high-speed combustion. An analytical and simulation-based analysis has been done to optimize the design of De Laval Nozzle.

The exit area of the nozzle should be matched with the existing windowed combustor. Therefore, the nozzle exit diameter is kept 25mm. The Ma =2 is considered at the nozzle exit and the back-calculation approach is implemented to calculate the throat and nozzle inlet dimensions.

3.4.2.1 Analytical Calculation

3.4.2.1.1 Dimensions and Air Properties at Nozzle Inlet

The air properties after heater are used as the inlet conditions to the De Laval Nozzle. Also, the nozzle inlet flow rates and Mach number are calculated based on the Re =64000 conditions. Once the flow passes the nozzle, it reaches the supersonic Mach. The following steps are followed to determine the nozzle inlet dimensions and air properties at the nozzle inlet:

$$P_1 = 100 \ Psi, \ \ T_1 = 400°C = 676°K, \ \ \ \ V_1 = 80 \frac{m}{s}$$

The inlet area of the nozzle is calculated using the Eqn. 34. The density and velocity of air at the nozzle inlet are calculated using the Eqn. 35 and 36.

$$A_1 = \frac{\pi}{4} (1.0'')^2 = 4.9 \times 10^{-4} \ m^2 \tag{34}$$

$$\rho_1 = \frac{P_1}{RT_1} \tag{35}$$

$$\dot{m} = \rho_1 A_1 V_1 = 0.13 \ kg/s \tag{36}$$

3.4.2.1.2 Dimensions and Air Properties at Nozzle Exit

The M_2 =2 is considered at the nozzle exit. After that, isentropic flow equations are used to determine the other properties at the nozzle exit. After that, throat dimensions are also calculated. The steps are listed below:

The Mach number, temperature, velocity, density and dimensions at the nozzle exit are determined using Eqn. 37 to 41.

$$\left(\frac{P_1}{P_2}\right)^{\frac{\gamma-1}{\gamma}} = 1 + \frac{\gamma-1}{\gamma} \ M_2{}^2 \tag{37}$$

$$\frac{T_1}{T_2} = 1 + \frac{\gamma-1}{\gamma} \ M_2{}^2 \tag{38}$$

$$M_2 = \frac{V_2}{\sqrt{kRT_2}} \tag{39}$$

$$\rho_2 = \frac{P_2}{RT_2} \tag{40}$$

$$\dot{m} = \rho_2 A_2 V_2 = 0.13 \text{ kg/s} \tag{41}$$

3.4.2.1.3 Dimensions and Air Properties at The Nozzle Throat

The maximum nozzle exit area (A_2) is determined from Eqn. 41. Using $M_2 = 2$ and the 1D isentropic compressible flow functions for an ideal gas (Table A-13, Page 961, [35]), the critical throat area (A^*) is determined by

$$\frac{A_2}{A^*} = 1.6875 \tag{42}$$

3.4.2.2 Computational Analysis

Ansys Fluent (fluid) analysis is carried out to validate the analytical results. Analytically derived data are used as the inlet conditions for simulation. Viscid flow ($k - \varepsilon$) and Inviscid flow assumptions are used for computational analysis. Mesh independence study is carried out for the proposed nozzle (shown in Figure 29). The element of 20,000 is found to be the optimized meshing condition for the nozzle. The meshing geometry of the nozzle is shown in Figure 30.
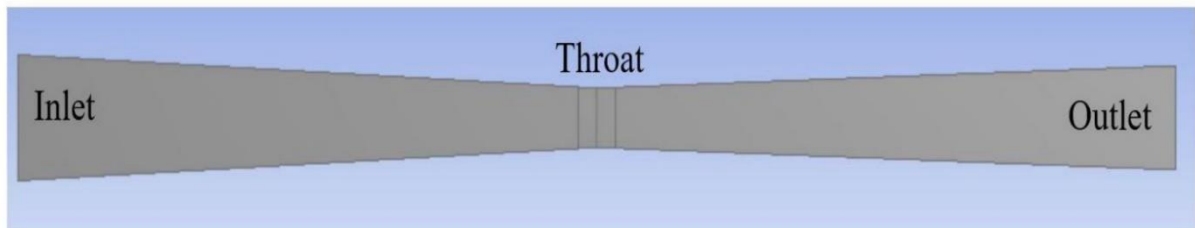
Figure 29. 2D view of the proposed De Laval Nozzle
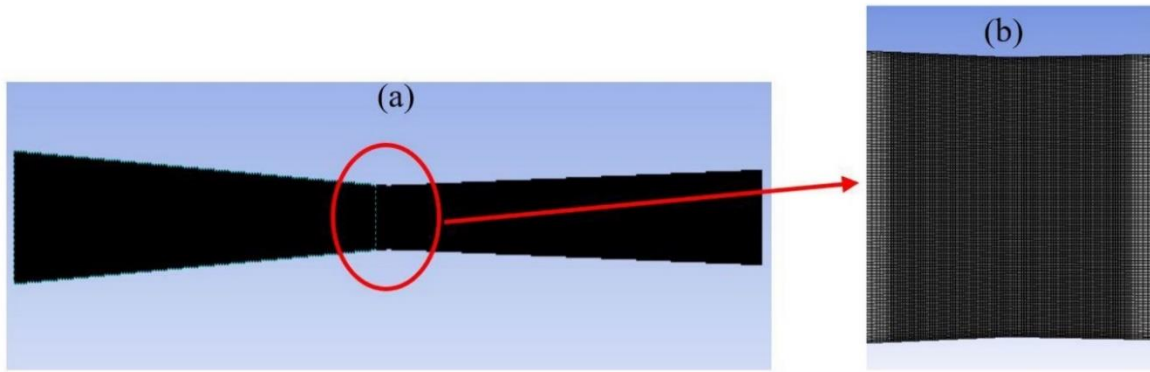
Figure 30. The meshing of the nozzle, (a) whole geometry and (b) Throat

Ansys FLUENT solver is used to solve the fluid flow inside the nozzle. Table 10 and 11 shows the solver parameters and boundary conditions used to analyze the flow inside the nozzle.

Table 10. Solver parameters used for flow analysis in Ansys FLUENT

Solver Parameters	Conditions and Assumptions
Solver	Steady, Density-based
Model	Energy-ON Both Viscid and Inviscid flow assumptions
Solution Material	Air with Ideal gas properties

Table 11. Ansys FLUENT boundary conditions used for solving the flow inside the nozzle

Flow Zones	Boundary Conditions
Inlet	Pressure Inlet with 110 Psig (700,000 Pa) and 673°K
Outlet	Pressure Outlet
Wall	SS Wall with regular material properties

3.4.2.2.1 Viscous k-ε Model

The viscous effect plays a role in flow propagation inside the nozzle. The k- ε model is used to address this issue. The k- ε derived nozzle Mach contour is shown in Figure 31. The nozzle exit Mach number is found to be 1.8. Therefore, the nozzle exit area needs to be increased. Sonic Mach is achieved at the throat which verifies the analytical results discussed

before. The Mach decreases at the near-wall regime because of the steep change in viscous drag.
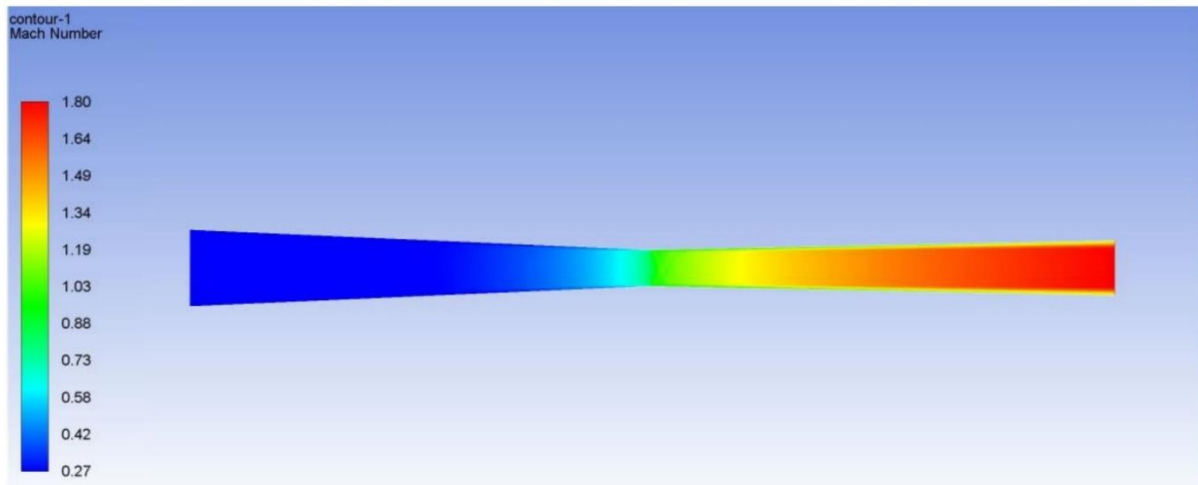
Figure 31. Mach contour using the viscous k-ε model

Static and dynamic pressure (shown in Figures 32 and 33) is calculated to see if there is any backflow and flow separation/shock waves respectively at the nozzle exit. The maximum static pressure of 38877 Pa (6 Psig) is observed at the nozzle outlet which indicates that there is no backflow in the system.
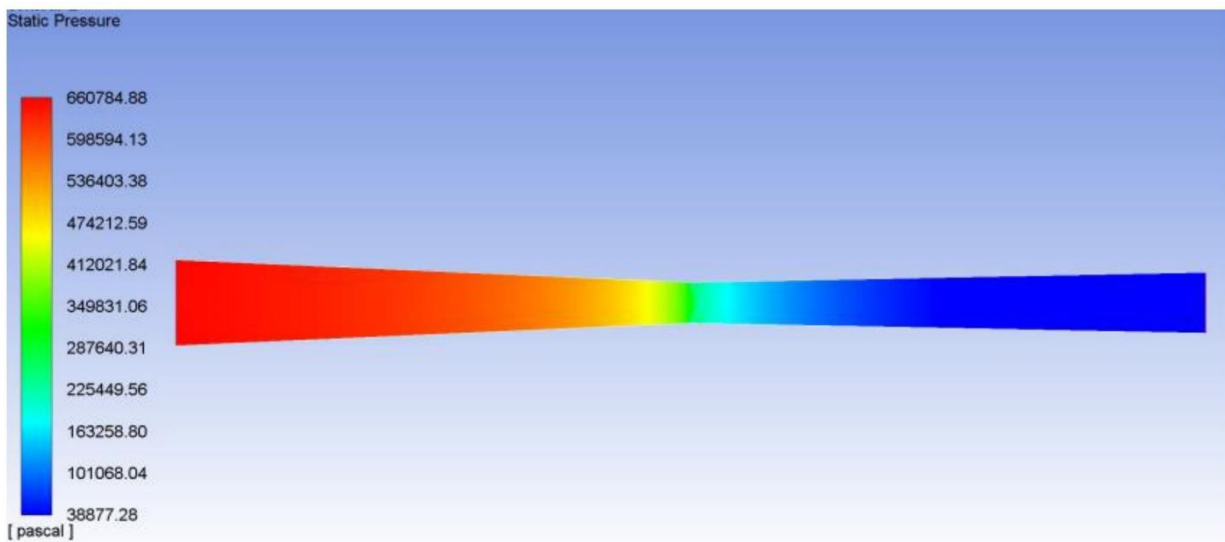
Figure 32. Static pressure contour using the k-ε model
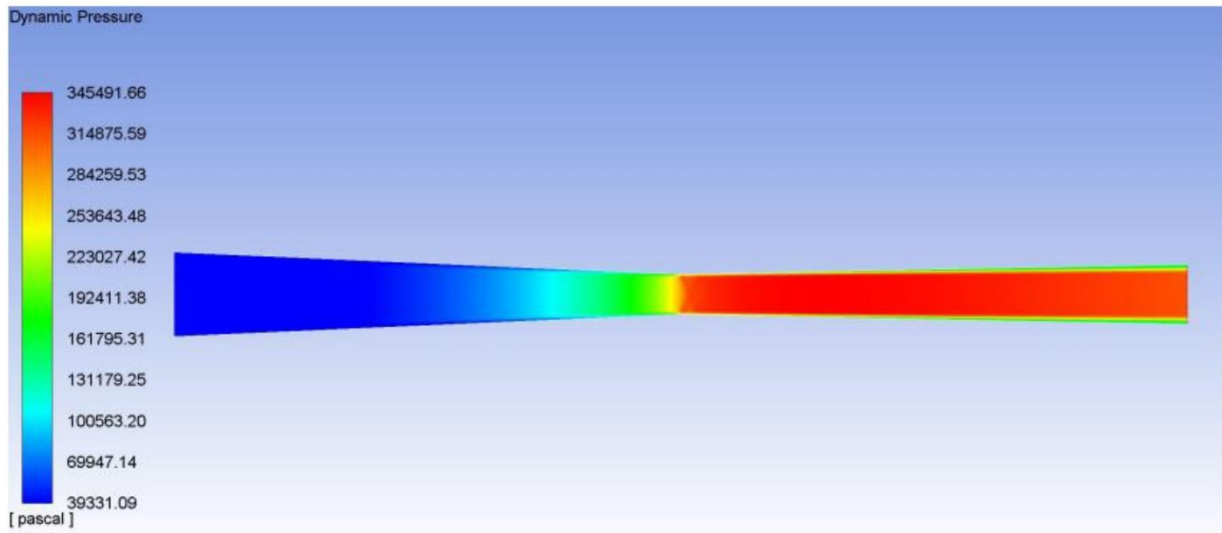
Figure 33. Dynamic pressure contour using the k-ε model

Dynamic pressure indicates the rise of moving fluid's pressure over its static pressure because of the motion. The maximum dynamic pressure of 345492 Pa (3.45 bar or 50 Psig) is observed at the nozzle outlet (see Figure 33). This dynamic pressure yields higher kinetic energy at the nozzle exit. The higher kinetic energy corresponds to higher Mach number at the nozzle outlet.
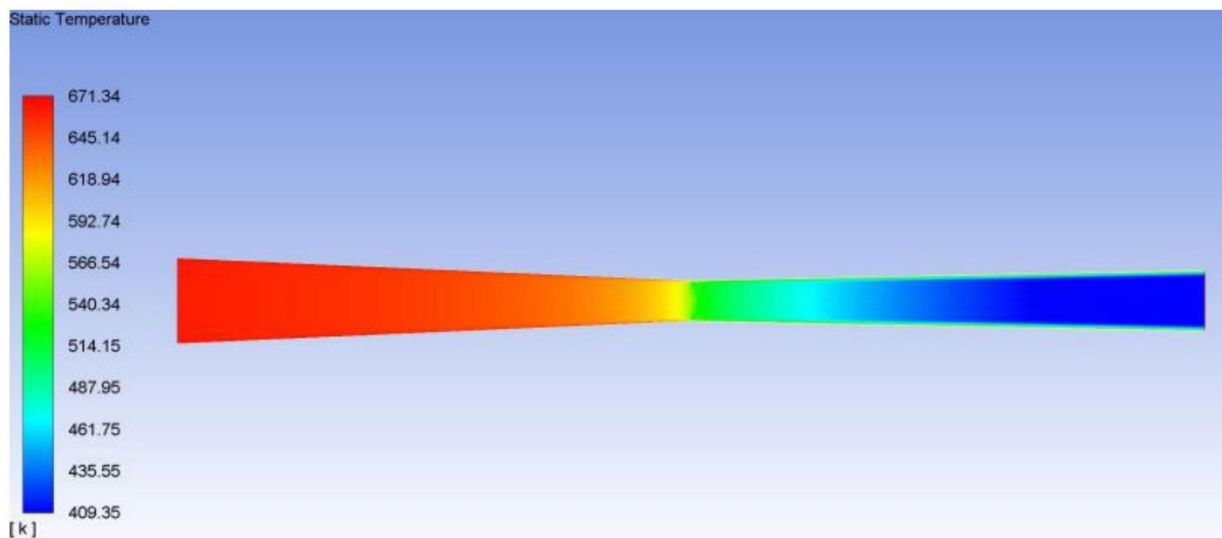
Figure 34. Static Temperature contour using the k-ε model

The temperature is generated to verify the phase change of the air. Figure 34 represents the temperature contour of the heated air. It is observed that the air temperature at the nozzle

exit is 410ºK (137ºC). This value is 37ºC higher than the analytical value. Therefore, there is no phase change in the air.

3.4.2.2.2 Inviscid Model

As the temperature increases, the effect of viscous forces decreases. The viscous forces are less dominant compared to the momentum diffusion at elevated temperatures. Thus, the inviscid model is implemented. A small change in Mach number at the nozzle exit ($Ma_2 = 1.86$) is observed. It happens because the expansion of the air at the nozzle outlet is not enough. The exit diameter of the nozzle is then increased to 20 mm. Now the Mach number at the nozzle exit increases to 2.04, which satisfies the requirements of the ongoing research (shown in Figure 36).
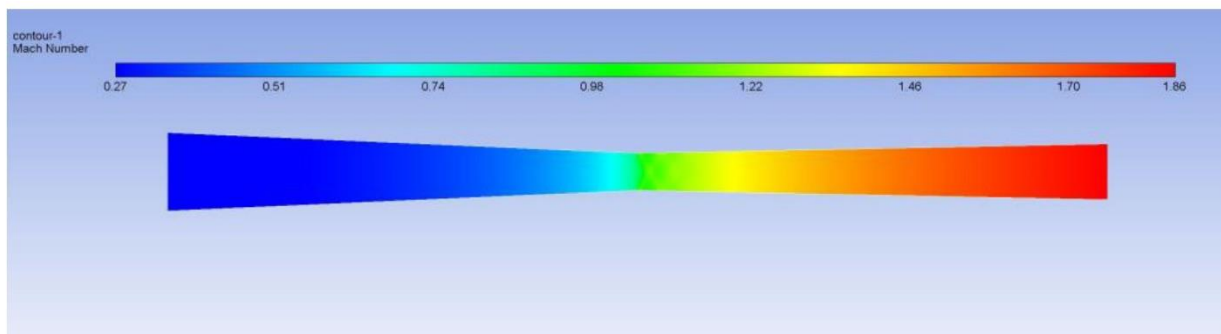
Figure 35. Mach number contour using the inviscid model with under expanded mode
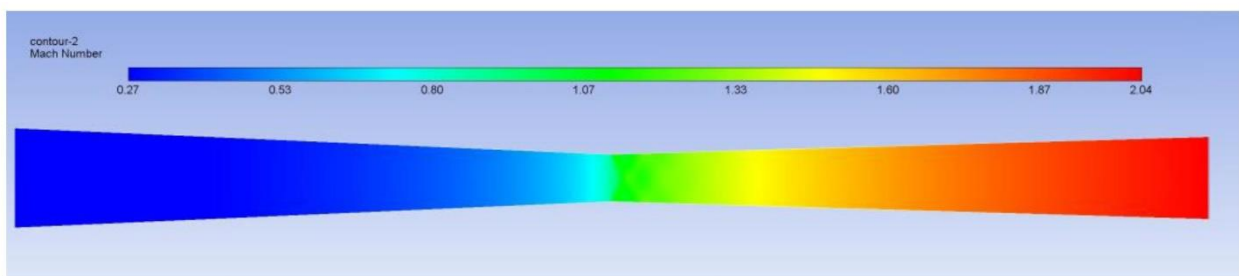
Figure 36. Mach number contour when nozzle exit diameter increases to 20 mm (Optimized expansion mode)

It is found that the inviscid flow assumptions resemble the actual trend of the flow physics inside the nozzle. Therefore, the results with the inviscid flow assumption are

considered for the optimization of the nozzle design. The optimized parameters and flow

properties are listed in Table 12.

Table 12. The optimized parameters of the proposed De Laval Nozzle

Nozzle Inlet	Throat	Nozzle Outlet
$T_1 = 400°C$ $P_1 = 100\ Psi$ $M_1 = 0.12$ $D_1 = 25\ mm$ $A_1 = 4.9 \times 10^{-4}\ m^2$	$A^* = 1.26 \times 10^{-4}\ m^2$ $D^* = 12.64\ mm$	$P_2 = 19\ Psi$ $T_2 = 100°C$ $D_2 = 20\ mm$ $A_1 = 3.14 \times 10^{-4}\ m^2$

The optimized dimensions are used to design the supersonic De Laval Nozzle. The

CAD view and a sectional view of the nozzle are shown in Figure 37.

(a)   (b)
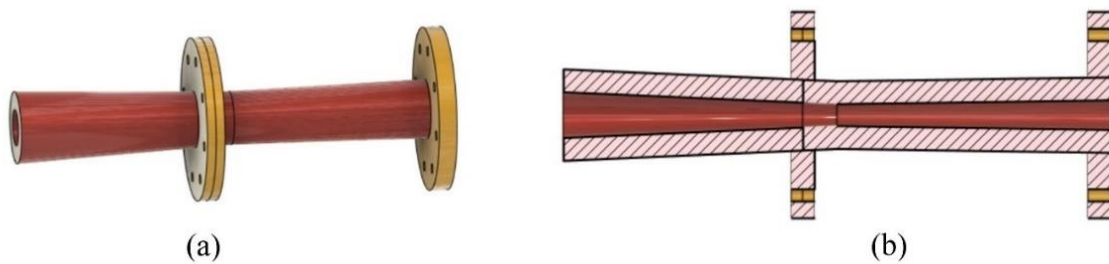
Figure 37. Supersonic De Laval Nozzle, (a) 3D view, (b) Cross-sectional view

The De Laval Nozzle is attached to the combustor such a way that there is no leakage

and backflow to the system. Also, it ensures that the reactants are not affected by external

influence. The assembly view of De Laval Nozzle and combustor assembly is shown in Figure

38.
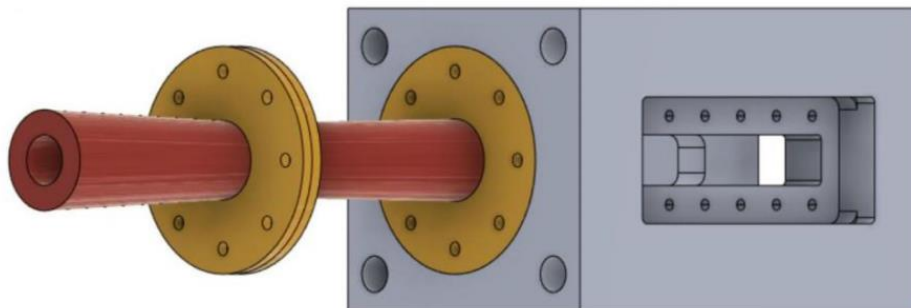
Figure 38. De Laval Nozzle and Combustor Assembly

3.5 Combustion Modelling

The PIV results and laminar flame characteristics are used to investigate the turbulent flame dynamics. These results are also used to detect the flame regime, the limit of flame regime boundaries and scale-factors that affects the reaction zone characteristics. To validate that the flame behavior and flame regime, a separate Ansys FLUENT based premixed combustion modeling (PCM) is performed. PCM is performed at all flow conditions and $\Phi = 1$. PCM gives the information on velocity, pressure and temperature characteristics, turbulence characteristics and combustion characteristics. For the validation of the flame regime location, only the Damkohler number (Da) obtained from PIV and PCM will be compared. Besides, the author extends the effort to check the turbulent flame speed at all flow conditions. The target is to validate the flame speed behavior observed from flame profiles/edges. The following equations are the default equations used in PCM to calculate the turbulent flame speed, S_T:

$$S_t = Au' \left(\frac{\tau_t}{\tau_c}\right)^{\frac{1}{4}} \tag{43}$$

$$\tau_t = \frac{L_T}{u'} \tag{44}$$

$$\tau_c = \frac{\alpha}{S_L^2} \tag{45}$$

Where A is the model constant. A $= 0.52$ is generally used for premixed combustion modeling. τ_t is the turbulent time-scale which depends on the turbulent integral length-scale (L_T) and velocity fluctuations (u'). τ_c is the chemical time-scale which is controlled by the thermal diffusivity of the reactants (α) and laminar flame speed (S_L). The thermal diffusivity of the reactants depends on the mole fractions and thermal diffusivity of the mixture components. The detail of the combustion model and results validation will be discussed in chapter 4.

Chapter 4: Results and Discussions

As mentioned earlier, the goal of the ongoing research is to design and develop the next-generation high-speed engine combustor. Therefore, the understanding of flame-flow interaction at extreme turbulence conditions is very important. For this, the PIV and PLIF results are discussed in this chapter. The effect of different flow mixture rates (12 CFM, 25CFM and 50 CFM), turbulence conditions (Re =15000, 30000 and 64000) and equivalence ratios ($\Phi = 0.6$ to 1.2) on the flame and flow characteristics will be discussed. Also, grids with different geometries and blockage ratios (shown in Table 3) will be examined for the flame-flow study.

The turbulent characteristics such as velocity vector fields, turbulent intensity fields, and vorticity fields will be discussed. Besides, flame evolution, flame regime detection, flame regime characteristics, and the scale factors that control the reaction zone characteristics will be examined. A correlation will be developed between the flow and flame parameters. The PIV derived Da will be validated with the premixed combustion model (PCM). A modification of the existing system for future supersonic combustion tests will be discussed. Experimental methodologies, combustion modeling strategies, and post data/image processing schemes for supersonic combustion will be proposed in this chapter. In the section below, the flow characteristics and flame dynamics will be discussed sequentially.

4.1 Turbulent Characterization

PIV laser system and synchronization have already been discussed in chapters 2 and 3. The PIV tests presented in this research were done by former cSETR student Martin Alejandro De La Torre [41]. However, PIV data is further analyzed for global flame regime detection. Permission is taken from Martin Alejandro De La Torre [41] to further analyze the PIV results. Another reason to analyze the PIV data is to check the presence of systematic errors in the

54

turbulence properties. Thus, in the following section, the PIV post-processing techniques and PIV results will be introduced sequentially.

4.1.1 PIV Post-processing Techniques

Image balancing is used to minimize the effects of laser light non-uniformities in the processed images. Based on the set of raw images, Dantec Dynamic studio generates an image balance map. Later, the image balance map is applied to the raw images to generate light balanced maps. The light balanced images have higher resolution thus the locations of the particles are clear. Another tool called image masking is also used to blackout the unwanted areas and highlight the target area. Dynamic studio mask out the areas (walls, and strong light reflection zones, etc) that generate higher background noises. Besides, Adaptive PIV is used to adapt the interrogation area to the local seeding densities and flow gradients. This method is useful to resolve the velocity vector fields generated in the shear layer. Adaptive PIV also has options to apply the frequency filter, window functions, and universal outliners detections.

An adaptive PIV post-processing tool called "wall windowing" is also used to reduce the spurious vectors present in the processed images. Wall windowing minimizes the wall bias. There are some instances when the interrogation area extends past a wall. This results in a deviation of distance and velocity measurements of the particles. It happens because particles passed the wall have higher acceleration than the particles near the wall. Wall windowing overcomes these difficulties. It gives a symmetrical uniform distribution of seeding particles in the interrogation area.

The outliers are early detected and ignored using the peak validation tool. The peak validation is further supported by the universal outlier detection algorithm. This algorithm compares each vector being generated to its neighbors. The adaptive PIV tool is used to resolve the velocity gradient formed at the onset of the backward-facing step. This gives an instantaneous velocity vector field map.

A Vector statistical tool is used to derive other turbulence parameters. For instance, the scalar map tool is used to generate the turbulent intensity scalar map and vorticity map. PIV also uses a default post-processing tool called proper orthogonal decomposition to resolve the flow system. It is used to identify the dominant components in the flow. It is also used to get the dimensional description of the multidimensional flow systems (2D or 3D).

To get the instantaneous velocity components $u(t)$, u_{RMS} and v_{RMS}, an interrogation plane is placed on the edge of the backward-facing step. The data acquired at the interrogation line is used to study the local velocity, turbulent intensity, and vorticity. The detail of the PIV post-processing techniques could be found elsewhere [41].

4.1.2 PIV Induced Turbulence Flow Characteristics

Grid induces the initial acceleration to the flow. The flow is further accelerated once it passes the backward-facing step as evident in Figure 39. The velocity vector field map shows the presence of low-velocity recirculation zones at the shear layer. This low-velocity recirculation zone helps to anchor the flame. The flame under grid 1(at 12 CFM and 50 CFM), and grid 3 (at 25 CFM and 50 CFM) shows the presence of some low-velocity vectors surrounded by high-velocity vectors on the upper part of the flow field. It happens because of the higher local flow fluctuation. The eddies are higher at 50CFM compared to the other two flow rates. The higher flow momentum and turbulence are responsible for this behavior. The flow under grid 3 and 4 show more eddies in the recirculation zone than it is under grid 1 and 2. The higher blockage ratios of grid 3 and 4 change the fluid-scales in the recirculation zone. Therefore, the flow forms many small-scale structures (small eddies) in this area.
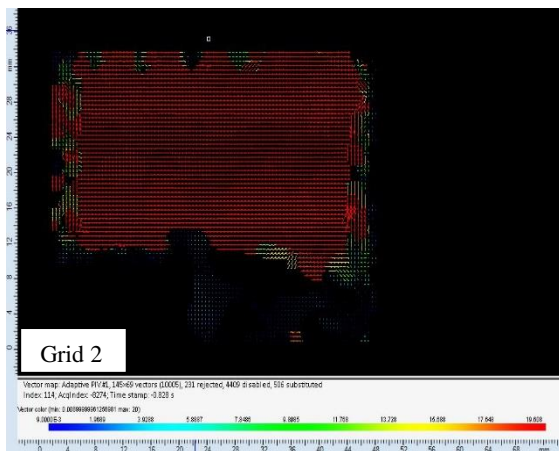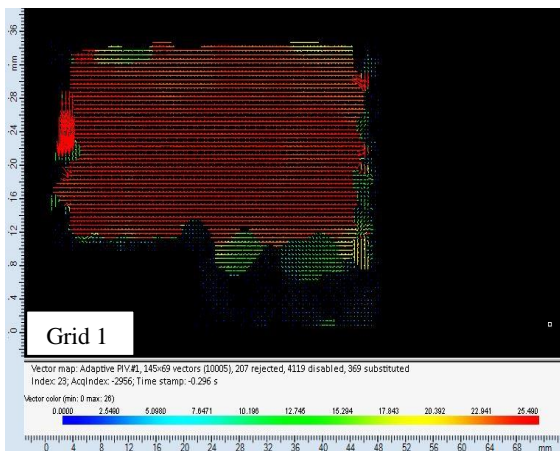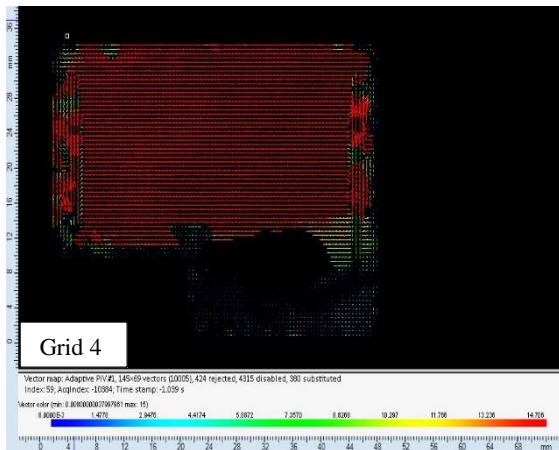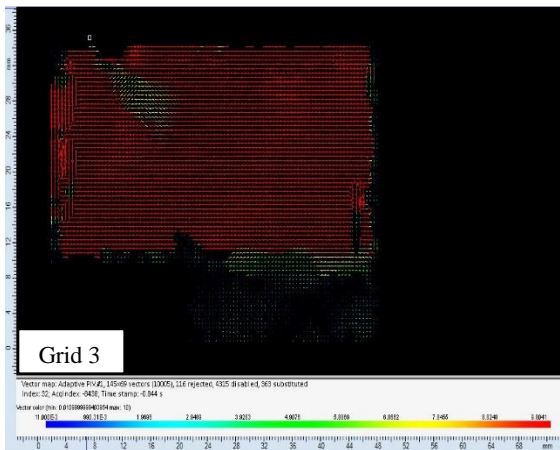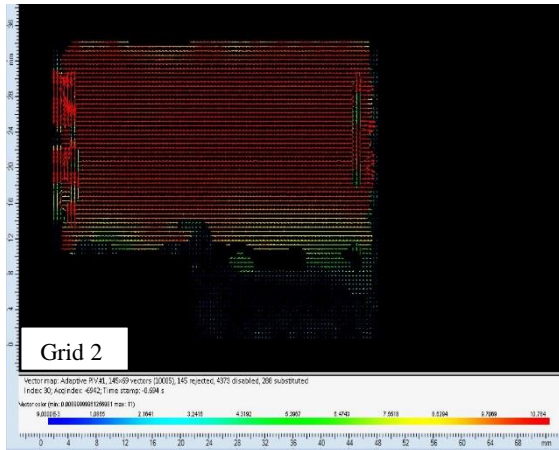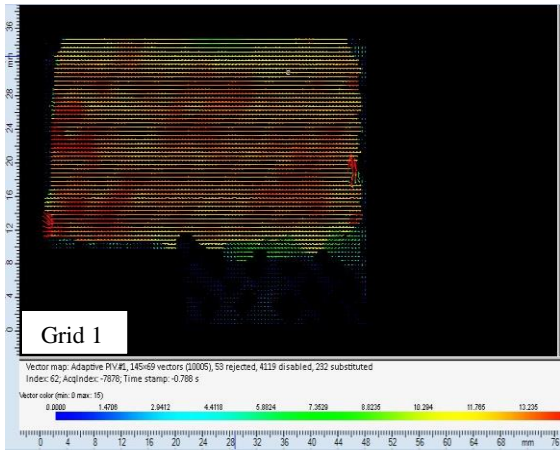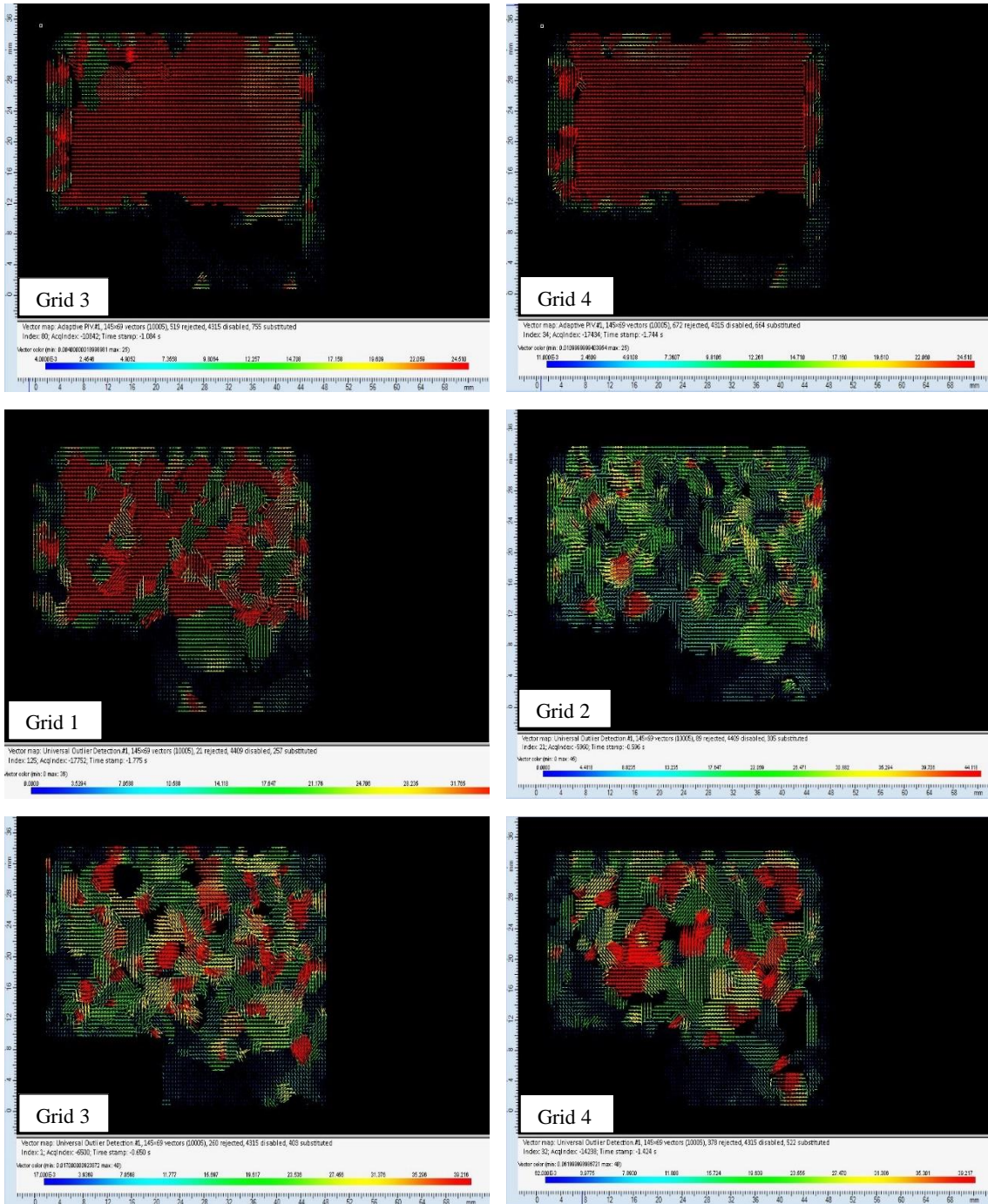
Figure 39. The velocity vector field maps at Re = 15000 (12 CFM) (first two rows), Re =30000 (25 CFM) (3rd and 4th two rows) and Re = 64000 (last two rows) (Zoom-in for better visualization) [41]

Post grid theoretical flow and the measured flow acceleration are used to calculate the velocity at different flow conditions. Velocity components extracted at the interrogation line are presented in Figure 40. The maximum velocity of 17 m/s, 27 m/s and 33 m/s are calculated at 12CFM, 25CFM and 50CFM respectively. The maximum flow acceleration/deceleration of

7 m/s is observed. The fluctuating parts of the velocity components are evaluated using equation (7). The velocity fluctuations of 0.5 and 0.25 m/s are observed for u and v components at 12 CFM and 25 CFM respectively. At 50 CFM, the velocity fluctuation of 20 m/s and 10 m/s are observed for u and v components respectively. It is observed that the v velocity component dominants over u velocity component at 50 CFM. The higher tangential (radial) velocity fluctuation is responsible for this behavior. The fluctuation is controlled by the perforated plate installed at the inlet of the combustor. The details about the velocity fluctuations could be found elsewhere [41].
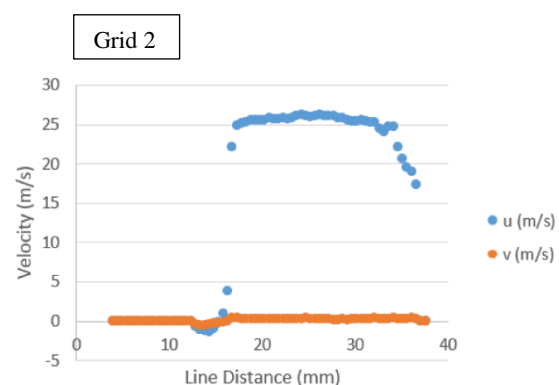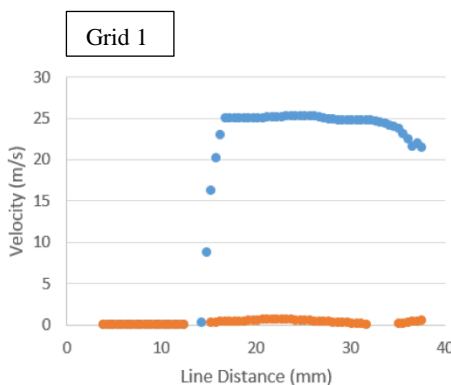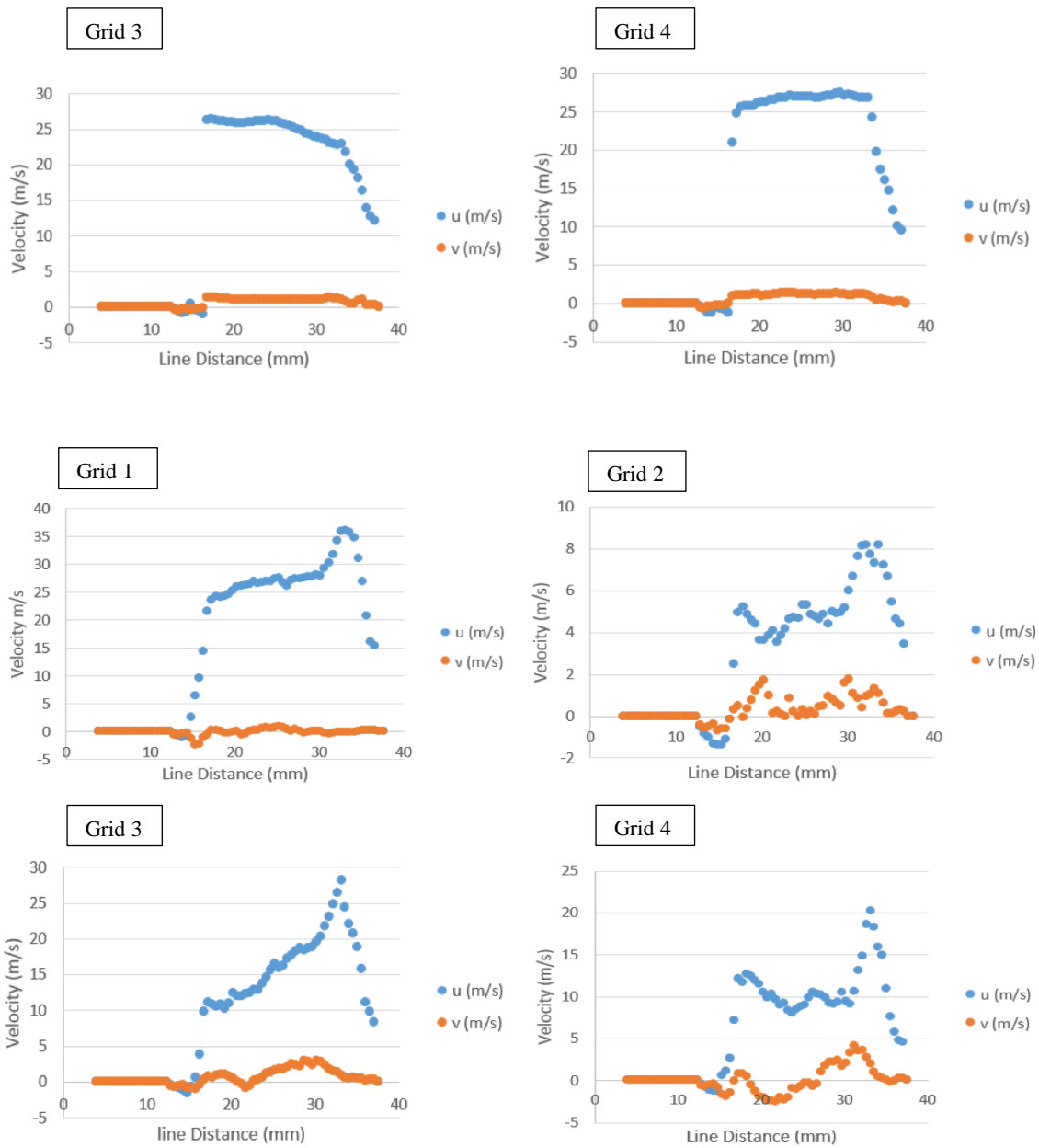
Figure 40. Average velocity acquired at the interrogation line for Re = 15000 (12CFM) (first two rows), Re = 30000 (25 CFM) (3rd and 4th rows), and Re =64000 (last two rows) [41]

To understand better flow behavior, turbulence intensities (I) are calculated using the equation (8). The dynamic studio is also used to generate the turbulent intensity contour plot which is shown in Figure 41.

60
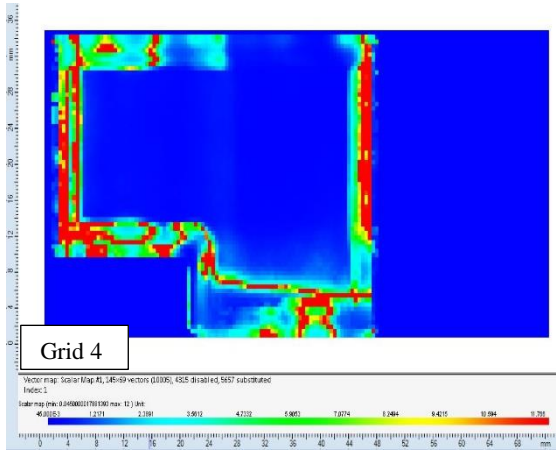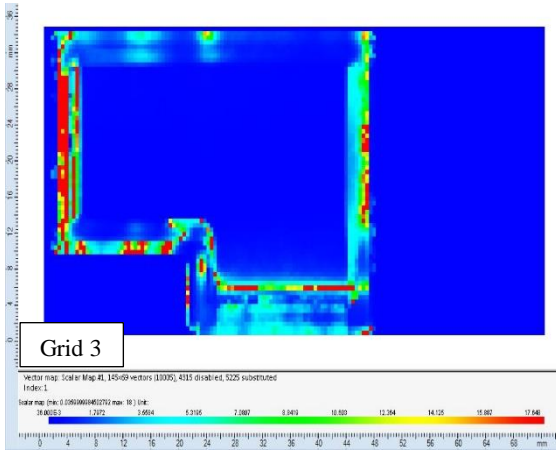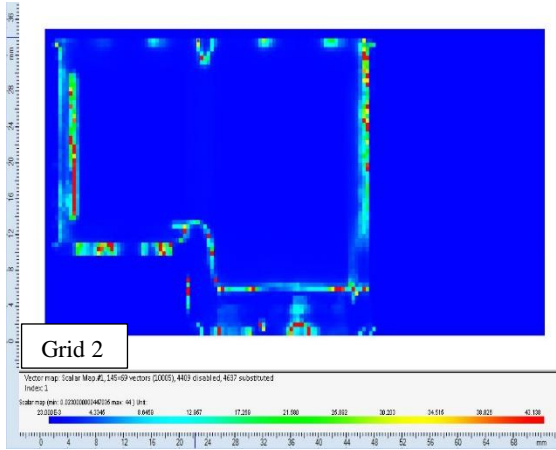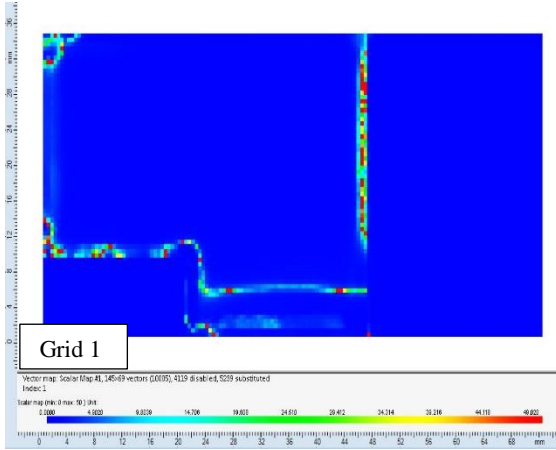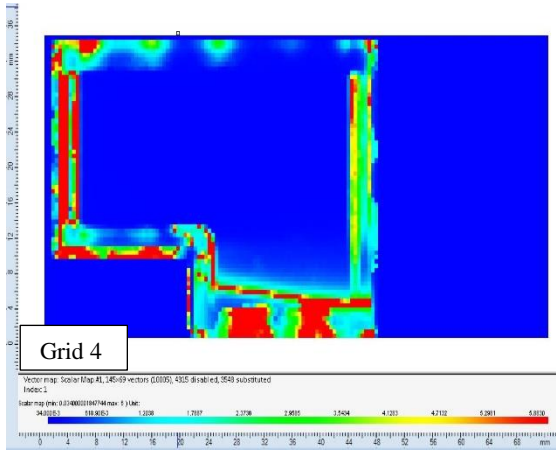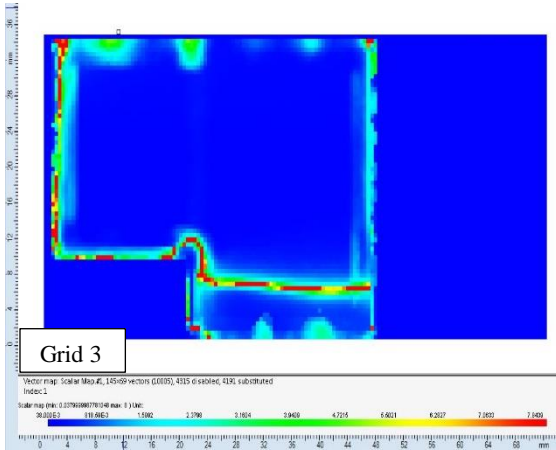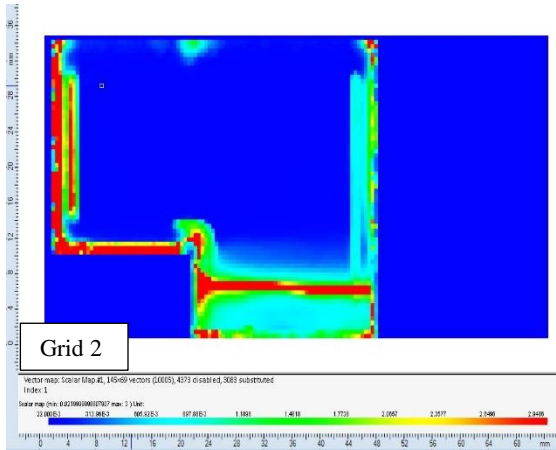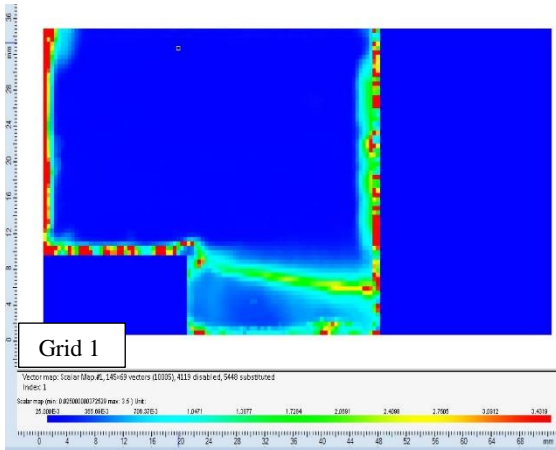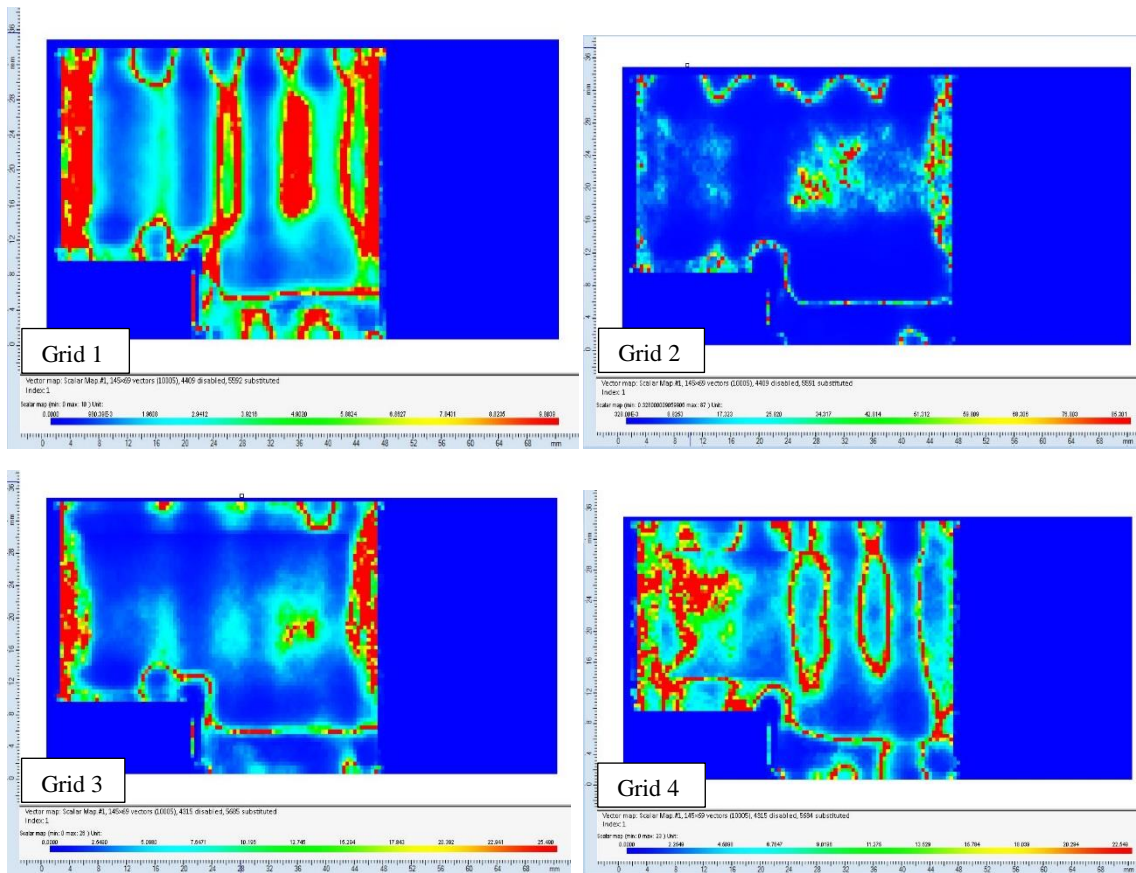
Figure 41.The turbulent Intensity contour maps at Re = 15000 (12 CFM) (first two rows), Re =30000 (25 CFM) (3rd and 4th two rows) and Re = 64000 (last two rows) (Zoom-in for better visualization) [41]

The turbulent intensity contour map shows how the recirculation zone behaves. It also shows how the turbulence is distributed in the fluid domain. The grid 1, 2 have diffused turbulence at the recirculation zones, whereas concentrated turbulence is noticed under grid 3 and 4 (see Figure 41). This could be explained by the nature of the flow path allowance. Less restriction in the flow path induces diffuse turbulence, whereas, higher flow restriction is responsible for concentrated turbulence in the recirculation zone. The turbulent intensities are higher under grid 2 and 4, whereas it is lower under grid 1 and 3. The large hole diameters grids enhance the u' thus the turbulent intensity. The turbulent intensities at 50 CFM are 1.5 times to 2 times higher compared to 25 CFM. The higher blockage ratios and flow momentum at 50 CFM controls this behavior. Similarly, the turbulent intensities are higher at 25CFM compared to 12 CFM.

Figure 41 shows that turbulence is higher in the recirculation zone. It also gives the idea of how the flow fluctuation varies in the flow domain. The small eddies in the shear layer control the flow fluctuation at the lower part of the flow. On the other hand, the overall flow fluctuation is controlled by the grids and flow momentum.

The flow vorticities are calculated using the equation (9) and (10). Dynamic studio generated vorticity contours are presented in Figure 42. The formation of flow vortices and eddies is higher under grid 1 and 3. The small hole diameter induces many small-scale vortices and eddies in the flow. Besides, the velocity gradients are steep along the flow path. The gradient of the axial velocity component drops and perpendicular (radial or tangential) component increases. Thus, the rotation of the velocity vector increased. Consequently, flow vorticity increases under grids 1 and 3. On the other hand, the vorticity formation is less under grid 2 and 4. The higher hole diameter grids cause a less formation of vortices in the flow. The vorticity scale is higher at 50 CFM (Re =64000) compared to 25CFM (Re =30000) and 12CFM (Re =15000). The higher flow momentum and rotation of the velocity components at 50CFM are responsible for this behavior.
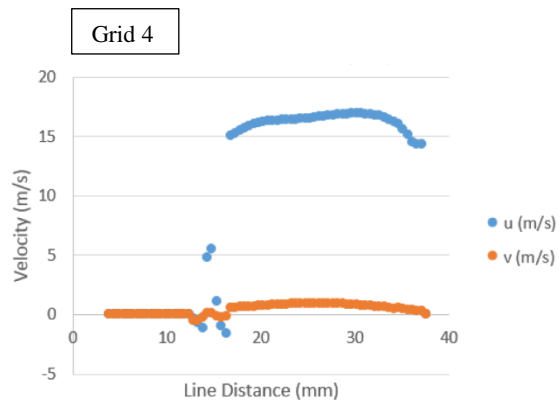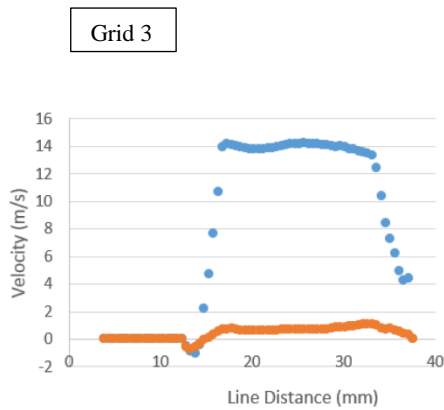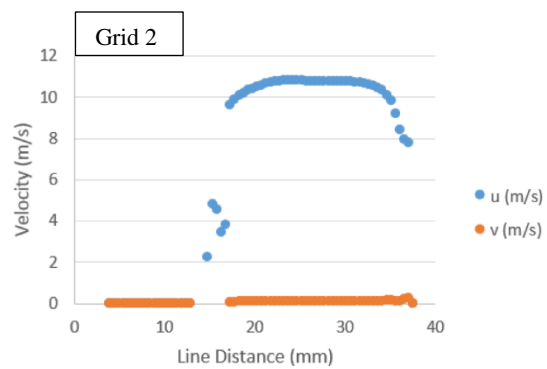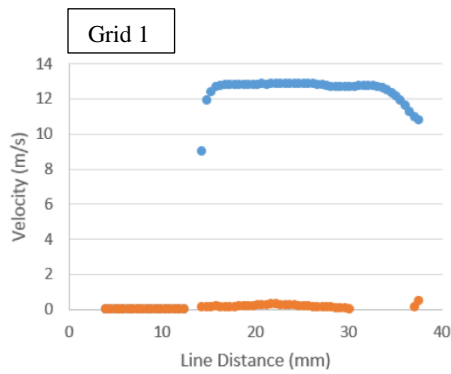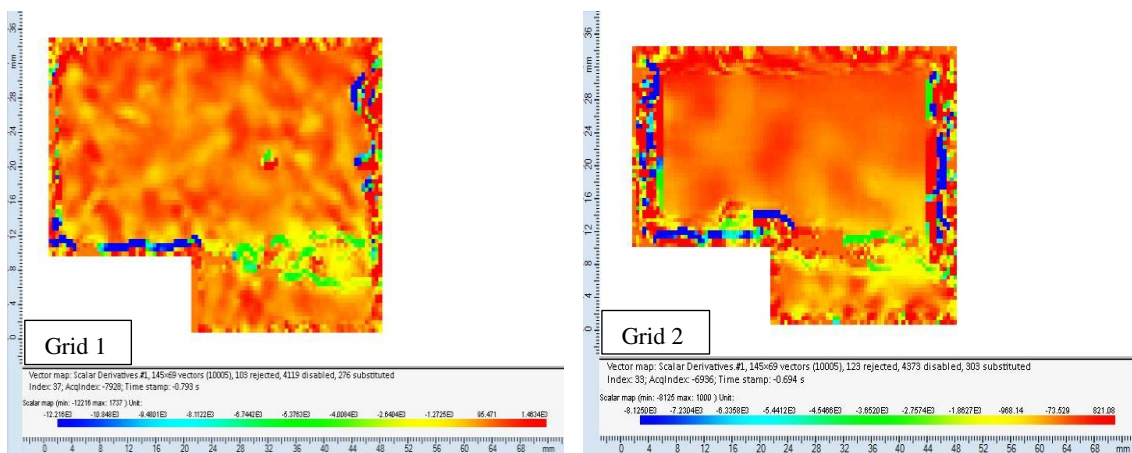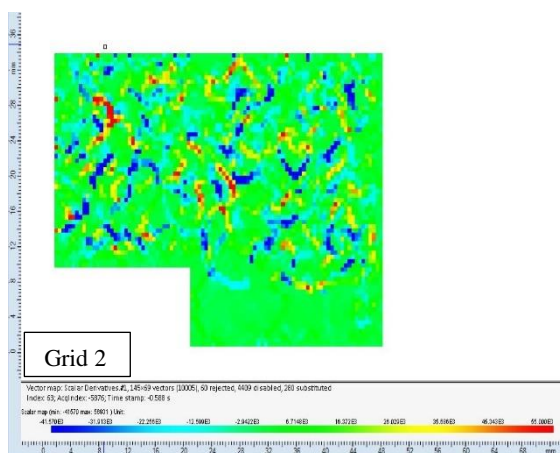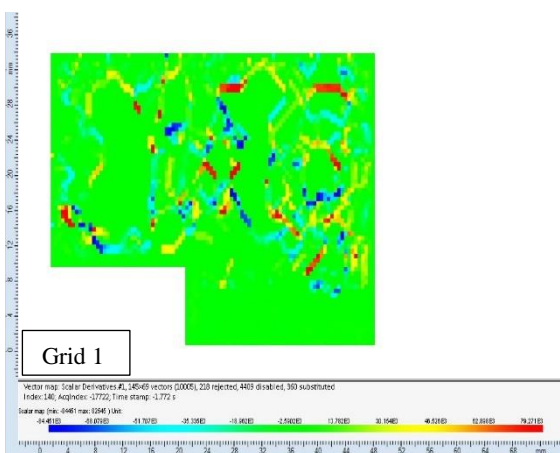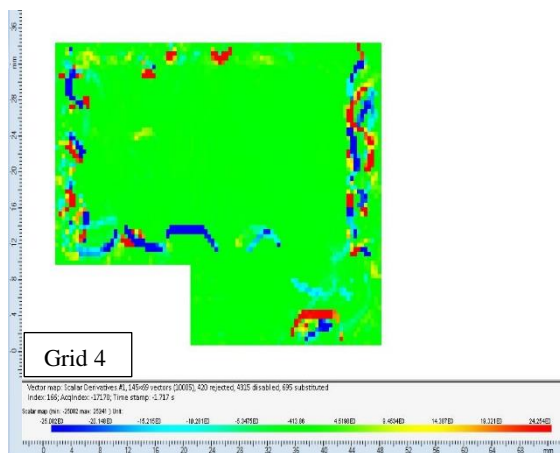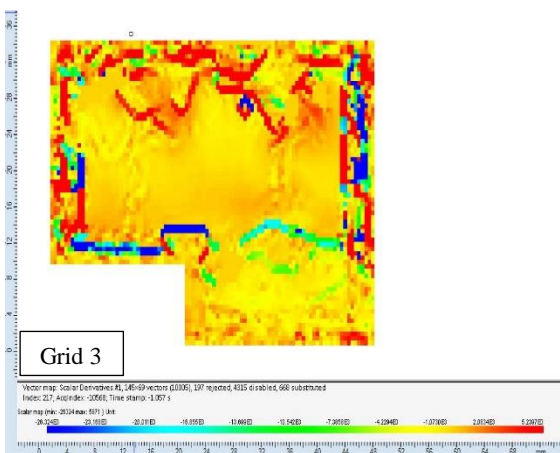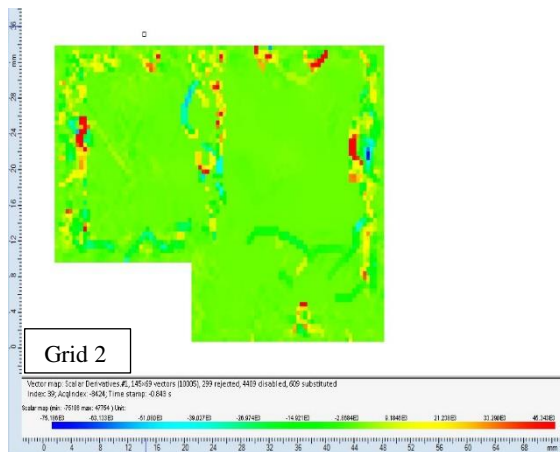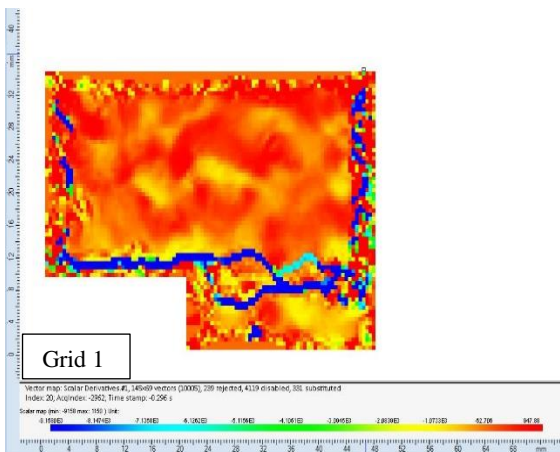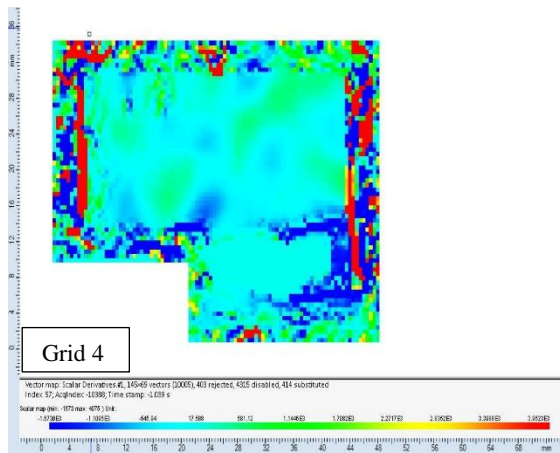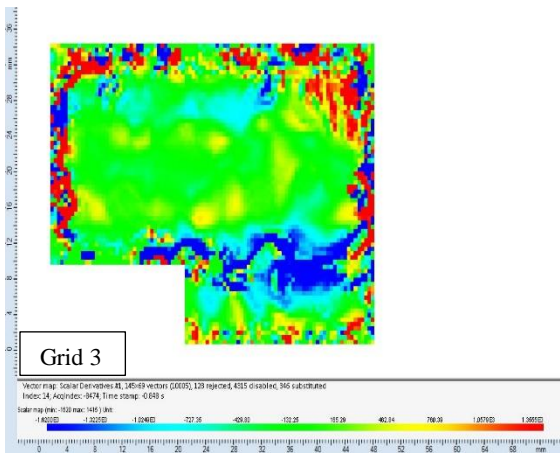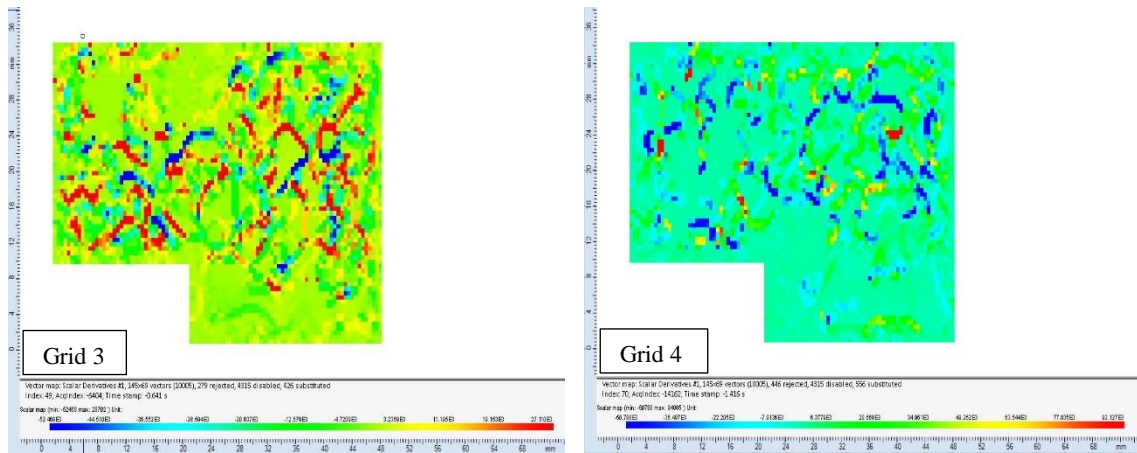
Figure 42. The vorticity contour maps at Re = 15000 (12 CFM) (first two rows), Re =30000 (25 CFM) (3rd and 4th two rows) and Re = 64000 (last two rows) (Zoom-in for better visualization) [41]

The vorticity contour map shows how the flow detached from the onset of the step. The detachment causes a formation of more low-speed recirculation zones in the downstream. The vorticity contour map could resolve both the small-scale and large-scale vortex pairs present at the shear layers. It is seen that the shear layers have the highest velocity gradient at all flow conditions. Therefore, the highest vorticity is seen in the recirculation zones. For other zones in the fluid domain, the vorticity is low.

The grid 1 and 3 shows many low-speed vortex pairs at the shear layer. Thus, vorticity is higher in the shear layer. On the other hand, the vorticity formation is less under grid 2 and 4. It is observed that the vortices are more concentrated and suppressed in the recirculation zone under grid 2 and 4. The higher blockage ratios (BR) and flow fluctuations (u') suppresses the turbulence at the recirculation zone.

At Re =64000 and 30000, the flow momentum is high. Therefore, the flow has a straight vortex line. It is represented by blue lines in Figure 42. On the other hand, at Re =15000, the vortex pairs seem to be the spotted dots. It is observed that both the grid geometries and flow momentum control the flow characteristics.

65

4.2 Flame Characterization Using the C-X CH-PLIF

The flow field characteristics alone do not provide enough information on high-speed combustion. For this, a flame study has been conducted using the 10-kHz rate laser-induced fluorescence (PLIF). Flow rates of 12 CFM (Re =15000), 25 CFM (Re =30000), 50 CFM (Re =64000) and $\phi = 0.6$ to 1.2 are considered for flame dynamics study. Dantec Dynamic studio tool is used to acquire the raw flame data and MATLAB codes are used to post-process the flame images. Although tests have been done for different lean-to-rich conditions, for the simplicity of the discussion, results at $\phi = 0.8$, 1.0 and 1.2 are reported in this section. The flame profiles at other ϕ conditions should be found in cSETR remote access resources such as in SVN. Readers are requested to contact the cSETR, UTEP for more inquiries.

Figure 43. Flame profiles at $\phi = 0.8$ and Re = 15000 (12 CFM) (Fold the laptop screen for better visualization), HSV colormap array contains red, green, blue intensities with the range [0, 1]

Figure 44. Flame profiles at ϕ = 1.0 and Re = 15000 (12 CFM) (Fold the laptop screen for better visualization), HSV colormap array contains red, green, blue intensities with the range [0, 1]

Figure 45. Flame profiles at ϕ = 1.2 and Re = 15000 (12 CFM) (Fold the laptop screen for better visualization), HSV colormap array contains red, green, blue intensities with the range [0, 1]

Figure 43-45 shows the flame profiles observed for all grids at ϕ = 0.8, 1.0, 1.2 and Re = 15000. At Re =15000 (12 CFM), the fuel-air mixture velocity was kept at 10 m/s. The notation (a) to (e) gives the pathway of how the flame grows inside the combustor. The notation "a" gives the flame profile at an earlier stage of combustion, "b" shows the initiation of the irregular shaped wrinkle in the flame, "c" gives the formation of more wrinkles at the flame

fronts, "d" shows the breakdown of the flame lets, and "e" shows the burnout of the flame lets from the flame core.

The presence of unburned gases inside the flame core is observed in Figure 43-45 (a). It happens because the combustion is not complete yet. The flame continues to grow until the unburnt mixture burns completely. There is a presence of different levels of turbulence in the flame. The flow momentum and grids produce a different level of turbulence in the flame. The flow is further accelerated once it passes the backward-facing step. The purpose of using the backward-facing step is to create low-speed vortices at the recirculation zones. The low-speed recirculation zones help burned gases to mix with the fresh mixtures. Thus, the flame gets stabilized.

In addition to that, the presence of irregularly shaped wrinkles was noticed in the flame profiles (shown in Figure 43-45 (b)). The wrinkle continues to form as the flame progress downstream (shown in Figure 43-45 (c)). The higher flow fluctuation, thermal instabilities generated by buoyancy and expansion causes the flame wrinkling. It also happens because of the change in local viscosity across the flame front. In other words, the compressive forces generated by the turbulent and velocity scales accelerate the flame-flame interactions. Thus, the reactant-product pocket formation rate increases. This increases the finger-shaped wrinkles in flame structure. As long as the effect of turbulence and combustion induced instabilities persists, the formation and growth of wrinkles continue.

After the flame wrinkling, the next event takes place in the flame is pinch-off. The breakdown of flamelet from the flame core is called the pinch-off event (shown in Figure 43-45 (d)). The large-scale fluid-structure present in the flow merges to the reaction zone. Therefore, the reaction zone is shattered. Also, the local velocity fluctuations, higher turbulent intensities, and local thermal diffusion accelerate the breakdown events in the flame. Near the

bottom wall at distance downstream, the breakdown event accelerates. This acceleration happens because of the infusion of some small eddies to the lower part of the flame core. This infusion changes the local flame fluctuation. Therefore, the breakdown of flamelet is dominant at the bottom wall zone. The loosed or semi-detached burned gases are small-scale in nature. Consequently, when they reach a very high temperature, they burn and disappear. This event is called a burned-out event (shown by "e" in Figure 43-45).

It is clear from Figure 43-45 that flame width increases as it moves downstream. The increase in flame width sometimes refers to flame broadening. The turbulent eddies enhance heat and mass transfer to the reaction zone. Thus, there is a change in local flame diffusivity. This causes a massive change in flame core structures. Therefore, the flame gets broadened towards downstream. More the formation of largescale eddies and wrinkles are, the higher will be the turbulent burning velocity and flame propagation speed, as also reported in [40], [41]. Besides, higher flame wrinkling increases the flame burning area. All these flame characteristics increase with the increase in flow-mixture velocity. This could be verified with the PIV data. As the flow velocity increases, many high energies fluid structures form in the fluid domain. These fluid structures cause an increase in turbulent eddy diffusivity. The higher turbulent diffusivity outplays over the strain rate. Therefore, the turbulent flame burning velocity increases. Consequently, the flame propagation speed (rate) and the flame burning area increases.

The effect of grids on flame characteristics has also been studied. The flames under grid 1 and grid 3 (small hole diameter grids) have more wrinkle growths as evident from Figure 43-45. These grids induce more flame-flame interaction within the flame core. It happens because of the higher thermal instabilities and flow fluctuations generated by these two grids. However, the presence of large-scale wrinkles is comparatively less. Thus, the flame stretching and flame width are less under grid 1 and 3. It is also observed that the higher blockage ratio grids with

large hole diameters strongly accelerate the flame evolution compared to the smaller blockage ratio grids with a small hole diameter.

It is clear from Figure 43-45 that the large hole diameter grids (grid 2 and 4) induce more pinch-off and burnout events. It happens because they generate many large-scale fluid structures inside the combustor. They shattered the reaction zone. It also causes a higher fluctuation in the flow. On the other hand, grids with a smaller hole diameter (grid 1 and 3) produce a small-scale continuous fluid structure in the flow. Therefore, the reaction zone is less shattered. Consequently, the pinch-off and burnout event is less dominant.

The effect of two other Re's (30000 and 64000) on flame evolution has also been studied. The flame expansion rate is faster at Re =64000 compared to Re =30000 and 15000 (shown in Figure 43-51). The local strain rate increases with the increase in flow velocity. Therefore, the local strain rate is higher at Re = 64000 compared to Re = 30000 and 15000. Local strain tries to suppress the flame growth rate, however, the higher-order turbulence helps to overcome this adverse effect. Thus, the flame continues to expand even at higher turbulence conditions. Consequently, the flame expansion rate is higher at Re =64000 compared to Re= 30000 and 15000. Similar research on flame expansion rate is reported in [41].
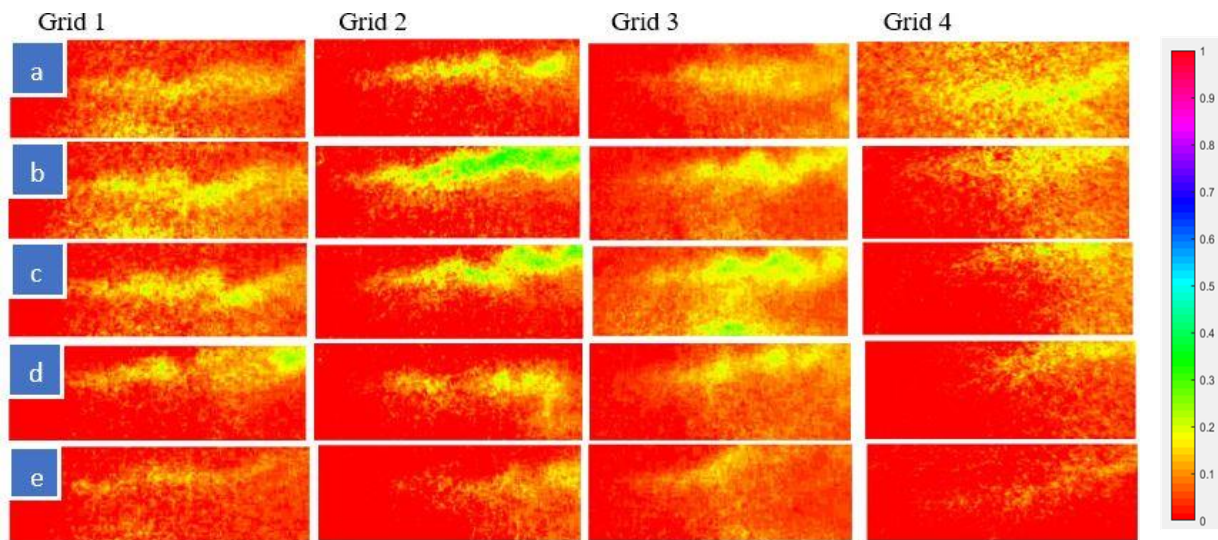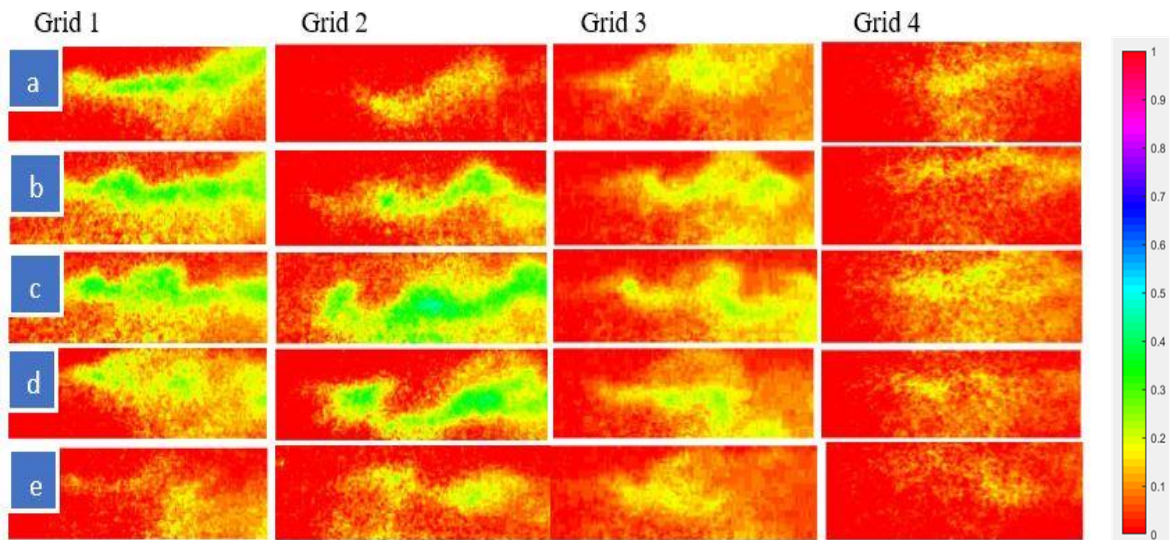
Figure 46. Flame profiles at $\phi = 0.8$ and Re = 30000 (25 CFM) (Fold the laptop screen for better visualization), HSV colormap array contains red, green, blue intensities with the range [0, 1]
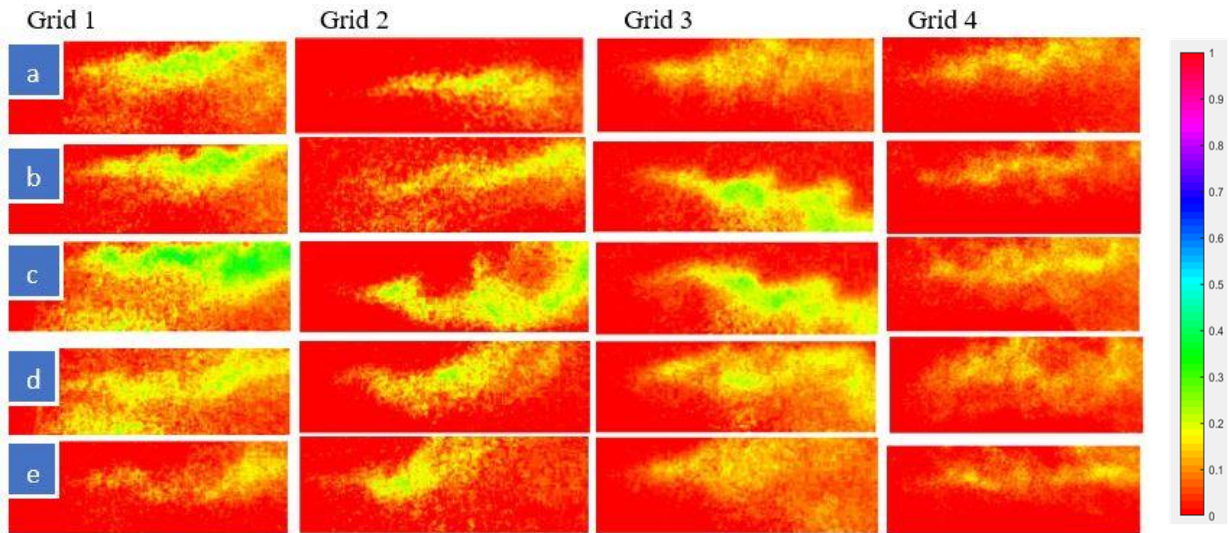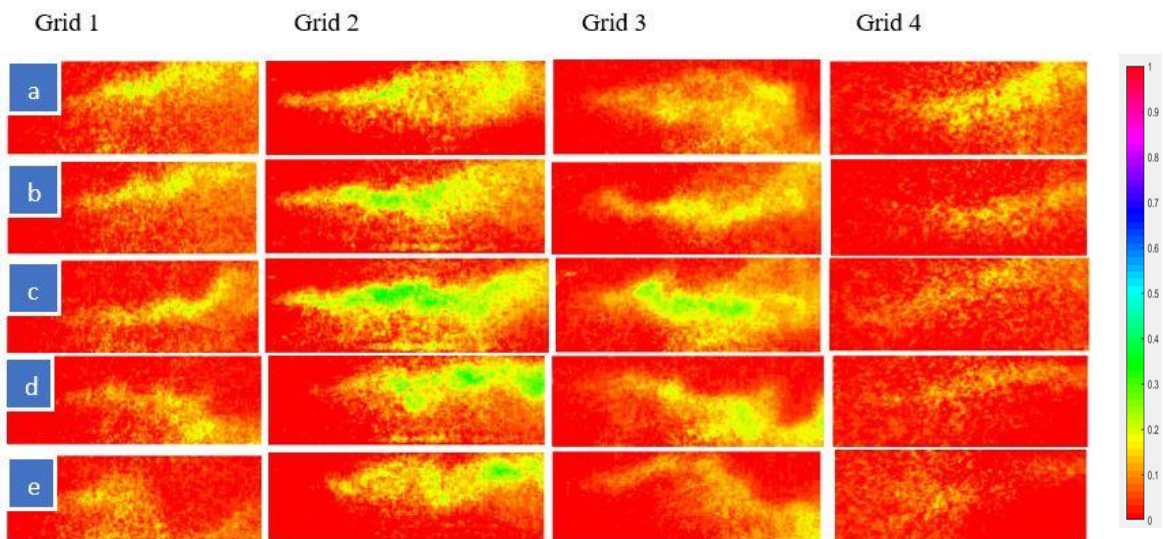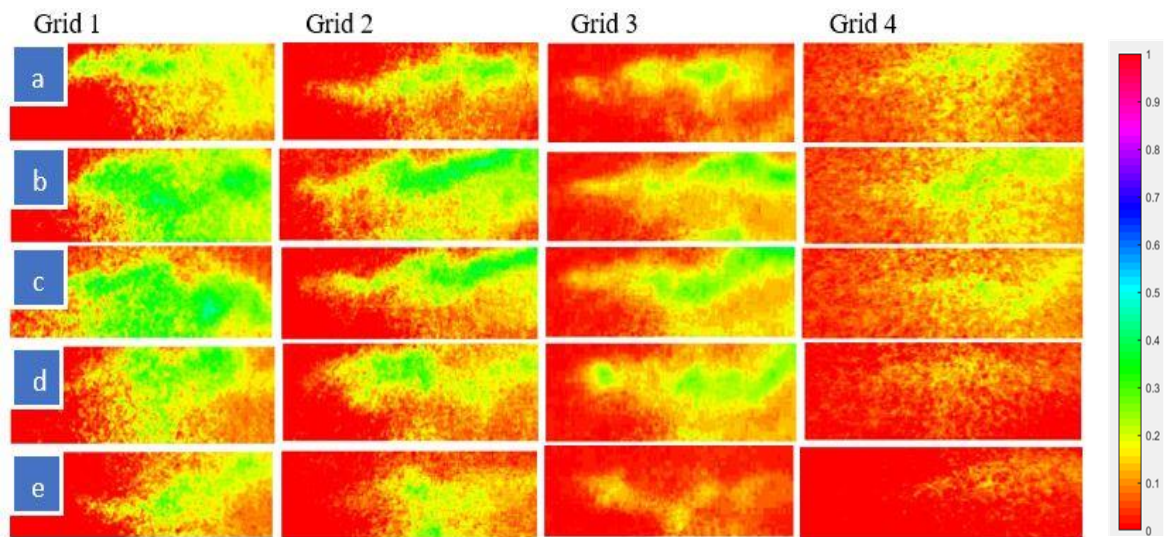

Figure 47. Flame profiles at $\phi = 1.0$ and Re = 30000 (25 CFM) (Fold the laptop screen for better visualization), HSV colormap array contains red, green, blue intensities with the range [0, 1]
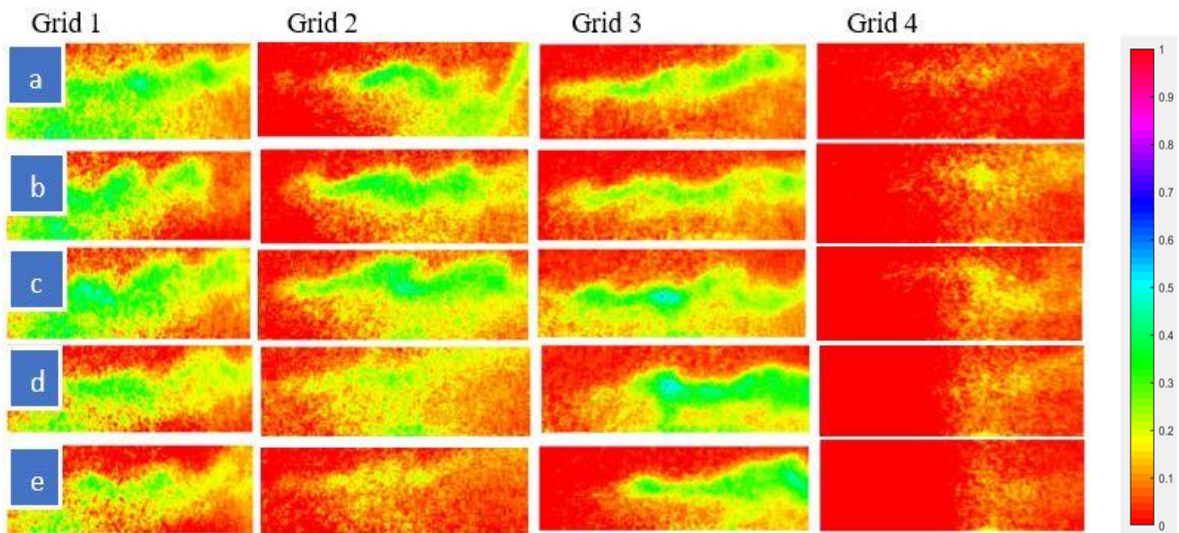
Figure 48. Flame profiles at ϕ = 1.2 and Re = 30000 (25 CFM) (Fold the laptop screen for better visualization), HSV colormap array contains red, green, blue intensities with the range [0, 1]
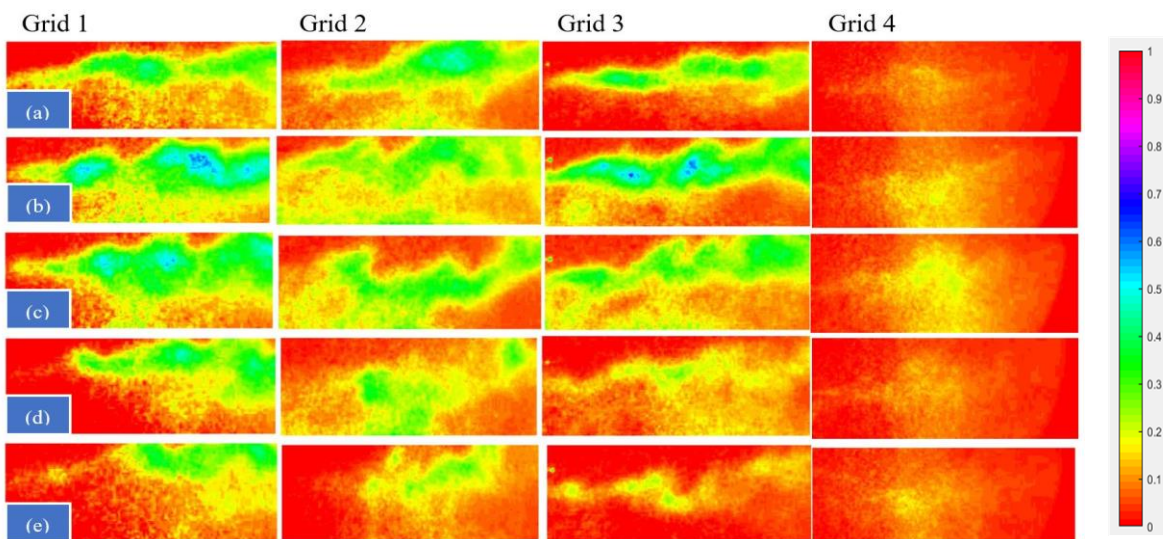
Figure 49. Flame profiles at ϕ = 0.8 and Re = 64000 (50 CFM) (Fold the laptop screen for better visualization), HSV colormap array contains red, green, blue intensities with the range [0, 1]
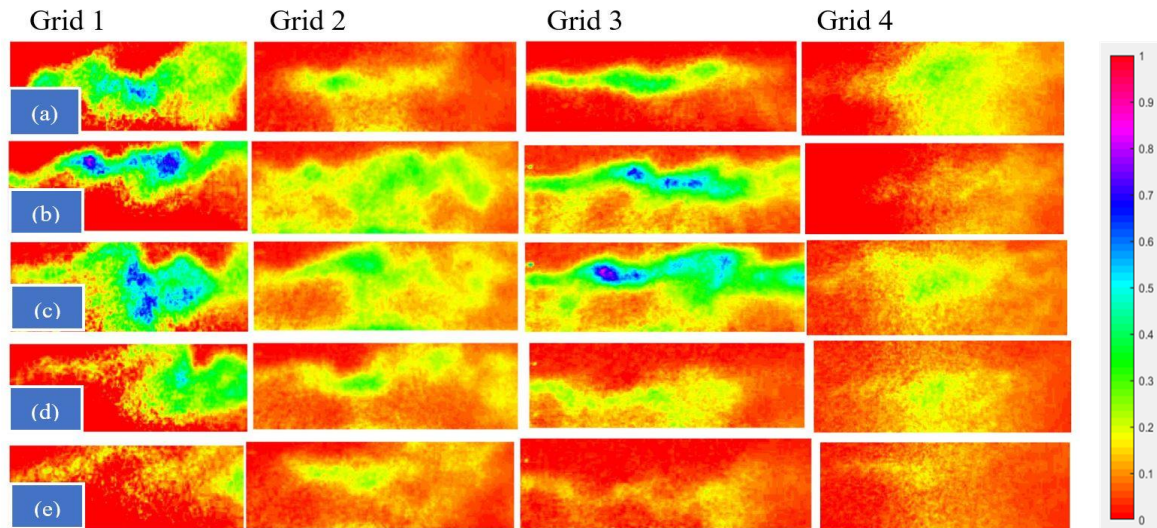
Figure 50. Flame profiles at ϕ = 1.0 and Re = 64000 (50 CFM) (Fold the laptop screen for better visualization), HSV colormap array contains red, green, blue intensities with the range [0, 1]

Figure 51. Flame profiles at ϕ = 1.2 and Re = 64000 (50 CFM) (Fold the laptop screen for better visualization), HSV colormap array contains red, green, blue intensities with the range [0, 1]

The flame wrinkling is higher at Re = 64000 compared to Re =30000 and 15000. The flow fluctuations, the formation of small-scale eddies and flame instabilities are higher at Re = 64000. This causes a massive change in flame-flame interaction. This interaction causes an abrupt increase in flame wrinkling at Re = 64000 (shown in Figure 49-51 (b & c)). It is also observed that the flame wrinkling increases with the increase in equivalence ratios (ϕ). At Re = 64000 and ϕ>1, the flame wrinkling rate is maximum.

Besides, at Re = 64000, there is a more presence of large-scale fluid-structures in the fluid domain. They bump into the reaction zone and make it more shattered. The shattered reaction zone is further affected by the higher flow fluctuation, turbulence intensity, vorticity, and thermal diffusion. Consequently, the flamelet breakdown and burnout are higher at Re =64000 compared to Re =30000 and 15000 (shown in Figure 49-51 (d & e).

The flame stretching is higher at Re = 64000 compared to Re = 30000 and 15000. There is a presence of many large-scale wrinkles in the flame at Re =64000. These large-scale wrinkles interact with each other. They form more wrinkles in the flame fronts. The curvatures of those wrinkles are high as evident from Figure 49-51 (b & c). The flame stretched across the maximum curvatures of those wrinkles. Therefore, the flame stretching is higher at Re =64000.

The flame front broadening increases with the increase in flow mixture velocity. At Re =64000, the flow mixture velocity (40 m/s) dominates over eddy viscosity ($u'l_o \ or \ u'\eta$). The flame broadening at Re =64000 is further accelerated by the infusion of small eddies into the flame core. It is also observed from Figure 43-51 that the flame broadening is mostly controlled by the turbulence than the flame wrinkling.

Flame edges are also generated using the in-house MATLAB based code. The flame edges are presented in Figure 52-54 (for Re = 15000), Figure 55-57 (for Re = 30000) and Figure 58-60 (for Re = 64000). The wrinkle initiation and their growth could be seen clearly in Figure 52-60. The wrinkle shape and size could be better explained using the flame edges. It is observed that wrinkle has an irregular shape. They have a handgrip like structures ((shown in Figure 52-60 (b & c)). Their shape does not change throughout the flame evolution. However, the size of the wrinkle reduces as the flame progresses downstream.
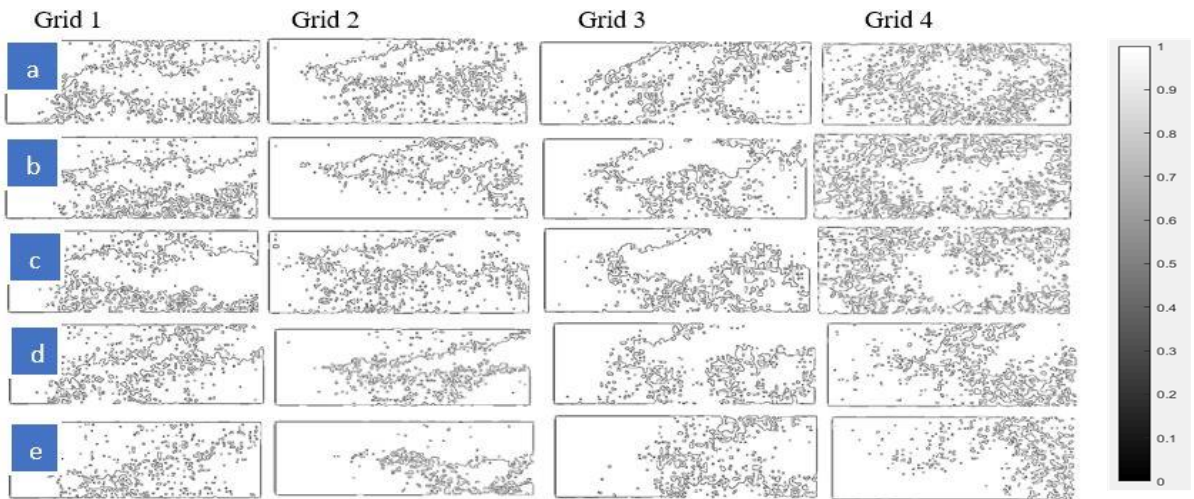
Figure 52. Flame Edges at ɸ = 0.8 and Re = 15000 (12 CFM) (Fold the laptop screen for better visualization)
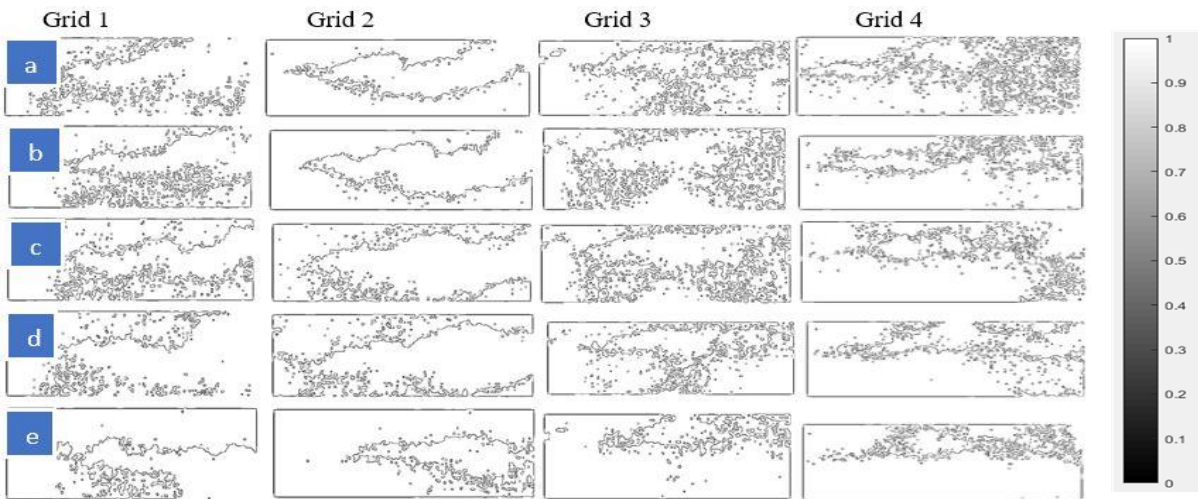
Figure 53. Flame Edges at ɸ = 1.0 and Re = 15000 (12 CFM) (Fold the laptop screen for better visualization)

Figure 54. Flame Edges at ɸ = 1.2 and Re = 15000 (12 CFM) (Fold the laptop screen for better visualization)
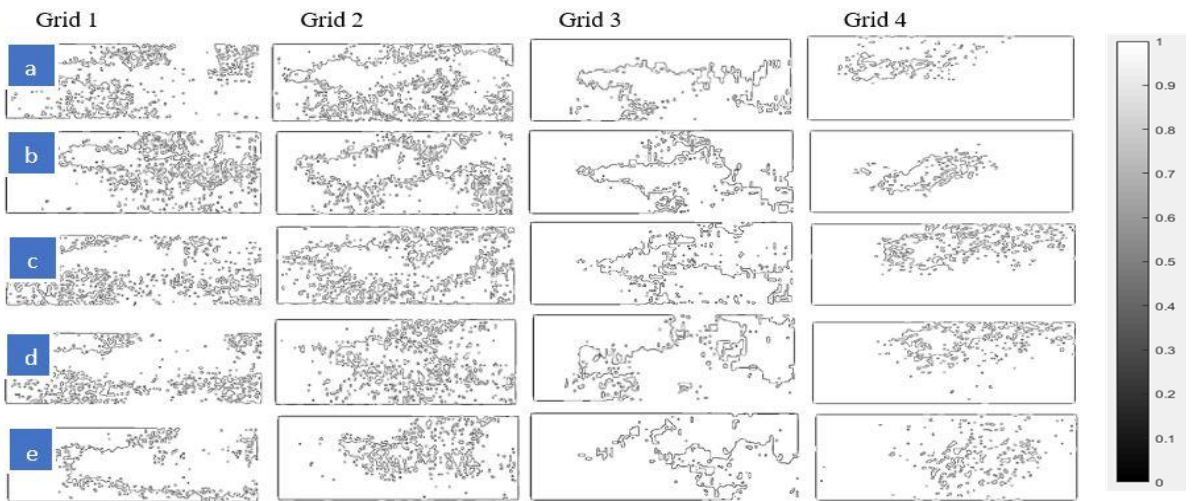
Figure 55. Flame Edges at $\phi = 0.8$ and Re = 30000 (25 CFM) (Fold the laptop screen for better visualization)
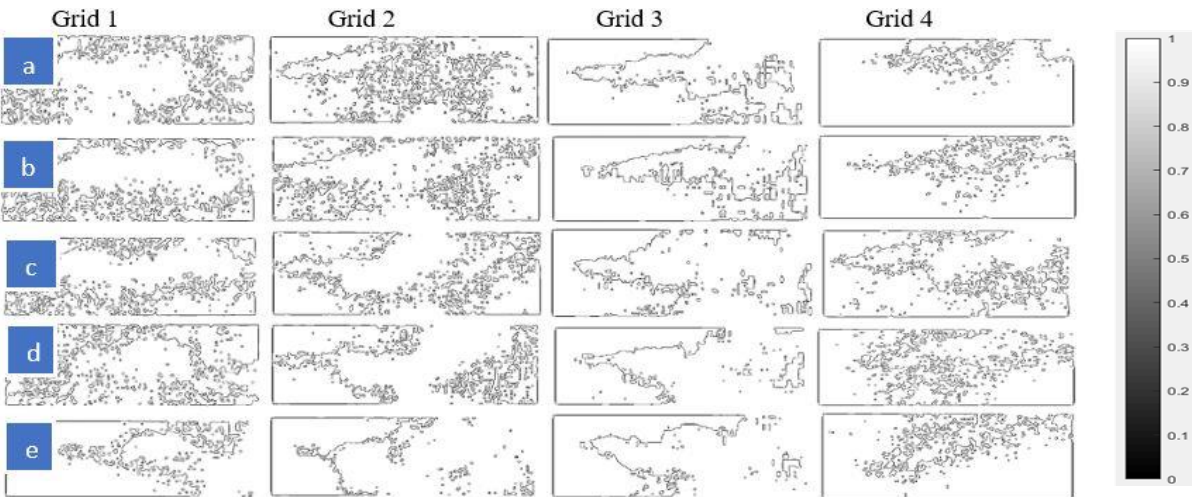
Figure 56. Flame Edges at $\phi = 1.0$ and Re = 30000 (25 CFM) (Fold the laptop screen for better visualization)
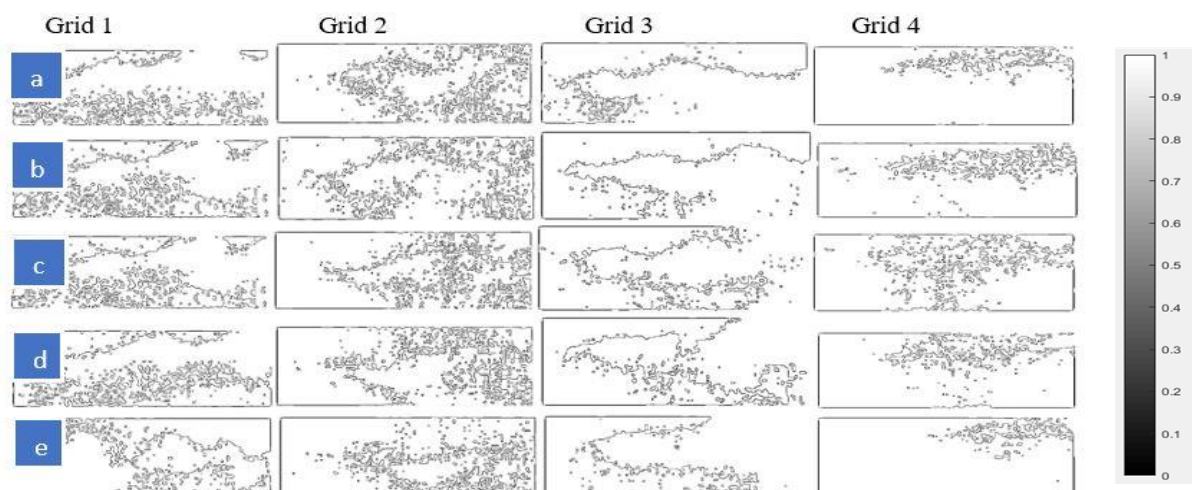
Figure 57. Flame Edges at ɸ = 1.2 and Re = 30000 (25 CFM) (Fold the laptop screen for better visualization)
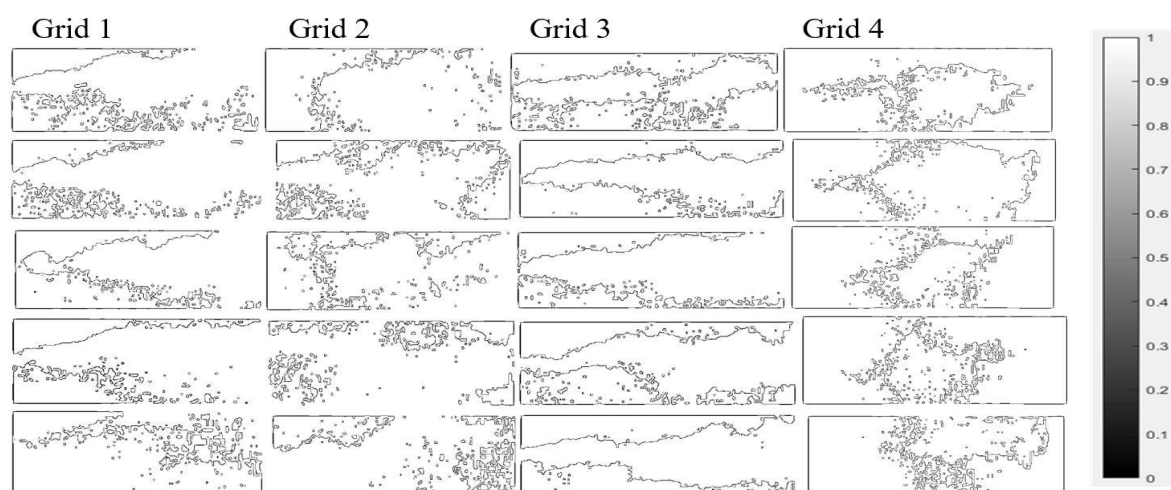
Figure 58. Flame Edges at ɸ = 0.8 and Re = 64000 (50 CFM) (Fold the laptop screen for better visualization)
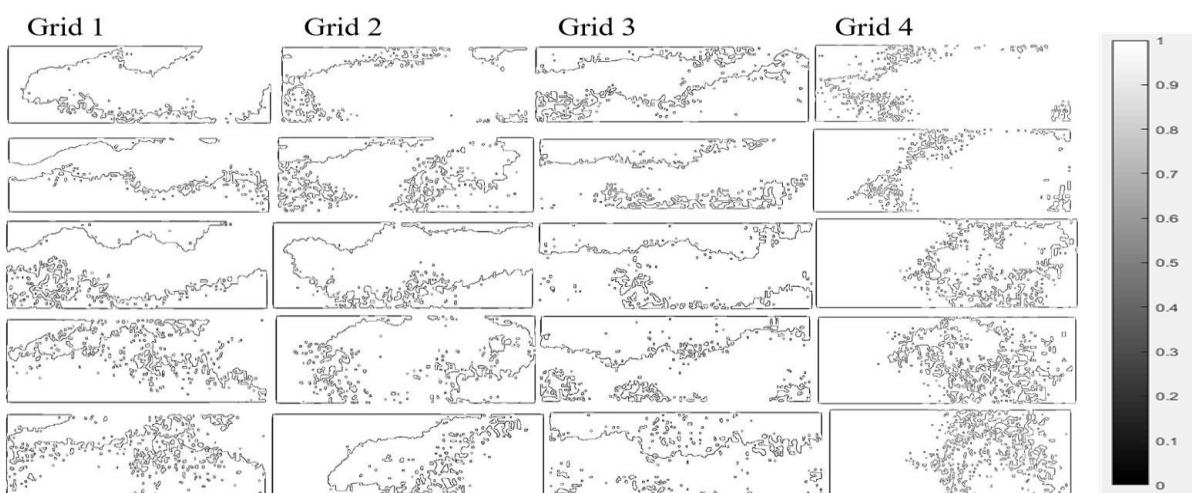
Figure 59. Flame Edges at ɸ = 1.0 and Re = 64000 (50 CFM) (Fold the laptop screen for better visualization)
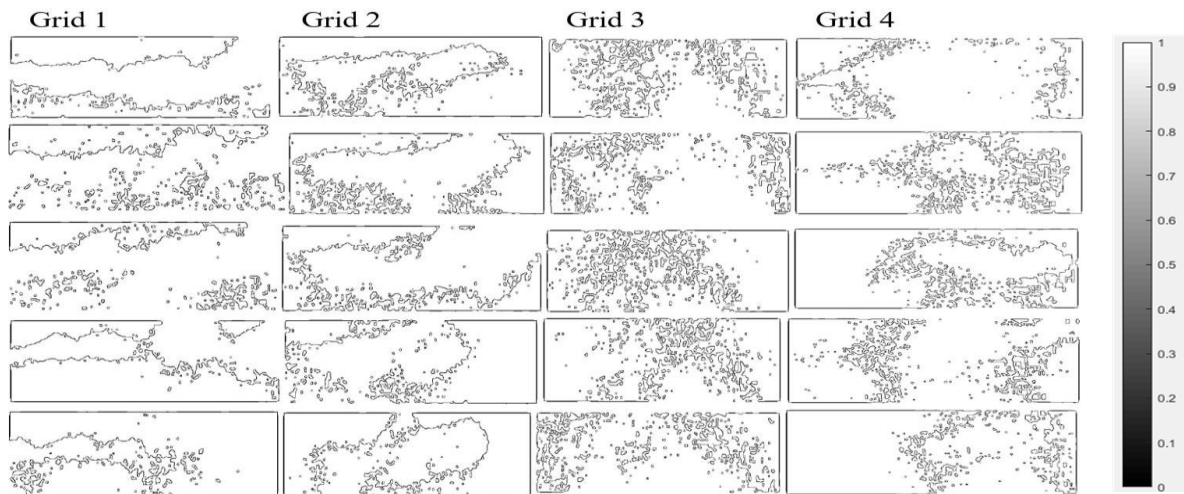
Figure 60. Flame Edges at ϕ = 1.2 and Re = 64000 (50 CFM) (Fold the laptop screen for better visualization

The flame edge profile shows that there is a formation of many small eddies at the recirculation zone. It validates the role of the backward-facing step in flame anchoring. Flame has more fluctuation in downstream as observed from Figure 52-60. It also shows that flame wrinkling and turbulence control flame growth. However, flame growth is mostly controlled by turbulence than the flame wrinkling.

Flame edge profile indicates that the flame is continuous and there is no flame extinction. It happens because the wrinkle formation was not too extreme at all flow conditions (see Figure 52-60). Wrinkle formation was just enough to maintain a continuous flame. The flame edges also show how the small-eddy forms and infused to the flame. The presence of turbulent vorticities is higher at Re =64000 compared to Re =30000 and 15000. Therefore, flamelet detachment and reattachment are higher at Re = 64000. The higher local flow momentum and vorticity-strain effects are responsible for this behavior (shown in Figure 52-60 (b,c, & d)).

The flame edge profile shows that the flame width (lateral) is thinner at Re = 64000, less thin at Re =30000 and wider at Re =15000. This could be explained with the help of flow

78

momentum and flow residence time. At Re = 64000, the flow momentum is extremely high, therefore the flow travels very fast inside the combustor. The flame does not have enough time to expand (lateral). Consequently, flame is thinner at Re =64000. At Re =30000, the flow momentum is relatively low. Thus, the flame propagation is not too fast. The flame has some time to expand. Consequently, the flame is less thin at Re =30000. The flow residence time is relatively higher at Re =15000. Thus, the flame has enough time to expand. Consequently, the flame is wider at Re =15000.

The flame edges show that the flamelet breakdown and burnout are higher at Re =64000 compared to Re =30000 and 15000. It is because the flow momentum, turbulent fluctuations, and thermal diffusion are very high at Re = 64000. It is observed that the flame wrinkling is higher under grid 1 and 3, whereas, flamelet breakdown and burnout are higher under grid 2 and 4. The same behavior is also noticed from flame profiles presented in Figure 43-51. A similar observation is also reported in [46].

It is seen from Figure 43-60 that the velocity fluctuation is higher at Re =64000 (50 CFM) compared to Re = 30000 (25 CFM) and 15000 (12 CFM). Therefore, the turbulent burning velocity should be higher at Re = 64000. Also, because of the higher flame thermal diffusion, flame propagation speed is expected to be higher at Re =64000. The flame under grid 2 and 4 is expected to have higher turbulent burning velocity. However, combustion modeling needs to be carried out to conclude on these issues.

The flame evolution shows that the CH layer or the reaction zone layer remains thin at all flow conditions. The CH layer thickness slightly increases towards the downstream. It happens because the turbulence dominates over strain-rate at the downstream. It is also observed that the CH layer is flame let like. CH signal decreases with the increase in flow mixture velocity. Therefore, to have a better CH signal at an extreme turbulence environment

(Re >64000), the reactants should be preheated. More specifically air has to be preheated at an elevated temperature. The incorporation of higher-order alkaline to the methane-air mixture might resolve this issue. However, it might slow down the hydrocarbon reaction. Therefore, extra care should be taken during the mixture preparation.

The effect of equivalence ratios on flame evolution is investigated at all flow conditions. As the equivalence ratio (ϕ) increases the heat release rate increases too. This happens because of the increase in combustion radical fraction and their reaction rate. A similar behavior is reports in [1], [41], [52]. The increase of temperature (i.e. heat release) with ϕ is observed using the LabView tool installed in the system. The flame reaches the maximum burnt temperature at ϕ =1.2.

The flame surface consumption rate increases with the increase in fuel loading. Therefore, the flame surface area and flame length are expected to increase at ϕ>1. The same behavior is reported in [53]. The flame surface area has a direct relation with the flame burning velocity and flame front curvature. Therefore, at higher ϕ, the flame burning area and flame front curvature should increase too. However, combustion modeling needs to be carried out to justify these flame characteristics.

Less discontinuity in the flame is noticed for the lean mixture (ϕ =0.8), whereas, a moderate level discontinuity is seen at ϕ =1.2 (see Figure 53-60). However, this small magnitude change in discontinuity does not affect flame stability. The same information is reported in [13].

4.2.1 Flame Regime Detection and Flame Behavior

The PIV results and the laminar flame characteristics are used to locate the flame regime on the Borghi-Peters diagram (shown in Figure 61). The laminar flame characteristics such as laminar flame speed, laminar flame thickness are obtained from the literature [54], [55]. The flow data used in flame regime detection are presented in Table 13 and Table 14.

The thickened flame (thin reaction zone) is observed at all conditions except the grid 1 at Re =15000 (12 CFM). The velocity fluctuation relative to laminar flame speed is low under grid 1 at Re = 15000. Thus flame falls in corrugated flamelet regime. For all other conditions, the flame falls in the thin reaction zone. The thickness of small-scale eddies (Kolmogorov scales,η) is less than the flame thickness (δ_T). Therefore, small-scale eddies infused to the flame and make the reaction zone thinner. At Re = 64000, there is a more infusion of small-eddies in the reaction zone. Therefore, the reaction zone is much thinner at Re =64000. The flame thickness is less thin at Re =30000 and wider at Re =15000. Flame falls in the thin reaction zone and there is no flame breaking up. Thus it is hypothesized that the flame wrinkling is not severe and flame stabilized at all flow conditions.
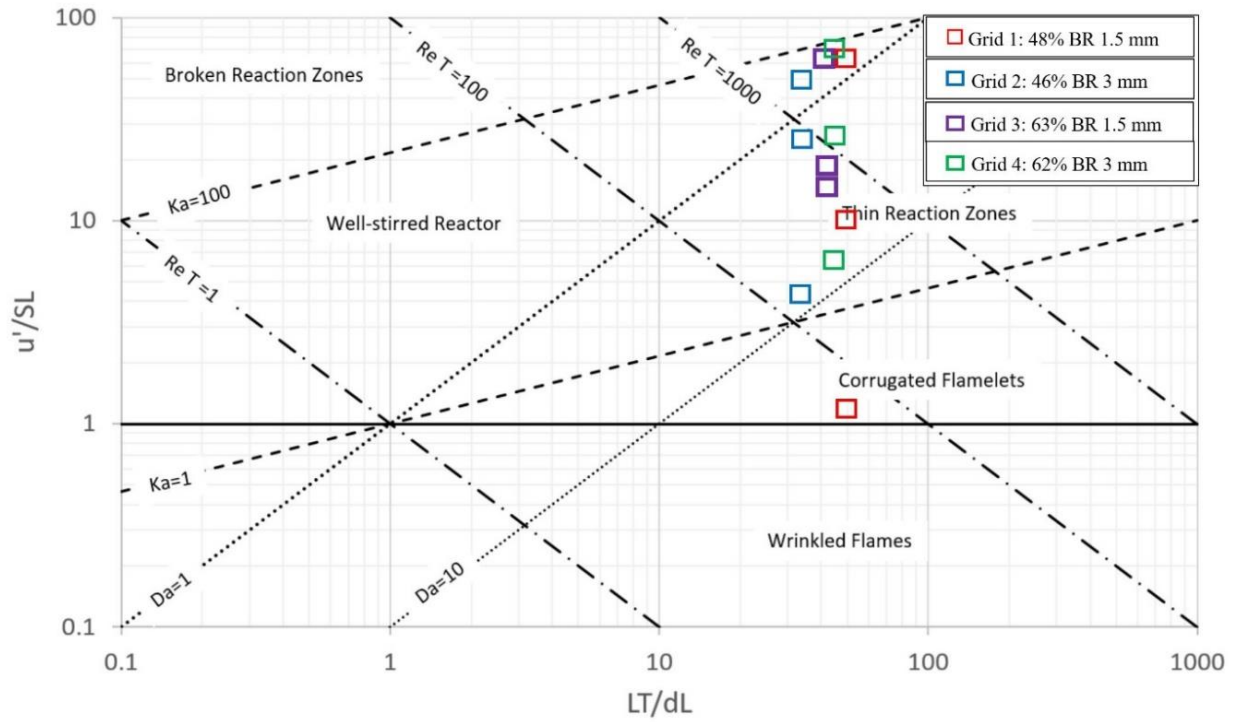
Figure 61. Flame regime detection on Borghi-Peter's diagram [graph is reproduced using the data of [41]]

Table 13. Flow characteristics under all grids [41]

Grid	Re	ϕ	U_{bulk} (m/s)	U_{PIV} (m/s)	u'(m/s)	Da	Ka	Re_T	u'/S_L	L_T	L_T/δ_L
48%BR-1.5mm dia.	15000		10	13	1.1	21.3	0.8	147.5	3.0	0.0173	49.4
	30000	1.0	20	25	3.5	18.8	7.0	458.4	9.3	0.0173	49.4
	64000		40	27	23.4	0.9	70.3	3034.6	61.5	0.0173	49.4
46%BR-3mm dia.	15000		10	11	1.7	34.2	1.7	234.2	4.4	0.0186	33.2
	30000	1.0	20	26	9.8	2.2	18.2	1364.7	25.7	0.0186	33.2
	64000		40	8	18.9	1.3	50.2	2647.4	49.8	0.0186	33.2
63%BR-1.5mm dia.	15000		10	14	5.5	5.1	10.3	604.5	14.5	0.0146	41.8
	30000	1.0	20	26	7.5	4.3	16.8	824.0	19.7	0.0146	41.8
	64000		40	28	25.6	0.9	90.2	2814.1	67.4	0.0146	41.8
62%BR-3mm dia.	15000		10	17	2.5	13.9	3.4	300.5	6.6	0.0160	45.6
	30000	1.0	20	27	11.0	1.8	24.6	1315.9	28.9	0.0160	45.6
	64000		40	33	27.7	0.8	95.9	3316.9	72.8	0.0160	45.6

Table 14. The parameters used in Borghi-Peter's Diagram [41]

Flow Rate (CFM)	Grid 1		Grid 2		Grid 3		Grid 4	
	L_T/δ_L	u'/S_L	L_T/δ_L	u'/S_L	L_T/δ_L	u'/S_L	L_T/δ_L	u'/S_L
12	49.371	2.987	33.171	4.405	41.77	14.471	45.57	6.594
25	49.371	9.285	33.171	25.665	41.77	19.727	45.57	28.875
50	49.371	61.465	33.171	49.97	41.77	67.37	45.57	72.785

The detection of flame regime gives insight into the flame behavior. The location of the flame is on the top of the thin reaction zone regime under grid 2 and 4. It means that Ka is higher and thermal diffusions dominate over reaction rate under grid 2 and 4. It also infers that the flame has more flamelet breakdown as it is very close to the broken reaction zone. On the other hand, the flame is located at the core of the thin reaction zone under grid 1 and 3. The flame under grid 1 and 3 have a higher reaction rate compared to the diffusion rate i.e. Da is less. Therefore, flame wrinkling is higher and the flame cannot move to the broken reaction zone under grid 1 and 3.

The behavior of flame thickness could also be explained using flame regime characteristics. The flame under grid 2 and 4 have higher Karlovitz number (Ka). The Karlovitz number is directly related to the flame thickness (δ_T). Therefore, the higher flame thickness (δ_T) is expected under grid 2 and 4. On the other hand, the flame thickness is expected to be less under grid 1 and 3 since Ka is less. The same behavior of flame thickness is observed from flame profiles/edges reported before.

As Re increases, Da is decreased (shown in Figure 61). It means that the flame wrinkling rate increases with Re. It happens because the turbulent time-scale dominates over chemical time-scale as Re increases. Also, as Re increases, Ka increases too (shown in Figure 61). It means that the flamelet breakdown/burnout increases with Re. It happens because of

Kolmogorov time-scale is less than the chemical time-scale at higher-order Re. In short, the flame evolution is fast at higher-order turbulence condition.

4.3 Validation of Flame Regime Characteristics

The PIV data and laminar flame characteristics are used to detect the flame regime on Borghi-Peter's diagram. The flame mostly falls in a thin reaction zone regime. However, PIV derived data such as Da, Ka, L_T, u' etc has to be verified to make a rigid conclusion on flame regime characteristics. To validate the PIV results, a separate approach is taken. A premixed combustion model (PCM) is used to validate the Da used for flame regime detection. In this part of this dissertation, a brief overview of the model and results will be discussed. In the end, the Da derived from PIV and PCM will be compared. A conclusion will be made on flame regime characteristics.

Pressure based transient solver is used to solve the combustion inside the combustor. The PCM is run for all grids and flow conditions. It is also run at stoichiometric condition, Φ = 1. The solver and flame model conditions used for combustion modeling are listed in Table 15 and 16 respectively.

Table 15. Solver conditions used in premixed combustion model (PCM)

Solver	
Solver Type	Pressure-based
Velocity Formulation	Absolute
Time	Transient
2D Space	Planar

A viscous model called direct eddy simulation (DES) is used to trace the energy change during the combustion. The viscous heating and curvature corrections options are used to get better convergence in the energy model. To solve the Reynolds stresses, SST K-Omega is used. The extended coherent model and Poinsot model are used as the species models. The species

models help to get the premixed combustion properties. It is to say that PCM does not have the option of setting the H$_2$-air as the pilot flame subsystem. PCM allows setting a spark ignition that would generate the same amount of energy as expected from the actual pilot flame. Thus, to mimic the pilot flame, spark ignition is set up in PCM. For the spark-ignition engine, a flame Kernel radius of 1mm to 3.5 mm is used [56], [57]. For this study, because of the higher turbulent combustion, the flame kernel radius of 5mm is considered. The PCM is run for the 30s-60s. Turbulent curvature is used as the flame speed model.

Table 16. Conditions of viscous models, species models and spark ignition used in PCM

Viscous Models, Species Models, and Spark Igniters	
Energy	On
Viscous Model	Direct Eddy Simulation (DES) • Delayed DES • Viscous heating and curvature corrections • Shielding Function: DDES RANS Model: SST K-Omega • Low Re corrections
Species Model	Premixed Combustion (Adiabatic) Premixed Model: Extended Coherent Flame Model (ECFM) Constants Used in ECFM: Poinsot • Turbulent Schmidt Number: 0.7 • Wall Flux Coefficient: 0.5
Spark Ignition	Spark Locations: x=0.08 m, y=0.025 m Initial Flame Kernel Radius: 0.005 m Flame Speed Model: Turbulent Curvature ECFM Spark Model: Turbulent

The grid domain is set up based on the properties listed in Table 3. Figure 62 shows the grid with fine mesh used for PCM analysis. Mesh independence study is carried out at different Reynolds conditions. Nodes of 78001 and elements of 144998 are found to be the optimized mesh conditions for PCM study.
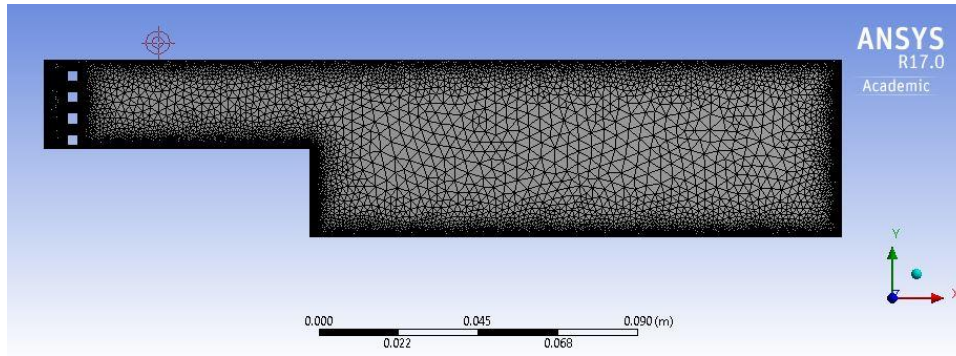
Figure 62. The meshing of the grid used in PCM study

Once the Mesh is generated, the boundary conditions are set for PCM analysis. For all test conditions, steel is used as the wall material. Stationary walls and no-slip conditions are used for momentum analysis. Also, wall roughness of 0.5 mm, wall temperature of 300 K and zero thermal heat flux are considered for the wall boundary conditions.

The flow inlet velocities of 10 m/s, 20 m/s and 40 m/s are used as the inlet boundary conditions. Also, no perturbation option is used for the fluctuating velocity algorithm. Besides, an initial gauge pressure of 101.352 kPa, a turbulent intensity of 15% and a turbulent length scale of 7.87 mm are used as the flow inlet conditions. For the outlet, the outflow condition is considered. The properties listed in Tables 4 and 5 are used to set the boundary conditions and operating conditions respectively.

Once the boundary conditions are set, the next step is to set the solution methods and control schemes. The final steps are to initialize the solution and run the calculation for the desired period of combustion. The solution methods, control schemes, and conditions for solution initialization are listed in Table 17.

Table 17. The conditions used for solution methods, control schemes and solution initialization

Solution Methods, Control Schemes and Solution Initialization	

Solution Methods	Pressure Velocity Coupling
	    • Scheme: Simple
	Spatial Discretization
	    • Gradient: Least Square Cell-Based
	    • Pressure: Standard
	Momentum/Turbulent Kinetic Energy/Species Dissipation Rate/Progress Variables/Flame Area Density
	    • Second-order Upwind
	Transient Formulation
	    • Second-order Implicit with Higher-order term Relaxation

Solution Controls	Under-relaxation Factors with 0.3 for all variables
Solution Initialization	Hybrid Initialization Method

After the solution initialization, the combustion model is run for the 30s-60s. For higher Re like 64000, combustion has to run for more than 30s. It is because flame takes time to stabilizes inside the combustor. The model is run at all flow conditions (12 CFM, 25CFM and 50 CFM) and Φ =1. For each run, turbulence characteristics, premixed combustion characteristics, velocity, pressure, and temperature characteristics are determined. The PCM derived characteristics match with the PIV results. In this part, only the Da and turbulent flame speed (S_T) will be compared. Table 18 shows the Da values found from both PCM and PIV analysis.

Table 18. Damkohler number (Da) found from PIV and premixed combustion model (PCM)

Re	Grid 1		Grid 2		Grid 3		Grid 4	
	PIV	PCM	PIV	PCM	PIV	PCM	PIV	PCM
15000	21.3	20.5	34.2	33.1	5.1	5.2	13.9	13.1
30000	18.8	17.8	2.2	2.5	4.3	4	1.8	2.1
64000	0.9	0.95	1.3	1.4	0.9	0.97	0.8	0.78

It is clear from Table 18 and Figure 63 that the discrepancy of the Da values is very low (~10% avg.). The methods of analysis, assumptions, design and systematic uncertainties are different in PIV and PCM. These are the vital factors that cause this discrepancy. The

repeatability of both the PIV test and PCM needs to be studied to conclude this issue. Based on the current analysis, it is confirmed that flame regime detection is right. It also validated that the flame falls in a thin reaction zone (thickened flame regime).
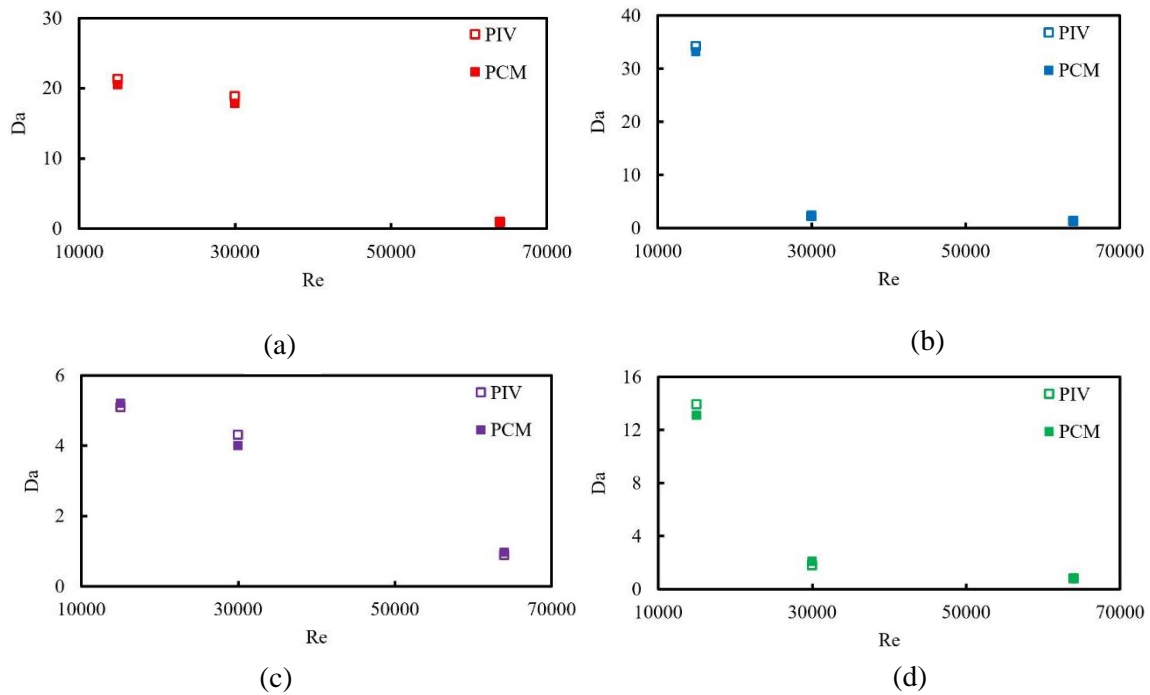
Figure 63. Graphical representation of Da values derived from PIV and PCM analysis, (a) Grid 1 (48% BR), (b) Grid 2 (46% BR), (c) Grid 3 (63% BR), and (d) Grid 4 (62% BR).

PCM has good accuracy in predicting the combustion characteristics at higher-order turbulence. Therefore, PCM data could resolve some of the unknown combustion parameters that have not been answered by PIV and PLIF experiments. From the PLIF study, it is observed that the flame speed increases with Re. PLIF study also indicates that the flame speed is higher under grid 2 and 4. However, these statements need to be verified. For this, the author took an attempt to check the turbulent flame speed (S_T) using the PCM analysis. PCM generated turbulent flame speeds (S_T) are listed in Table 19 and Figure 64.

Table 19. Turbulent flame speed for all grids

Re	Turbulent Flame Speed, S_T (m/s)			
	Grid 1	Grid 2	Grid 3	Grid 4
15000	12.4	17.3	14.0	17.9
30000	19.9	22.1	18.6	23.2
64000	41.5	45.8	40.1	48.6
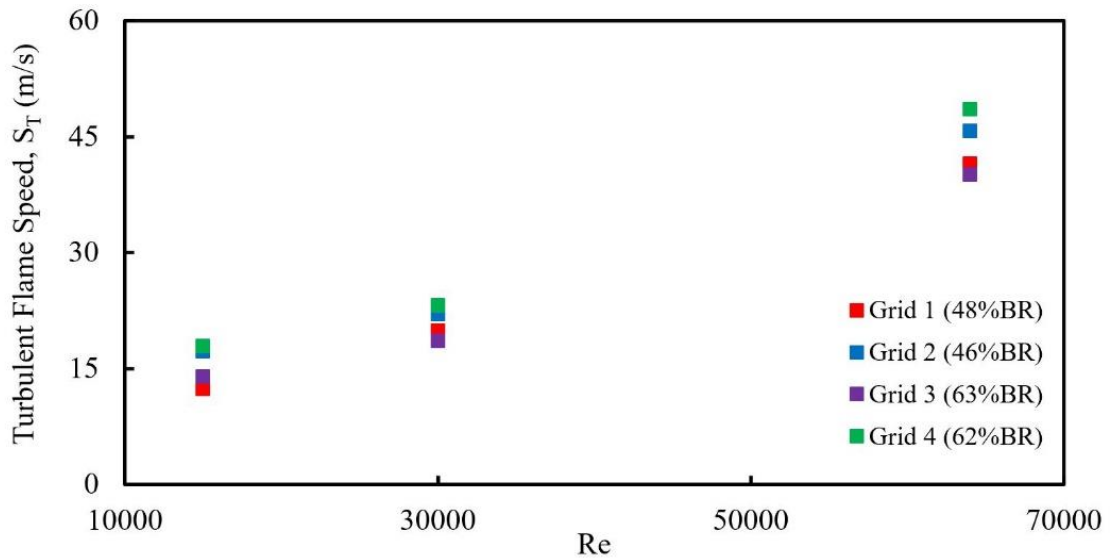
Figure 64. The turbulent flame speed at Re =15000, 30000 and 64000.

The turbulent flame speed (S_T) increases with the mixture flow rates. It is also seen that S_T is higher under grid 2 and 4 (large hole diameter grids). It varies from 17.3 m/s to 48.6 m/s under grid 2 and 4. However, S_T is low under grid 1 and 3 (small hole diameter grids). It varies from 12.4 m/s to 41.5 m/s under grid 1 and 3. PCM generated turbulent flame speed matches with the trend observed by flame profiles/edges. Therefore, the PLIF derived flame characteristics reported in this dissertation are valid.

Chapter 5: Summary, Conclusions and Future Works

5.1 Summary and Concluding Remarks:

The non-intrusive laser techniques such as PIV and PLIF have opened the door to combustion engineers to experimentally check the performance of the high-speed combustors. This research aims to develop a combustion test facility, experimental methodologies and data analysis schemes for the study of next-generation high-speed combustion. The outcome of this research could be used to develop and/or modify the combustion models used for supersonic and hypersonic combustion. Also, this research intends to come up with an optimized design of high-speed combustor.

A 10 kHz time-resolved particle image velocimetry (PIV) is used to study the flow characteristics such as velocities (u, v), turbulent intensities (I), vorticities (ω), turbulent kinetic energy (TKE), etc. Adaptive PIV tools and Statistical tools are used to determine these characteristics. The results are presented in the contour map so that a better understanding of flow behavior could be made. The effect of turbulence and grids geometries on the flow characteristics have been presented. It is observed that the velocity gradient is high at the shear layers. The recirculation zone shows the highest concentration of small eddies which helps in flow mixing. The proposed synchronization parameters and PIV post-processing techniques can resolve the high-velocity gradients, turbulent intensities, and vorticities present at the recirculation zone. Maximum velocity of 17 m/s, 27 m/s, 33 m/s are observed at Re =15000 (12 CFM), Re = 30000 (25 CFM) and Re =64000 (50 CFM) respectively. Proper orthogonal decomposition (POD) is used to study the fluid flow energy structure. The energy structures are used to understand the energy cascading during the vortex breakdown. It is also used to determine the turbulent integral length scale and Kolmogorov scale.

The effect of grids on flow characteristics is investigated. An average of 5 m/s flow acceleration is observed when compared to the theoretical values. It is seen that the fully developed flow enters the combustor. At Re = 15000 and 30000, u component dominates over v component. However, at Re =64000, v component takes the main role and u component drops by 10 m/s. This could be resolved by moving the grid further upstream on the combustor inlet. It is observed that the grid has less impact on u', it is the bulk flow rate that controls the flow fluctuation. The PIV system used in this research can resolve the high-intensity zones inside the flow domain, however, at Re =64000, the system reaches its maximum resolution capacity. A high-resolution camera and filter may be needed for future high-speed flow visualization.

A 10 kHz Planar laser-induced fluorescence (PLIF) is used to investigate the flame front characteristics. The PLIF system has a high temporal and spatial resolution of 100 um/pixel. The system is capable of detecting the flame front as low as 0.1 ms. Besides, the combustor is optically accessible. It allows the laser to enter the target area. In this research, CH-PLIF is chosen for the flame dynamic study. Among the three bands of CH, the C-X band has a higher potential of capturing the real-time flame evolution. CH bands need less laser power. They present during the main course of combustion. Also, they do not convect the flow downstream. Besides, they have higher excitation and emission coefficients. It enables capturing the real flame fronts. A wavelength of 314.415 nm is found to be the best wavelength for C-X CH-PLIF.

For the reactants, methane and air mixture are used. Hydron and air are used as the pilot mixture. The combustion tests are performed at Re =15000, 30000 and 64000 at atmospheric pressure and temperature. The equivalence ratios, $\Phi = 0.6$ to 1.2, turbulent length scales (L_T) and velocity fluctuations (u') are used for flame dynamics study. The turbulent length scales (L_T) are varied using turbulence inducing grids with blockage ratios from 46 % to 63% and hole diameter from 1.5 mm to 3mm. The velocity fluctuation (u') is changed using different

flow rates and grids. The flame parameters such as Turbulent Reynolds number (Re_T), Damkohler number (Da), Karlovitz number (Ka), etc are determined using the PIV and literature data. In this study, Da varies from 0.8 to 34, Ka changes from 0.8 to 95, Re_T varies from 147 to 3317, $\frac{u'}{S_L}$ changes from 3 to 72 etc.

It is observed that the velocity fluctuation (u') controls the flame front characteristics. The u' is mostly controlled by the flow rates and grid blockage ratios. It is also observed that for a grid, whatever the flow rates are, the turbulent length scales (L_T) are the same. As the Re increased, velocity fluctuation (u'), turbulent Reynolds number (Re$_T$), $\frac{u'}{S_L}$, and Karlovitz number (Ka) increases too. The opposite is true for Da.

The flame front has the burned gas zones inside the unburned gas zones and vice-versa. It is more visible in the corrugated flame regime. At Re =15000, the flame under grid 1 falls in the corrugated flame regime. There are formations of some corrugated pockets behind the flame front. The local hot spot or auto-ignition of the flammable mixture controls this behavior. Determination of the third velocity component (w) using two sets of cameras could provide further information on this issue.

The flame evolution has been studied using flame profiles. A MATLAB based image processing code has been developed to study the flame front characteristics. After the initiation of flame, there is a formation of flame wrinkles. Flow fluctuation, instabilities created by thermal expansion and buoyancy are responsible for this behavior. Besides, the change of local viscosity across the flame plays a vital role in flame wrinkling. As the flame moves downstream, there is a flamelet breakdown. The turbulence and local thermal energy fluctuation help in flamelet breakdown. Also, the large-scale fluid structures shattered the reaction zones and cause more breakdown in the flame front. The flamelet breakdown event is higher at the downstream near the bottom wall. This is because of the infusion of small eddies

to the flame core. The flamelet burnout is also dominant at the downstream. When the detached or loosely attached loop reaches a very high temperature, they self-ignite and disappear.

The effect of grids on flame evolution has also been studied. The flame wrinkling is found to be high under grid 1 and 3. Under these grids, the reaction rate is faster than the diffusion rate i.e. the chemical timescale is higher than the turbulent timescale. Therefore, flame under these grids mostly controlled by the chemistry than the turbulence. Consequently, the Da value is less. On the other hand, the flamelet breakdown and burnout events are higher under grid 2 and 4. The velocity fluctuation (u') and turbulent Intensity (I) are higher under these grids. In other words, the Kolmogorov scale is way less than the chemical timescale. Thus, the Ka value is higher under grid 2 and 4.

The flame stretching is found to be higher under grid 2 and 4. There is a formation of many large-scale eddies in the flow. These eddies interact and form new eddies. When they interact, the curvature of the flame fronts changes. The flame stretched towards the maximum area of the curvature. This is also justified by the increase in the Ka value under grid 2 and 4.

The flame broadening is also higher under grid 2 and 4. The turbulent eddies are high under these grids. The higher turbulent eddies enhance the heat and mass transfer to the reaction zone. Consequently, the local flame diffusivity increases. This causes a massive change in flame core structures. Thus, the flame broadened towards downstream. It is observed that the formation of large eddies and wrinkles accelerate the turbulent burning velocity and flame propagation speed. It is also observed that flame wrinkling increases the flame burning area.

The research has also been extended to see how the flow rates control the flame dynamics. The flame characteristics increase with the increase in flow-mixture velocity. As the Re increases, the presence of high energy fluid-structure increases too. This causes an increase in turbulent eddy diffusivity. The turbulent diffusivity outplays over the strain rate. Therefore,

the turbulent flame burning velocity increases. Consequently, the flame propagation speed (rate) and the flame burning area increases. It is postulated that the flame burning area and flame propagation speed are higher at Re =64000 compared to Re =30000 and 15000.

Da decreases with flow rates (Re). It means that the flame wrinkling increases. Similarly, Ka increases with the Re. It means that the flamelet breakdown, flamelet burnout, flame stretching, and flame broadening increase too.

It is investigated through the LABVIEW tool that the heat release rate (flame burning temperature) increases with the increase in Φ. This happens because of the increase in combustion radical fraction and their reaction rate. The flame surface consumption rate increases with the increase in Φ. Therefore, it is expected that the flame surface area, flame length, flame burning velocity, and flame front curvature will increase with ϕ. For a solid conclusion, extensive combustion modeling needs to be performed.

A separate MATLAB based code has also been developed to generate the flame edges. It is seen that the turbulent eddies are higher in the recirculation zone. Also, flame width increases in the downstream. Flame edges show that the wrinkle shapes are irregular. They retain their shapes. However, wrinkle size reduces as the flame grows. Flame edges also show that the flamelet breakdown is higher at the downstream near the bottom wall. The detachment and reattachment of the flamelets/pockets are seen behind the flame fronts. Flame edges confirm that the flame does not extinct. It validates the role of grids and the backward-facing step used in this research.

The PIV and flame characteristics are used in Borghi-peter's diagram to locate the flame. The flame under grid 1 at Re =15000 falls in the corrugated zone. A preheated reactant could be used to shift the flame to a thin reaction zone. The flame under all grids at Re =64000 falls in the well-stirred reactor zones. They are close to the broken reaction zone. Investigation

on the geometries of the grids and combustor needs to be done for future high-speed combustion. Apart from these conditions, the flame mostly falls in the thickened flame regime (thin reaction zone). Large-scale fluid structures bump on the flame fronts and make the flame shattered. The infusion of small eddies to the flame core further stretched the flame. Therefore, the reaction zone gets thinner. The same flame regime characteristics are noticed from the flame profiles/edges reported in this thesis.

To verify the experimental flame front characteristics, a separate premixed combustion model (PCM) has been performed. The PCM has been conducted at all flow conditions under a stoichiometric condition. The PCM and PIV derived Da values are compared. The values matched with less than a 10% discrepancy. It indicates that the flame regime characteristics derived from PIV and PLIF are valid. The author then investigates the turbulent flame speed (S_T) using the PCM. It is found that the is higher under large-hole diameter grids (grid 2 and 4). The opposite is true for grid 1 and 3.

In the first phase of research, experimental methodologies and post-data/image processing tools have been developed for subsonic combustion tests. The results are validated using PIV, PLIF and PCM analysis. In the second phase of the research, the system is being upgraded for supersonic combustion. For this, analytical and computational fluid-heat transfer analysis has been conducted. A 16 kW in-flow industrial air heater is chosen for supersonic combustion. Besides, an analytical study has been carried out to generate the characteristics dimensions for the converging-diverging nozzle (De Laval Nozzle). These dimensions and flow conditions have been used as the boundary conditions for computational analysis. Two different methods (Viscous k-ε model and inviscid model) have been considered for the computational analysis. After several trials, it is found that the inviscid model provides better results than the Viscous k-ε model. Optimized dimensions and flow conditions have been proposed for supersonic combustion (Ma $\geq$ 2).

5.2 Future Recommendations:

In the future, the effect of walls on the velocity contour could be investigated. For this, the z-component velocity (w) needs to be determined. More grids with different geometries and blockage ratios should be considered for flame characteristics study. For this, additive manufacturing techniques could be implemented. Also, combustion modeling should be performed to understand the effect of new grids on the flame front characteristics. The presence of large-scale fluid structures in the flame needs to be minimized. To address this, the inlet of the combustor needs to be modified. This will allow placing the grids further upstream from the fuel injection port. The PIV system resolution has to be increased so that more particles could be traced during the high-speed tests.

Simultaneous PIV-PLIF could be used to trace the instantaneous turbulence and flame characteristics. A higher capacity PLIF system is suggested to capture the maximum CH signal at extreme turbulent conditions. A-X and B-X bands of CH could be used to justify the results presented in this research. For this, wavelength scanning and laser tuning need to be done very carefully.

Extensive combustion modeling needs to be carried out for a better understanding of flame and flow characteristics. The air heater and De Laval Nozzle proposed in this research are compatible with supersonic combustion (Ma $= 2$). More experimentation, analytical analysis, computational analysis, and combustion modeling needs to be done for Ma ≥ 2.0. This analysis will provide information on the location of fuel and air injection port, grids and pilot igniters. Experimental strategies and post data analysis techniques should be developed for Ma ≥ 2.0. For this, the existing MATLAB image processing codes need to be modified.

References

[1]   M. K. Bobba, "Flame Stabilization and Mixing Characteristcs In A Stagnation Point Reverse Flow Combustor," Georgia Institute of Technology, 2007.

[2]   M. A. Hossain, "Design of A High Intensity Turbulent Combustion System," The University of Texas at El Paso, 2015.

[3]   A. W. Skiba, C. D. Carter, S. D. Hammack, and T. Lee, "A simplified approach to simultaneous multi-scalar imaging in turbulent flames," *Combust. Flame*, vol. 189, pp. 207–211, 2018, doi: 10.1016/j.combustflame.2017.10.035.

[4]   P. L. Fluorescence, "Role of Planar Laser-Induced Fluorescence in Combustion Research," *AerospaceLab*, no. 1, pp. 1–14, 2009.

[5]   J. F. Driscoll, "Turbulent Combustion , Experimental and Fundamental Models," 2016.

[6]   S. A. Filatyev, J. F. Driscoll, C. D. Carter, and J. M. Donbar, "Measured properties of turbulent premixed flames for model assessment , including burning velocities , stretch rates , and surface densities," vol. 141, pp. 1–21, 2005, doi: 10.1016/j.combustflame.2004.07.010.

[7]   M. Tanahashi, S. Murakami, and G. Choi, "Simultaneous CH – OH PLIF and stereoscopic PIV measurements of turbulent premixed flames," vol. 30, pp. 1665–1672, 2005, doi: 10.1016/j.proci.2004.08.270.

[8]   C. D. Carter, J. M. Donbar, and J. F. Driscoll, "Simultaneous CH planar laser-induced fluorescence and particle imaging velocimetry in turbulent nonpremixed flames," vol. i, pp. 129–132, 1998.

[9]   C. D. Carter, S. Hammack, and T. Lee, "High-speed flamefront imaging in premixed turbulent flames using planar laser-induced fluorescence of the CH C-X band,"

Combust. Flame, vol. 168, pp. 66–74, 2016, doi: 10.1016/j.combustflame.2016.03.024.

[10] J. Sjo *et al.*, "Simultaneous visualization of OH , CH , CH 2 O and toluene PLIF in a methane jet flame with varying degrees of turbulence," vol. 34, pp. 1475–1482, 2013, doi: 10.1016/j.proci.2012.05.037.

[11] A. Acosta-zamora, "Flame Front Structure Studies of Highly Turbulent Reacting Flow Over A Backward Facing Step Using kHz OH-CH Planar Laser Induced Fluorescence," The University of Texas at El Paso, 2016.

[12] C. D. Carter, S. Hammack, and T. Lee, "High-speed flamefront imaging in premixed turbulent flames using planar laser-induced fluorescence of the CH C − X band," *Combust. Flame*, vol. 168, pp. 66–74, 2016, doi: 10.1016/j.combustflame.2016.03.024.

[13] K. Periagaram, "Determination of Flame Characteristics In A Low Swirl Burner At Gas Turbine Conditions Through Reaction Zone Imaging," Georgia Institute Technology, 2012.

[14] C. M. Vagelopoulos and J. H. Frank, "An Experimental and Numerical Study on the Adequacy of CH as a Flame Marker in Premixed Methane Flames," *Proc. Combust. Inst.*, vol. 30, no. 1, pp. 241–249, 2005, doi: 10.1016/j.proci.2004.08.243.

[15] M. N. A. Islam, M. A. Hossain, A. Choudhuri, M. D. La Torre, and A. Acosta-zamora, "Laser Diagnostics of Highly Turbulent Premixed Methane-Air Flow Over a Backward Facing Step Using PIV and OH-PLIF," in *AIAA Propulsion and Energy Forum*, 2019, no. August, pp. 1–12, doi: 10.2514/6.2019-4323.

[16] B. F. . Armaly, F. Durst, J. C. F. Pereira, and B. Schonung, "Experimental and theoretical investigation of backward-facing step flow," *J. Fluid Mech.*, vol. 127, no. May 2014, pp. 473–496, 1983, doi: 10.1017/S0022112083002839.

[17] G. Biswas, M. Breuer, and F. Durst, "Backward-facing step flows for various expansion ratios at low and moderate reynolds numbers," *J. Fluids Eng. Trans. ASME*, vol. 126, no. 3, pp. 362–374, 2004, doi: 10.1115/1.1760532.

[18] R. W. Pitz and J. W. Daily, "Combustion in a turbulent mixing layer formed at a rearward-facing step," *AIAA J.*, vol. 21, no. 11, pp. 1565–1570, 1983, doi: 10.2514/3.8290.

[19] J. M. . Cohen and T. J. Anderson, "Experimental investigation of near-blowout instabilities in a lean, premixed step combustor," vol. 1, no. c. p. 100084.

[20] V. Sabel 'nikov *et al.*, "Thermo-Acoustic Instabilities in a Backward-Facing Step Stabilized Lean- Premixed Flame in High Turbulence Flow," in *14th Int Symp on Applications of Laser Techniques to Fluid Mechanics*, 2008, no. 07-10 July, pp. 1–12.

[21] P. J. W. Roberts and D. R. Webster, "Turbulent diffusion," *Environ. Fluid Mech. Theor. Appl.*, pp. 7–45, 2003, doi: 10.1017/cbo9780511808944.006.

[22] A. N. Kolmogorov, "Dissipation of Energy in the Locally Isotropic Turbulence," in *Mathematical and Physical Sciences*, 1991, vol. 434, no. 1890, pp. 15–17, doi: 10.1017/S0022112094212417.

[23] P. A. Davidson, *Turbulence: An Introduction for Scientists and EngineersTurbulence: An Introduction for Scientists and Engineers , P. A. Davidson , Oxford U. Press, New York, 2004. $174.50, $74.50 paper (657 pp.). ISBN 0-19-852948-1, ISBN 0-19-852949-X paper*. New York: Oxford Union Press, 2004.

[24] F. A. Williams, *Combustion Theory: The Fundamental Theory of Chemically Reacting Flow Systems*, 2nd Editio., vol. 53, no. 9. The Benjamin/Cummings Publishing Company, Inc., 1985.

[25] N. Peters, *Turbulent Combustion-Cambridge*. Cambridge, United Kingdom: Cambridge University Press, 2000.

[26] P. Griebel, P. Siewert, and P. Jansohn, "Flame characteristics of turbulent lean premixed methane/air flames at high pressure: Turbulent flame speed and flame brush thickness," *Proc. Combust. Inst.*, vol. 31, no. 2, pp. 3083–3090, 2007, doi: 10.1016/j.proci.2006.07.042.

[27] M. A. Hossain, N. A. Islam, W. Hossain, and A. Choudhuri, "CH-PLIF Diagnostics of High-Intensity Turbulent Premixed Methane-Air Combustion," in *AIAA Scitech 2020 Forum*, 2020, no. January, pp. 1–14, doi: 10.2514/6.2020-1705.

[28] M. N. A. Islam, M. A. Hossain, M. De la Torre, A. Acosta-Zamora, and A. R. Choudhuri, "Laser Diagnostics of Highly Turbulent Premixed Methane-Air Flow Over a Backward Facing Step Using PIV and OH-PLIF," in *AIAA Propulsion and Energy Forum*, 2019, no. August, pp. 1–12, doi: 10.2514/6.2019-4323.

[29] M. A. Hossain, M. N. A. Islam, and A. Choudhuri, "FLAME IMAGING OF HIGHLY TURBULENT PREMIXED METHANE-AIR COMBUSTION USING PLANAR LASER INDUCED FLUORESCENCE (PLIF) OF CH (C-X)," in *ASME 2019 Power Conference*, 2019, pp. 1–7.

[30] F. T. C. Yuen and Ö. L. Gülder, "Premixed turbulent flame front structure investigation by Rayleigh scattering in the thin reaction zone regime," *Proc. Combust. Inst.*, vol. 32, no. 2, pp. 1747–1754, 2009, doi: 10.1016/j.proci.2008.08.005.

[31] P. Tamadonfar and Ö. L. Gülder, "Experimental investigation of the inner structure of premixed turbulent methane/air flames in the thin reaction zones regime," *Combust. Flame*, vol. 162, no. 1, pp. 115–128, 2015, doi: 10.1016/j.combustflame.2014.07.001.

[32]   L. P. H. De Goey, T. Plessing, R. T. E. Hermanns, and N. Peters, "Analysis of the flame thickness of turbulent flamelets in the thin reaction zones regime," *Proc. Combust. Inst.*, vol. 30, no. 1, pp. 859–866, 2005, doi: 10.1016/j.proci.2004.08.016.

[33]   A. Kalantari, E. Sullivan-Lewis, and V. McDonell, "Development of Criteria for Flashback Propensity in Jet Flames for High Hydrogen Content and Natural Gas Type Fuels," 2016.

[34]   S. D. Hammack, "Development of High-Speed Laser Diagnostics for the Study of Advanced Propulsion Systems," 2015.

[35]   Y. A. Çengel and J. M. Cimbala, *Fluid Mechanics: Fundamentals and Application*, Fourth Edi. Mc Graw Hill Education, 2018.

[36]   Y. A. Cengel and J. M. Cimbala, *Fluid Mechanics: Fundamentals and Applications*, Third Edit. New York: Mc Graw Hill, 2014.

[37]   "LIF Systems for Combustion Diagnostics," *Dantec Dynamics, www.dantecdynamics.com*, 2016. .

[38]   G. Laufer, *Introduction to optics and lasers in engineering*, First Edit. New York: Cambridge University Press, 1996.

[39]   Z. Peng, H. Zhao, and N. Ladommatos, "Visualization of the homogeneous charge compression ignition / controlled autoignition combustion process using two-dimensional planar laser-induced uorescence imaging of formaldehyde," vol. 217, pp. 1125–1134.

[40]   A. W. Skiba, C. D. Carter, S. D. Hammack, J. D. Miller, J. R. Gord, and J. F. Driscoll, "The influence of large eddies on the structure of turbulent premixed flames characterized with stereo-PIV and multi-species PLIF at 20 kHz," *Proc. Combust.*

Inst., vol. 37, no. 2, pp. 2477–2484, 2019, doi: 10.1016/j.proci.2018.07.122.

[41]   M. Alejandro and D. E. L. A. Torre, "Characterization of High Intensity Turbulent Flows through Time Resolve Particle Image Velocimetry in a Backward Facing Step Combustor," University of Texas at El Paso, 2016.

[42]   M. K. Bobba, P. Gopalakrishnan, K. Periagaram, and J. M. Seitzman, "Flame structure and stabilization mechanisms in a stagnation point reverse flow combustor," *Proc. ASME Turbo Expo*, vol. 2, no. December, pp. 879–888, 2007, doi: 10.1115/GT2007-28231.

[43]   J. M. Donbar, J. F. Driscoll, and C. D. Carter, "Simultaneous CH planar laser-induced fluorescence and particle imaging velocimetry in turbulent flames," *36th AIAA Aerosp. Sci. Meet. Exhib.*, vol. i, pp. 129–132, 1998, doi: 10.2514/6.1998-151.

[44]   J. D. Miller, S. R. Engel, J. W. Tröger, T. R. Meyer, and T. Seeger, "Characterization of a CH planar laser-induced fluorescence imaging system using a kHz-rate multimode-pumped optical parametric oscillator," *Appl. Opt.*, vol. 51, no. 14, pp. 2589–2600, 2012, doi: 10.1364/AO.51.002589.

[45]   N. Jiang, R. A. Patton, W. R. Lempert, and J. A. Sutton, "Development of high-repetition rate CH PLIF imaging in turbulent nonpremixed flames," *Proc. Combust. Inst.*, vol. 33, no. 1, pp. 767–774, 2011, doi: 10.1016/j.proci.2010.05.080.

[46]   S. Yoshida, Y. Naka, Y. Minamoto, M. Shimura, and M. Tanahashi, "Propagation Characteristics of Turbulent Methane-Air Premixed Flames at Elevated Pressure in a Constant Volume Vessel," in *18th International Symposium on the Application of Laser and Imaging Techniques to Fluid Mechanics*, 2016, vol. July 4-7, pp. 1–12.

[47]   M. -S Chou and A. M. Dean, "Excimer laser perturbations of methane flames: High

temperature reactions of OH and CH," *Int. J. Chem. Kinet.*, vol. 17, no. 10, pp. 1103–1118, 1985, doi: 10.1002/kin.550171007.

[48]   M. Tsujishita, M. Ipponmatsu, and A. Hirano, "Visualization of the ch molecule by excitiug c2s+\v=l) state in turbulent flames by planar laser-induced fluorescence," *Jpn. J. Appl. Phys.*, vol. 32, no. 12 R, pp. 5564–5569, 1993, doi: 10.1143/JJAP.32.5564.

[49]   C. M. Mitsingas *et al.*, "Simultaneous high speed PIV and CH PLIF using R-branch excitation in the C 2 Σ + -X 2 Π (0,0) band," *Proc. Combust. Inst.*, vol. 37, no. 2, pp. 1479–1487, 2019, doi: 10.1016/j.proci.2018.08.014.

[50]   J. A. Y. B. Jeffries, R. A. Copeland, G. P. Smith, and D. R. Crosley, "Multiple Species Laser-Induced Fluorescence In Flames," *Twenty-first Symp. Combust. Combust. Inst.*, pp. 1709–1718, 1986.

[51]   M. E. Quiroz-regalado, "Fluid Flow Characterization of High Turbulent Intensity Compressible Flow Using Particle Image Velocimetry," University of Texas at El Paso, 2015.

[52]   I. A. Mulla *et al.*, "Heat release rate estimation in laminar premixed flames using laser-induced fluorescence of CH 2 O and H-atom," vol. 165, pp. 373–383, 2016, doi: 10.1016/j.combustflame.2015.12.023.

[53]   P. M. Allison, "Experimental Characterization of Combustion Instabilities and Flow-Flame Dynamics in a Partially-Premixed Gas Turbine Model Combustor," The University of Michigan, 2013.

[54]   I. V Dyakov, J. De Ruyck, V. U. Brussel, K. J. Bosschaart, and P. De Goey, "Measurement of adiabatic burning velocity in methane-oxygen-nitrogen mixtures," *Combust. Sci. Technol.*, vol. 172, no. 1, pp. 81–96, 2001, doi:

10.1080/00102200108935839.

[55] J. G. Gens, F. Mauss, and N. Peters, "Analytic approximations of burning velocities and flame thicknesses of lean hydrogen, methane, ethylene, ethane, acetylene, and propane flames," in *Twenty-Fourth Symposium (International) on Combustion/The combustion Institute*, 1992, pp. 129–135, doi: https://doi.org/10.1016/S0082-0784(06)80020-2.

[56] X. Zhen, X. Li, Y. Wang, D. Liu, Z. Tian, and Y. Wang, "Effects of the initial flame kernel radius and EGR rate on the performance, combustion and emission of high-compression spark-ignition methanol engine," *Fuel*, vol. 262, no. October 2019, p. 116633, 2020, doi: 10.1016/j.fuel.2019.116633.

[57] Y. H. Chang and S. B. Han, "Characteristics of Flame Kernal Radius In A Spark Ignition Engine According To The Electric Spark Ignition Energy," *Int. J. Automot. Technol.*, vol. 15, no. 5, pp. 715–722, 2014, doi: 10.1007/s12239.

Vita

Md. Amzad Hossain was born and raised in Noakhali, Bangladesh. He received his B.Sc. Eng. in Mechanical Engineering from Khulna University of Engineering & Technology (KUET), Bangladesh on May 16th, 2011 with distinction (CGPA: 3.78/4.0, First-class First, President Gold Medalist and Prime Minister Gold Medalist). After graduation, he worked as a Production Engineer in Global Heavy Chemicals Limited, Bangladesh for 9 months. He has finished his M.Sc. Eng. in Mechanical Engineering from Khulna University of Engineering & Technology (KUET), Bangladesh on December 15th, 2013 with CGPA 3.94 out 4.0. He has served as a Lecturer (2012-2014) and Assistant Professor (2014-Present, currently on study leave) in the Department of Mechanical Engineering at Khulna University of Engineering & Technology (KUET), Bangladesh. He went to USASK, Canada in Summer 2016 for his Ph.D. study. Later he has transferred to UTEP, USA to finish his Ph.D. His research interests are in combustion and propulsion, Aerodynamics, and HVAC. His long-term career goal is to establish himself at the forefront of academia.

Contact Information: mhossain8@miners.utep.edu

This thesis/dissertation was typed by Md. Amzad Hossain.